

The Pennsylvania State University  
The Graduate School  
College of Engineering

**DYNAMICS OF FISH**

A Thesis in  
Physics  
by  
Your Name

© 2013 Your Name

Submitted in Partial Fulfillment  
of the Requirements  
for the Degree of

Doctor of Philosophy

May 2013

The thesis of Your Name was reviewed and approved\* by the following:

Joseph H. Blow  
Professor of SomeThing  
Thesis Advisor  
Chair of Committee

Reader Name  
Professor of SomeThing  
Optional Title Here

\*Signatures are on file in the Graduate School.

# **Abstract**

Some nonsense goes here.

# Table of Contents

List of Figures	vii
List of Tables	x
List of Symbols	xi
Acknowledgments	xii
<b>Chapter 1</b>	
<b>Introduction</b>	1
<b>Chapter 2</b>	
<b>Background and literature review</b>	3
2.1 Semiconductors . . . . .	3
2.1.1 Metal-Semiconductor-Metal conduction . . . . .	3
2.1.2 Field effect transistors (FET) . . . . .	7
2.1.2.1 Band Bending? (TODO) . . . . .	10
2.1.3 Weak localization (TODO) . . . . .	11
2.2 Ferroelectricity . . . . .	11
2.2.1 Piezoelectricity and pyroelectricity . . . . .	11
2.2.2 Domains and polarization . . . . .	12
2.2.3 Phase transitions . . . . .	14
2.2.3.1 First-order, $\beta < 0$ and $\gamma > 0$ . . . . .	15
2.2.3.2 Second-order, $\beta > 0$ . . . . .	15
2.2.4 Ferroelectric field-effect transistors (FeFETs) . . . . .	16
2.2.5 Ferroelectric tunnel junctions (FTJs) . . . . .	19
2.2.6 Polar metals . . . . .	21
2.2.7 FeFETs with ferroelectric channels . . . . .	21
2.3 2D materials . . . . .	22
2.3.1 Trapped charge in 2D FETs? (TODO) . . . . .	22
2.3.2 In-Se compounds . . . . .	22
2.3.2.1 $\text{In}_2\text{Se}_3$ polymorphs in literature . . . . .	22

<b>Chapter 3</b>	
<b>Sample fabrication and measurement methods</b>	<b>26</b>
3.1 Introduction . . . . .	26
3.2 Flake generation . . . . .	27
3.2.1 Manufacturing alignment marker wafer chips . . . . .	27
3.2.2 Mechanical exfoliation from bulk crystals to thin flakes . . . . .	29
3.3 Thin crystal characterization . . . . .	30
3.3.1 Scanning probe microscopy . . . . .	30
3.3.1.1 Atomic force microscopy . . . . .	31
3.3.1.2 Piezoresponse force microscopy . . . . .	34
3.3.2 Optical second harmonic generation . . . . .	36
3.3.3 Raman (TODO: review) . . . . .	38
3.4 Device manufacture . . . . .	40
3.4.1 Photolithography . . . . .	40
3.4.1.1 LOR/SPR stack . . . . .	41
3.4.1.2 PMMA/PMGI/SPR stack for alkali-sensitive materials .	41
3.4.2 Thin filament shadow mask . . . . .	43
3.4.3 Metal evaporation and liftoff . . . . .	43
3.4.4 Sample wiring . . . . .	45
3.4.5 Layer Transfer (TODO: review) . . . . .	46
3.5 Device characterization . . . . .	47
3.5.1 Electronic measurement systems (TODO: review) . . . . .	47
3.5.2 PPMS (TODO: review) . . . . .	48
3.5.3 Hall probe (TODO) . . . . .	48
<b>Chapter 4</b>	
<b>Electric field induced metallic behavior in thin crystals of ferroelectric <math>\alpha</math>-In<sub>2</sub>Se<sub>3</sub></b>	<b>51</b>
4.1 Introduction . . . . .	51
4.2 Device manufacture . . . . .	52
4.3 Optical crystal measurements . . . . .	54
4.4 FET measurements . . . . .	55
4.5 Discussion . . . . .	56
<b>Appendix A</b>	
<b>3D crystal symmetry groups</b>	<b>62</b>
<b>Appendix B</b>	
<b>Project Unity control software</b>	<b>67</b>
B.1 Running Unity . . . . .	67
B.2 Main Program Structure . . . . .	67
B.2.1 Static Environments . . . . .	68
B.2.2 Dynamic Environments . . . . .	68
B.2.3 Stand alone classes . . . . .	69

B.3	Main Algorithm . . . . .	69
B.4	File format (Parameters to/from File) . . . . .	69
B.5	Hardware (System Specific Subprograms) . . . . .	70
B.6	DC (Sourcing and Measuring) . . . . .	70
B.7	Queueing measurements . . . . .	70

**Appendix C**  
**Additional  $\alpha$ -In<sub>2</sub>Se<sub>3</sub> Figures** 72

# List of Figures

2.1	Band diagrams of metal in contact with a n-type semiconductor . . . . .	5
2.2	Current-voltage behavior of various junctions . . . . .	7
2.3	FET . . . . .	9
2.4	Polarization . . . . .	13
2.5	Landau first order transition . . . . .	16
2.6	Landau second order transition . . . . .	17
2.7	Ferroelectric field effect transistors . . . . .	18
2.8	Ferroelectric tunnel junctions . . . . .	20
2.9	In-Se alloy phase diagram. . . . .	23
2.10	In <sub>2</sub> Se <sub>3</sub> crystal structure . . . . .	24
3.1	Device manufacture. . . . .	28
3.2	Mechanical exfoliation of thin flakes of bulk crystal . . . . .	31
3.3	Atomic force microscope . . . . .	32
3.4	AFM interaction modes . . . . .	33
3.5	PFM and ferroelectric materials . . . . .	35
3.6	Optical second harmonic generation . . . . .	37

3.7	Raman Spectroscopy . . . . .	39
3.8	Photoresist stacks . . . . .	42
3.9	Filament device . . . . .	44
3.10	Sample wiring . . . . .	49
3.11	Layer transfer station setup . . . . .	50
3.12	PPMS and electronics measurement system . . . . .	50
4.1	Device images . . . . .	54
4.2	Optical measurements of $\alpha\text{-In}_2\text{Se}_3$ . . . . .	55
4.3	Sample A: $I_D (V_{DS})$ . . . . .	57
4.4	Sample A: $I_D (V_G)$ transfer characteristics . . . . .	58
4.5	Temperature dependence . . . . .	59
4.6	Magnetic field measurements . . . . .	60
C.1	Sample A: $I_D (V_{DS}, V_G)$ . . . . .	73
C.2	Sample B: $I_D (D_{DS}, V_G)$ . . . . .	74
C.3	Sample C: $I_D (V_{DS}, V_G)$ . . . . .	75
C.4	Sample B: $I_D (V_G)$ transfer characteristics . . . . .	76
C.5	Sample C: $I_D (V_G)$ transfer characteristics . . . . .	77
C.6	Sample C: effects of warming and cooling while gated . . . . .	78
C.7	Sample B: $I_D (V_G), V_G$ rate dependence . . . . .	78
C.8	Sample D: contact resistance . . . . .	79
C.9	Sample A and B: annealing . . . . .	79

C.10 Sample A: magnetoconductance . . . . .	80
---	----

# List of Tables

2.1	<i>In<sub>2</sub>Se<sub>3</sub></i> polymorphs . . . . .	24
2.2	<i>InSe</i> polymorphs . . . . .	25
3.1	Lithography resists . . . . .	41
4.1	Device parameters . . . . .	53
A.1	3D crystal classes [1] . . . . .	62

# List of Symbols

- $\alpha$  The first Landau parameter, p. 14
- $\beta$  The first Landau parameter, p. 14
- $\gamma$  The first Landau parameter, p. 14
- $E$  Electric field, p. TODO
- $E_c$  Coercive electric field, p. 13
- $P$  Material polarization, p. 11
- $T_0$  Landau Curie–Weiss transition temperature, p. 14
- $T_C$  The Curie temperature, p. 11

# Acknowledgments

# Chapter 1

## Introduction

Ferroelectricity was first experimentally observed just over 100 years ago in 1920 by a PhD student at the University of Minnesota, Joseph Valasek [2]. Valasek was originally working with piezoelectric crystals to develop a seismograph when he observed that placing one such material, Rochelle salt, in an electric field showed S-like curve with hysteresis [3]. Ferromagnetism was already known at the time of the discovery so Valasek made the analogous connection showing the relationship between magnetic and electric fields. This gave rise to the term “ferroelectricity” even though such materials rarely contain iron like their ferromagnetic precursors. Ferroelectricity was largely ignored until the discovery of barium titanate ( $\text{BaTiO}_3$ ) during the second world war, where Valasek was seeking to use ferroelectrics to make transducers for submarine detection. Barium titanate had many physical advantages compared to Rochelle salt, it was chemically stable at room temperature, insoluble in water, a high dielectric constant, and more robust ferroelectricity. Its simple structure helped researchers investigate ferroelectricity, eventually resulting in the Landau-Ginzberg-Devonshire phenomenological model of ferroelectricity in 1951 [4]. Barium titanate is still used today in “condensers” and capacitors as its relative permittivity is much greater than most non-ferroelectric dielectrics. [5]

$\text{BaTiO}_3$  showed that oxide crystals could be ferroelectric and in the decades following the Second World War hundreds new ferroelectric compounds were discovered. Ceramics are the most common ferroelectrics in use, due to the ease of manufacture and the ability to build complex configurations in while still behaving like a single ferroelectric crystal. In 1952 lead zirconate-titanate (PZT) was discovered and has become one of the most widely used piezoelectric ceramics, though recent efforts have sought to find lead-free alternatives that are more environmentally friendly. All ferroelectric materials are also piezoelectric and pyroelectric, though the reverse is not true, and many have found

applications in ultrasound, capacitors, transducers, micropositioners, energy harvesters, night vision, sensors, and many other devices.

The applications of ferroelectrics to modern electronics are numerous and diverse, but perhaps the most sought after utilization is enhancing random access memory (RAM) with a ferroelectric dielectric. While the original idea for ferroelectric RAM (FeRAM) was first proposed by Dudley Allen Buck's in his 1952 master's thesis, limitations of the known ferroelectric materials have prevented commercialization. To integrate with silicon transistors, ferroelectrics must be scaled down to a few nanometers in thickness, have a scalable growth processes that is compatible with the temperature limitations of the other materials and lithography processes, all while maintaining their electronic properties. The development of thin ferroelectric films into standard silicon circuits in 1984 was one of the first major milestones approaching practical FeRAM [6] and since then researchers and engineers have continued to push towards this goal. The recent explosive growth in 2D material research, and the subsequent discovery of ferroelectricity down to a few layers of material has opened the possibility of integrating ferroelectric memory with the logic circuits of modern processors.

TODO: discuss what contents of later chapters are.

# Chapter 2 |

# Background and literature review

## 2.1 Semiconductors

Semiconductors, as their name implies, are characterized by their decreased conduction compared to a metal, while still more than an insulating material. They possess a band gap of a few electron volts (eV), driving this conductivity. Semiconductors come in two flavors, n-type and p-type, that conduct predominately using either electrons or holes respectively. Carriers reside below the Fermi energy in the fully occupied valance band but can be exited to move to an unoccupied higher energy band, the conduction band and thus move thus conduct. This is often through thermal excitation, so most semiconductors have an increased resistance at low temperatures. Photons can also excite electrons giving rise to countless applications such as sensors and LEDs. Furthermore, semiconductor behavior can be altered by introducing other elements or electric fields giving rise to a wide range of potential applications in just about every area of modern electronics.

TODO Add band diagram showing metal, sc, insulator

### 2.1.1 Metal-Semiconductor-Metal conduction

When constructing electronic devices with multiple materials the physical and chemical properties of the material contact region must be considered. When placed in contact with each other, band structures of the individual crystal is altered as a new preferred energy minimum is reached, chemical reactions between the two materials can take place, and the physical dimensions of one material can shift to accommodate the other. For most electronic transport applications, an ohmic contact is preferred as it takes the least potential to form a current and is an easily predictable behavior. Ohmic contact is

characterized by a linear relationship between the voltage and current given by the usual equation  $V = IR$ . This typically seen for a metal-metal junction as there is little band bending and metal's ability to conduct at a wide range of energy levels. At the interface between metals and semiconductors a Schottky contact is typically formed instead that is non-ohmic in behavior. The actual nature of Schottky contacts is complicated and no simple model exists for the interface of metal-semiconductors. [7, 8] To predict the behavior of a metal-insulator junction one must numerically calculate the quantum mechanical states of the system, including the materials chemistry, and include the system's geometry. [9]

To provide at least a metal model of the behavior of the system, a simplistic model will be given for the behavior of a Schottky contact that ignores some of the individual details but gives broad predictions. Next to the junction, the electrons in the semiconductor move to (or from) the conduction band of the metal, depleting (accumulating) electrons in the area nearest to the metal. This causes the bands to bend, shown in Figure 2.1a-2.1b. The Schottky-Mott rule gives the energy barrier  $\Phi_B$  of a charge carrier  $q$  between the two materials in terms of the work function of the metal  $\phi_M$  and semiconductor electron affinity  $\chi_{SC}$

$$\begin{cases} \Phi_{B,n} = \phi_M - \chi_{SC} & n-type \\ \Phi_{B,p} = \chi_{SC} - \phi_M & p-type \end{cases} \quad (2.1)$$

The bulk of the semiconductor band shifts to accommodate the difference in work functions of both materials  $\phi_M - \phi_{SC}$ .

Applying a forward voltage bias to the system allows electrons from the semiconductor band to tunnel into the metal forming a current. Applying a bias in reverse causes only a few thermally excited electrons in the metal to tunnel to the semiconductor resulting in almost no current. Taken together, for an n-type semiconductor electrons can more easily flow from the semiconductor to the metal than the reverse. [11] Figure 2.1c-2.1d shows the potential shifting the bands in a forward and reverse bias. However, if a large enough reverse voltage bias is applied the carriers can instead move to the valance band of the semiconductor. This voltage-current curve is used to form diodes that conduct current only in one direction, where the reverse current is considered the breakdown potential of the diode. In order to reduce the band mismatch various techniques are often used to achieve Ohmic contact. Selecting the appropriate metal can reduce the energy band mismatch though it will likely still have a significant barrier. A common solution is to instead dope the semiconductor near the region of contact to provide a smooth transition between the metal and the semiconducting region.

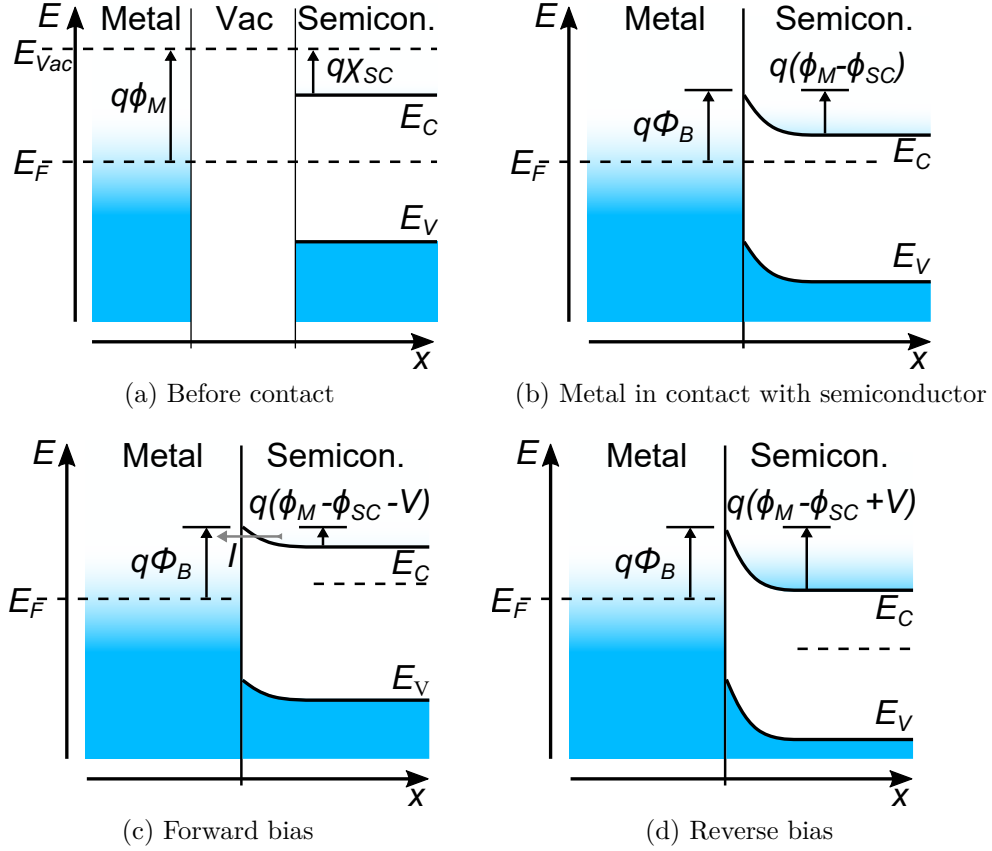


Figure 2.1: Band diagrams of metal in contact with a n-type semiconductor (2.1a) before and (2.1b) after a metal is brought into contact with a n-type semiconductor. [10]  $\Phi_B$  is the Schottky barrier height,  $E_F$ , the Fermi energy,  $E_C$  and  $E_V$  the conducting and valance bands. 2.1c forward and 2.1d reverse voltage bias applied from right to left. Arrow indicated the direction of current flow.  
TODO: Add in boundary layer. Match with FTJ and FeFET

For Schottky contacts behavior can be modeled using thermionic emission theory. The current density is given by

$$J = J_0 \left( \exp \left( \frac{qV}{k_B T} \right) - 1 \right), \quad (2.2)$$

$$J_0 = A^{**} T^2 \exp \left( -\frac{q\Phi_B}{k_B T} \right) \quad (2.3)$$

where  $J_0$  is the saturation current density,  $q$  the fundamental charge,  $k_B$  Boltzmann constant,  $T$  the temperature, and  $A^{**}$  the Richardson constant. [12–14] For a complete conduction channel though a semiconductor, both metal contacts must be considered, current in and out, as both are Schottky barriers. If we apply a voltage across the entire

structure we have to consider the potential drop across each contact  $V_n$  as well as the material itself  $V_{SC}$ . The voltage drop across a single diode is then

$$V_n = \pm \frac{k_B T}{q} \ln \left( \pm \frac{J}{J_{0n}} + 1 \right) \quad (2.4)$$

where the sign corresponds to the direction of current and  $J_{0n}$  depends on the individual barrier energy  $\Phi_{Bn}$ . We may also consider that the contacts may not be ideal and introduce a contact specific parameter  $n_n \geq 1$  to take this into account. With this we have the total voltage across the contacts

$$V = V_1 + V_{SC} + V_2 \quad (2.5)$$

$$V = \frac{n_1 k_B T}{q} \ln \left( \frac{J}{J_{01}} + 1 \right) + RAJ - \frac{n_2 k_B T}{q} \ln \left( \frac{J}{J_{02}} + 1 \right) \quad (2.6)$$

where  $A$  is the surface area and  $R$  the resistance of the semiconductor. [12–14] This equation is not directly solvable for the current density but it is possible to numerically model the behavior as shown in figure 2.2. Figure 2.2a shows a typical linear ohmic behavior for large and small resistance. Figure 2.2b and 2.2c shows the behavior of a single diode and attached to a large and small resistance. The increased resistance can be seen in the higher voltages needed to reach the saturation current while the barrier height limits the reverse bias current. Figure 2.2e and 2.2f shows the behavior of both barriers and the semiconductor in this model. Similar to the single contact, the barrier height dictates the saturation current and the resistance the rate at which increasing voltage reaches saturation. The ideality factor  $n$  produces a deviation from the ideal curves which can easily be seen with a smaller  $R$ , making two contacts that have the same barrier height still produce an asymmetric behavior. This differentiation will decrease as  $R$  increases and the semiconductor resistance becomes as large as the contacts.

This non-linear behavior must be taken into account for any electronic transport done on a material as the Schottky contact can have multiple competing effects on a measurement. For a four-terminal device charges may or may not tunnel into a lead in contact with the semiconductor based on the size of the barrier and the resistance of the material being tested. Furthermore by placing a metal in contact with a semiconductor the region around the material is altered so a uniform material can not be assumed if it is near that metal. The ideality factor and barrier height can shift the two terminal resistance of a material so the current produced is not symmetric with respect to the voltage direction.

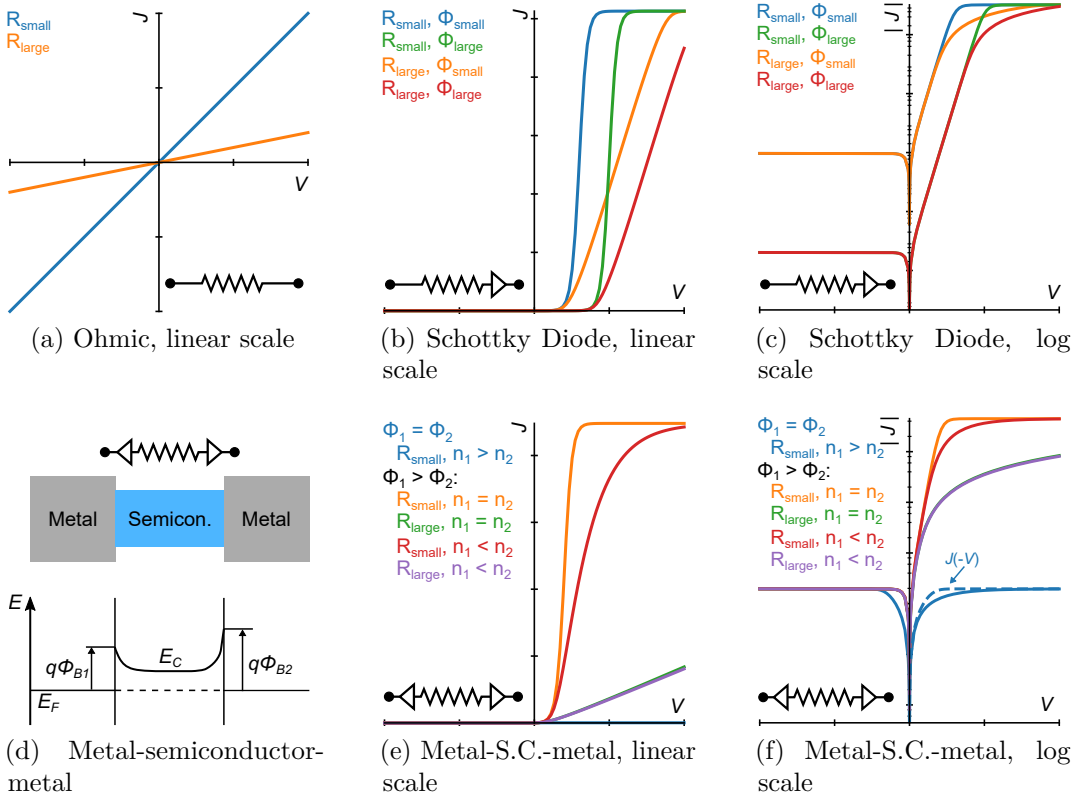


Figure 2.2: Current-voltage behavior of various junctions

Current-voltage graphs of the behaviors of different junction parameters from equation 2.6. (a) ohmic behavior, with no Schottky barrier with large and small resistances. A single Schottky barrier with small and large resistances and barrier heights, in linear (b) and logarithmic (c) plots. (d) simplified band diagram for a double Schottky barrier in a metal-semiconductor-metal device. A double Schottky barrier with large and small resistances, barrier heights, and ideality factors on a linear (e) and log (f) scale. The dashed line shows the asymmetrical nature of a pair of junctions with different ideality factors.

## 2.1.2 Field effect transistors (FET)

One of the most common applications of semiconductor devices is a field effect transistor (FET). Transistors provide a way to turn a current on or off with a voltage, allowing for controllable states in larger circuits. This forms the basis of digital logic in computers, by defining a threshold current as “on” or “off” we form a binary system. Transistors also allow for circuit elements to be isolated from each other, providing a path for different parts of a circuit to interact with one element while independent of the rest.

The typical structure of a FET is two ohmic contacts on either side of a semiconductor with a metal gate positioned on the semiconductor in between the two contacts.

Between the two contacts a conduction channel is established that majority charge carries, electrons or holes, can pass through. The natural conductivity of this channel can be altered by doping the semiconductor material to change the carrier concentration in the semiconducting material. The gate then provides an electric field that acts on the carriers passing between the two contacts. Removing carriers, known as depletion, will decrease the conductivity, while enhancement adds carriers to increase conductivity. There are two common types of FET, junction gate field-effect transistor (JFET) and metal-oxide-semiconductor FET (MOSFET).

JFET gates are composed of two gates placed on either side of the conduction channel. The gates are opposite in type to the channel, so if the channel is n-type the gate is p-type and vice-versa, figure 2.3a. This junction sets up a depletion region around the gates with a lower carrier concentration. By applying a bias between the source and the gate the depletion region can be expanded, shrinking the conduction channel. This eventually pinches off the entire channel forcing carriers to tunnel across the depletion region and halting most current thus giving an off state to the JFET. Because of this configuration, all JFET must be doped to conduct naturally and operate in depletion mode, as the reverse would generate current though the gate instead.

MOSFET incorporate a thin insulating oxide barrier between the metal gate and the conduction channel channel to isolate each and preventing a junction from forming, as seen in figure 2.3b. This also eliminates almost all current between the gate and the gate and the conduction channel, one of the most important advantages of MOSFET over other types of transistors. The conduction channel contacts are doped to form ohmic contacts opposite to the substrate. MOSFET transistors can operate in either enhancement or depletion mode, another of their significant assets, figure 2.3c shows the different operation modes possible. In enhancement mode the channel region does not have enough carriers to conduct naturally but by applying a gate voltage carriers are added to the region and current flows. Conversely, in depletion mode the channel will conduct without any bias, often though a doped layer, but an external voltage can be used to remove carriers and produce the off state. The bias between the source and drain leads also changes the electric field, and thus carrier density, within the conduction channel. Too large of a voltage causes the channel to start to pinch off, similar to a JFET, and setting a limit on the current that can be sourced between the contacts.

The interplay of drain-source and gate bias on channel behavior in FET lead to a non-trivial relationship between channel current and voltage. Figure 2.3d shows the typical interplay between drain-source voltage and current at different gate voltage

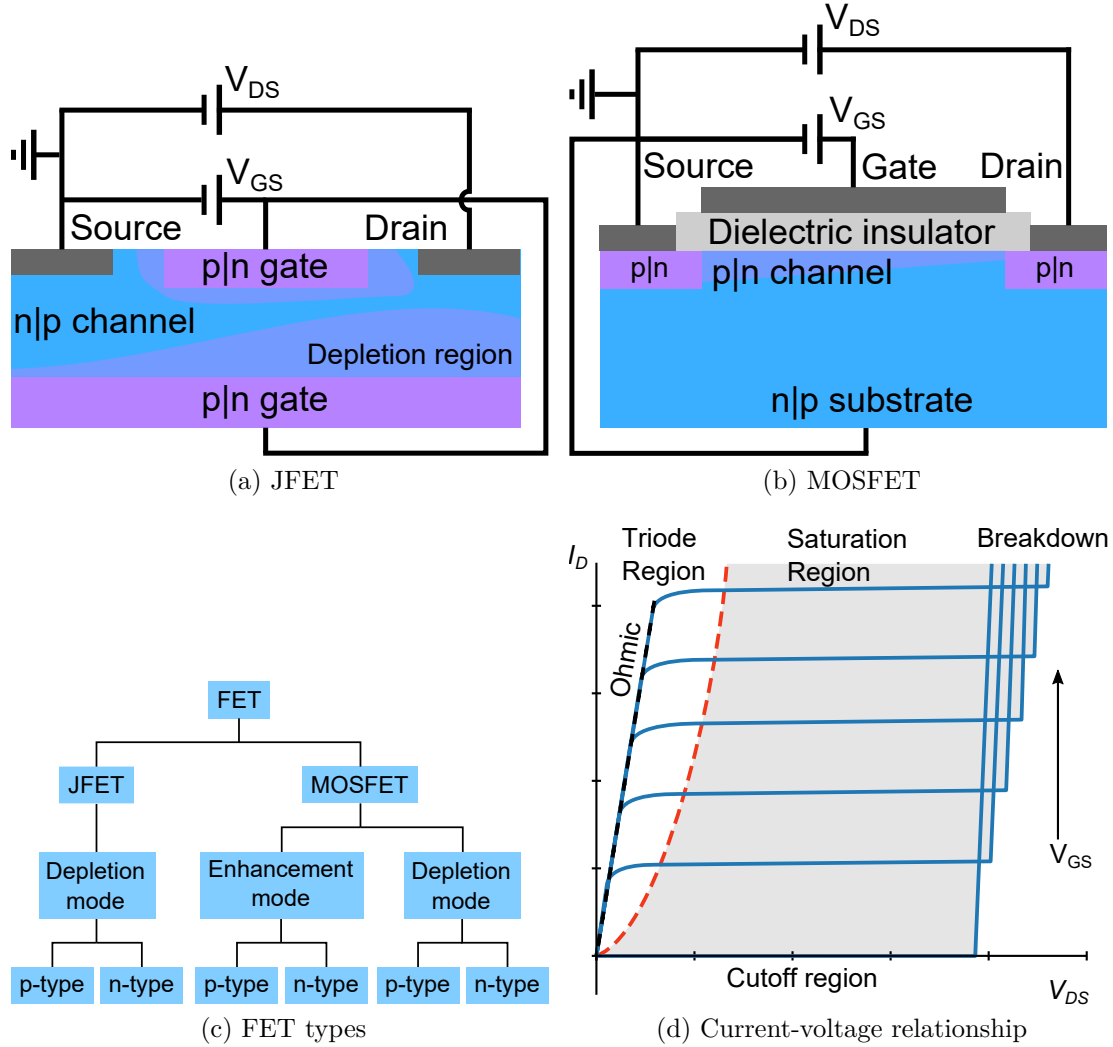


Figure 2.3: FET

Typical (a) JFET and (b) MOSFET devices in n- or p-type configurations. (c) Tree of possible standard FETs used. (d) Source-drain current vs voltage of a generic FET. Different curves show the deviation for increasing gate voltage increments. The transition between ohmic (triode) and saturation occurs near the dotted line. The shown breakdown behavior is a characteristic of a MOSFET rather than most JFET.

intervals. In the cutoff region the channel conduction is exponentially low for almost any current to flow, and is an arbitrary threshold for the off state for a FET. As the channel carrier concentration is raised by the gate voltage the semiconductor has enough free charges for current flow through the channel. For low voltages,  $V_{DS} \leq V_G - V_{th}$ , the current looks linear and the FET acts like an ohmic resistor. The actual increase more

closely follows

$$I_D = 2\kappa \left( (V_{GS} - V_{th}) V_{DS} - \frac{V_{DS}^2}{2} \right) \quad (2.7)$$

where  $\kappa$  is a scaling factor that depends on multiple factors like temperature, device geometry, and gate capacitance.  $V_{th}$  is the threshold voltage at which the gate voltage begins to pinch off the conduction channel, and is also dependent on temperature. Above this limit the current is roughly constant

$$I_D = \kappa (V_{GS} - V_{th})^2 \quad (2.8)$$

and is called the saturation region. The saturation region is what is typically thought of as the on state for a FET, providing an easy binary contrast with the cutoff region. Finally, once  $V_{DS}$  is large enough, there is a rapid increase in current known as breakdown, due to the avalanche effect. This typically occurs only in JFET while MOSFET are limited instead by their power dissipation, however MOSFET can suffer an irreversible breakdown in the gate dielectric instead. [15]

Avalanche breakdown starts when a strong enough electric field causes an electron or hole to be propelled into an atom ionizing it and creating a second free charge. The charges can be further driven through the material ionizing more and more atoms along the way. This creates a runaway effect as the ions produce a conduction channel for more current and more free carriers. Avalanche breakdown can occur in both semiconductors and insulators and is usually irreversible as it forms a permanent conduction medium even after the field is removed. The breakdown oftentimes damages the material as rapid heating arises with the current.

As FET gate and channel contacts are within close proximity of each other, the electric fields produced by the gate will influence the channel contact junction behaviors. The electric field will cause the bands to bend at the junction between materials, potentially changing the barrier height, band bending rate, ideality factor, or other properties. Dealing with this often leads to many real world engineering complications and must be accounted for in device design. We must also be wary of assuming all FET device gating response is due to the bulk of the semiconductor alone, but instead recognize it is often a mix of bulk and contact characteristics.

### 2.1.2.1 Band Bending? (TODO)

TODO: MOSFET band bending?

### 2.1.3 Weak localization (TODO)

## 2.2 Ferroelectricity

Ferroelectric crystals will spontaneously polarize below a critical temperature, known as the Curie temperature  $T_C$ . Below  $T_C$  atoms will create naturally occurring dipoles as they shift to find the lowest overall energy state, sacrificing local electrostatic homogeneity to do so. At higher temperatures the atoms have more energy and space and generally prefer neutrality, forming a paraelectric material instead. When a ferroelectric is exposed to an electric field the dipoles shift to align with the electric field and will remain aligned when that field is removed. Paraelectric materials may form similar dipoles under the electric field but will return to their unpolarized state when the field is removed. Ferroelectrics have many practical applications, as the polarization can be used to enhance capacitors as a dielectric, hold a persistent electronic state, or modify other device properties.

### 2.2.1 Piezoelectricity and pyroelectricity

Piezoelectricity and pyroelectricity arise from non-linear behaviors in crystal structures [16]. There are 32 crystal classes that make up 3D crystals. Of those 21 are non-centrosymmetric, and 20 of the non-centrosymmetric groups form piezoelectric materials. Furthermore, 10 of those groups are polar, forming dipoles with the material. Crystals from these 10 groups are pyroelectric and possibly ferroelectric. All ferroelectrics possess pyroelectricity and all pyroelectrics are piezoelectric, but not all pyroelectrics are ferroelectric and not all piezoelectrics are pyroelectric. This encircling Venn diagram provides a way for easily screening possible ferroelectrics but also means ferroelectrics materials have other attributes. Appendix A shows a list of classes of each type and the corresponding space groups.

In piezoelectric crystals, mechanical motion and polarization are bound together. Applying mechanical strain or stress that shifts the atom locations in the material shifting the dipole orientation or displacement. This generates an electric field and the aggregate can be measured as a voltage across the material. Applied in reverse, an electric field will cause the dipoles within the materials to displace, and provided they are aligned, alter the the crystal size and shape. This has wide applications, giving rise to rapid, precise electric motors and sensors used throughout modern society [16].

In pyroelectricity crystal polarization is conjoined with changes in temperature [16,17]. If we heat or cool a pyroelectric crystal, the crystal structure is altered slightly allowing it

to spontaneous polarize, or if already polarized, change to a new polarization fitting the new atom placement. This polarization produces a voltage across the bulk of the crystal, providing a method to measure this change and thus the changing temperature that drove the re-polarization. After the temperature is fixed the voltage will generally dissipate through leakage currents. This makes pyroelectrics suitable for changing measurements like thermal imaging cameras and energy generation, but poor for managing persistent states in modern digital electronics [16].

### 2.2.2 Domains and polarization

A ferroelectric material is differentiated from a pyroelectric by the ability to switch dipole orientation under an electric field, making ferroelectrics a subset of pyroelectrics.  $\vec{P}$  is the dipole moment per unit volume, in SI-units as Coulombs per square-meter ( $C/m^2$ ). The majority of known ferroelectrics are insulating, limiting the movement of charge within the materials. Dipoles in a ferroelectric can have several different origins that depend on the elements and chemical bonds that make up the material. Electronic polarization comes from the electron cloud shifting around an atom so that local charge density forms a positive region around the nucleus and negative with the electron cloud. As electrons are very light this response is quite fast  $\sim 10^{15} Hz$ . Ionic polarization occurs when cations and anions displace slightly within the crystal to form dipoles. As the nucleus of the atom is much heavier this response is slower, on the order of  $\sim 10^{13} Hz$ . Polarized molecules may also rotate within a material to align with the field, known as orientation polarization. This is much slower,  $\sim 10^7 - 10^9 Hz$ , as the larger molecule is again heavier and the competing forces within the material may limit the motion of the dipole. Lastly, space charge polarization takes place when ions move through multiple crystal layers to create positive and negative crystal regions,  $\sim 10^4 Hz$  [16]. The rate of the dipole movement can be used to characterize the type of dipole in a material and may limit a materials use in high speed electronics.

As an external electric field is increased the dipoles will move to align with the electric field to minimize the energy of the system. The minimum may include different regions of the materials with different dipole alignments, known as domains, shown in figure 2.4a. These domains often are formed at the defects in crystals such as a lattice mismatch or missing atom, and the dipole walls are typically atomically sharp as there are limited possible dipole configurations. For a crystal with all dipoles aligned in a single direction, an increasing opposing electric field will eventually make a dipole switch. From there the domain will begin to nucleate around the original dipole as the electric field continues to

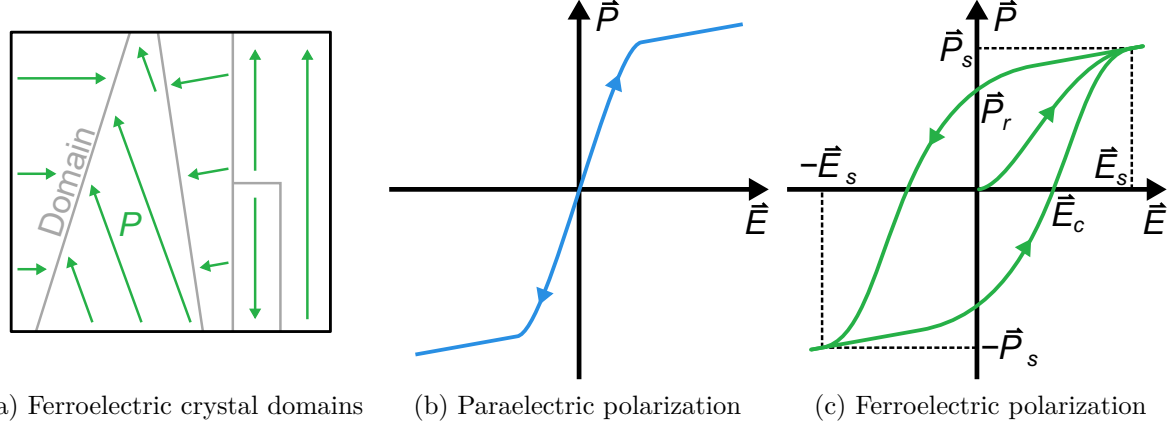


Figure 2.4: Polarization

(a) Ferroelectric domains and dipole orientation within a crystal. Polarization vs electric field for a (b) paraelectric and (c) ferroelectric.  $\vec{E}_c$ ,  $\vec{E}_s$ ,  $\vec{P}_s$ , and  $\vec{P}_r$  are the coercive electric field, spontaneous electric field, spontaneous polarization, and remnant polarization.

increase. This can persist until all the dipoles are aligned in a single direction, forming the maximum polarization of the material. This is the spontaneous polarization  $P_s$ , and occurs at  $E_s$ . A polarized material has excess surface charge on the opposing sides of the material. These charges serve to lessen the field within the material as they produce an electric field within the opposite direction, known as the depolarization field. The depolarization field will cause the dipoles to reorient as thermal fluctuations let the dipoles to find new local energy minimums. As the electric field is reduced to 0 from  $\pm \vec{E}_s$  the depolarization field will force some domains to flip directions, but a finite amount will still remain polarized in the original direction as the remnant polarization  $\vec{P}_r$ . It is this polarization that gives ferroelectric many uses in low power electronics.

One important characteristic in determining whether a crystal is ferroelectric is the transition to paraelectric above the Curie temperature. Above  $T_C$  the temperature fluctuations are enough to destroy any preference the electric charges to remain in a non-neutral configuration. An external electric field may still polarize charges but they will return to electrically neutral when the field is removed. From an energy perspective, two or more local minimums appear for the dipole charges that are offset from each other. Switching the polarization direction requires the electric field must be large enough to overcome this energy barrier, known as the coercive field strength  $\vec{E}_c$ . Figures 2.4b and 2.4c show the respective polarization vs electric field behavior for a paraelectric and ferroelectric dielectric.

One of the largest hindrances to ferroelectrics in many applications is the susceptibility of ferroelectric films to aging and fatigue. Aging is the slow changing of a material's characteristics over time, while fatigue takes place under high electric field. Both take multiple forms and can have similar effects, though the mechanisms are still areas of active research [18]. Crystals may switch to another phase so that the overall stoichiometry does not differ but the elements shift to form a new space group that has a different remnant and spontaneous polarization. Ionic dipoles can form within a crystal that provide a counter electric field within the material or rotate slowly to depolarize. Charged ions, vacancies, or electrons may diffuse through the crystal and later become pinned at domain walls, grain boundaries, or interfaces between materials [19].

### 2.2.3 Phase transitions

Phase transitions in ferroelectrics is usually modeled with the Landau phenomenological approach, or Landau–Devonshire theory. [16, 20] We can write the free energy  $F$  of a ferroelectric in the mean-field approach as

$$F = F_0 + \frac{\alpha}{2}P + \frac{\beta}{4}P^2 + \frac{\gamma}{6}P^6 \cdots - EP \quad (2.9)$$

where  $\alpha$ ,  $\beta$ ,  $\gamma$ , etc are the Landau parameters,  $F_0$  is the free energy density of the disordered (high temperature) phase near the transition, and  $E$  the external field. In the paraelectric phase the Hamiltonian must be invariant under a transformation from  $P$  to  $-P$ , forcing equation 2.9 to only contain even powers of  $P$ . The Landau parameters are pressure and temperature dependent, though usually only the temperature dependence in  $\alpha$  is considered. As  $\alpha$  should switch sign at the transition,  $\alpha$  is generally taken as linear in  $T$  near the transition temperature, taking on the form  $\alpha = \alpha_0(T - T_0)$ , where  $T_0$  is the Curie–Weiss transition temperature ( $T_0 \leq T_C$ ). Equation 2.9 can be modified to fit thin film ferroelectrics by including the boundary conditions [21], but we will keep to the simpler, bulk description and to only three terms in the expansion. To find the local minimums in the free energy we take the derivative

$$\frac{\partial F}{\partial P} = \alpha P + \beta P^3 + \gamma P^5 - E = 0 \quad (2.10)$$

We set  $E = 0$  to look at the system in the simplest scenario, without external fields, giving

$$P^2 = \begin{cases} 0 & \text{Paraelectric} \\ \frac{-\beta \pm \sqrt{\beta^2 - 4\alpha\gamma}}{2\gamma} & \text{Ferroelectric} \end{cases} \quad (2.11)$$

We can then look at two separate cases based on the sign of the second term  $\beta$ .

### 2.2.3.1 First-order, $\beta < 0$ and $\gamma > 0$

For  $F$  to remain positive while  $\beta < 0$  we need the next term  $\gamma > 0$ ; we will continue to neglect higher order terms as they are increasingly small. As  $\beta$  is negative, we can drop the “ $-$ ” term in equation 2.11. Above  $T_1$  the free energy will have no minimums outside  $P_s = 0$  as the term inside the square root becomes negative. Then

$$P_s = \begin{cases} \pm \sqrt{\frac{-\beta + \sqrt{\beta^2 - 4\alpha_0\gamma(T-T_0)}}{2\gamma}} & T < T_0 \\ 0, \pm \sqrt{\frac{-\beta + \sqrt{\beta^2 - 4\alpha_0\gamma(T-T_0)}}{2\gamma}} & T_0 < T < T_1 \\ 0 & T > T_1 \end{cases}$$

where  $T_1$  is the ferroelectric temperature limit. For  $T_0 < T < T_C$  the two non-zero terms have lower free energy than  $P_s = 0$ , while for  $T > T_C$  the absolute minima occurs at  $P_s = 0$ . We can find the Curie temperature  $T_c$  by setting  $F(P_s = 0) = F(P_s = \pm\sqrt{\cdot}) = 0$  and solving

$$T_C \approx T_0 + \frac{3\beta^2}{16\alpha_0\gamma}$$

We can do the same for  $T_1$  as  $F(P_s) = 0$

$$T_1 = T_0 + \frac{\beta^2}{4\alpha_0\gamma}$$

Allowing us to confirm  $T_0 < T_C < T_1$ . [16, 20] Figure 2.5a shows the free energy as a function of electric fields; as well as 2.6b the progression of the order parameter  $P_s$  as  $T$  is increased from  $T_0$ ,  $T_C$ , to above  $T_1$ . Adding the electric field back in will create an asymmetry in the free energy and increase  $P_s$ .

### 2.2.3.2 Second-order, $\beta > 0$

For the second case we assume  $\beta > 0$ . When  $T > T_0$  we neglect the  $\beta$  and higher terms as  $P$  is small, there can be only one minimum in equation 2.10 and the shape of  $F$  is

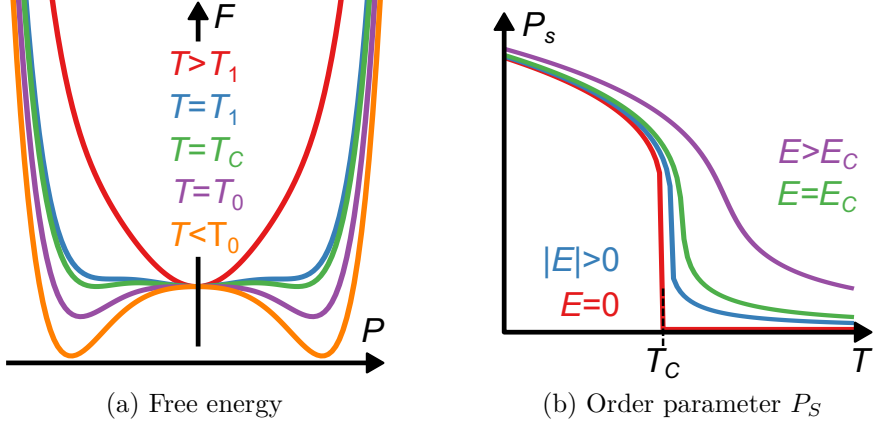


Figure 2.5: Landau first order transition

(a) The free energy as a function of polarization at constant temperature and zero electric field for a first order transition. As  $T$  increases the minimums at finite polarization increase and disappears above  $T_1$ . (b) The value of the parameter  $P_s$  as a function of increasing temperature and constant electric fields.

parabolic. For  $T < T_0$  we start with equation 2.11 and Taylor expand the term under the square root, noting  $P^2 > 0$  this gives

$$P = \begin{cases} 0 & T < T_0 \\ \sqrt{\frac{\alpha_0(T_0-T)}{\beta}} & T > T_0 \end{cases} \quad (2.12)$$

we can also find this result dropping the  $\gamma$  and higher terms in equation 2.9. [16, 20] Below  $T_0$  then  $F$  becomes quartic in shape with a double well. Figure 2.6 shows the free energy above and below  $T_0$ , and the behavior of the minimum(s) in  $F$  with increasing temperature. Above the critical field  $E_c$  the minimum polarization transitions from discontinuous to continuous.

## 2.2.4 Ferroelectric field-effect transistors (FeFETs)

Ferroelectric field-effect transistors (FeFETs), 1T cell, seek to keep a persistent on/off binary state. A ferroelectric dielectric replaces the typical oxide gate dielectric of a (MOS)FET, using the gate to switch the polarization of the crystal, figure 2.7a. The polarization of the material should maintain an electric field along the junction with the semiconductor, providing the normal enhancement or depletion of the channel. As a normal FET, a conducting channel is “on” and conversely, current reduced below a

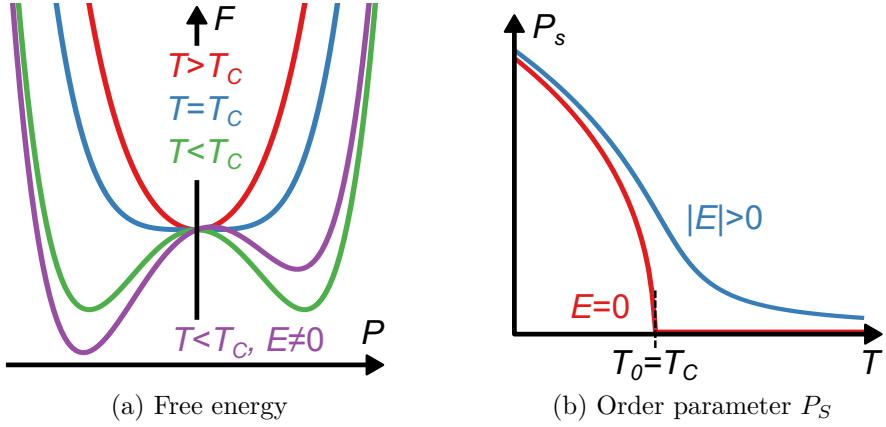


Figure 2.6: Landau second order transition

- (a) The free energy as a function of polarization for a second order transition. All electric fields are zero except for the line indicated. (b)  $P_s$  as a function of increasing temperature and constant electric fields.

threshold can be considered “off.” While as the polarization persists the channel state should remain on or off, sustaining it without power. This has the potential to replace or augment DRAM in computers and low power devices, reducing active energy consumption or possibly allowing electronics to turn on without a lengthy start. FeFETs also offer the possibility of faster switching than traditional capacitor-based RAM [22].

The presence of dipoles within the dielectric layer produces a hysteresis in the current-gate voltage relationship of a FET, figure 2.7b. Increasing the gate voltage to the “on” state of the creates an electric field across the ferroelectric. The electric field increases the carrier concentration within the semiconducting layer, forming a channel between the source and drain contacts [23]. Once the coercive electric field is reached, the dipoles begin to align, creating a larger voltage drop across the ferroelectric dielectric, figure 2.7d. When the voltage across the gate is reduced to 0 V the polarization continues to provide an electric field at the surface and maintaining the conduction channel and the “on” state, figure 2.7c. Further decreasing the gate voltage to the “off” state subsequently polarizes the dielectric in the opposite direction, figure 2.7e. The electric field of the gate depletes the channel of carriers, giving the desired diminutive drain current. When the gate voltage is again returned to 0 V the polarization preserves the depletion field within the channel until the gate is switched to “on” again, figure 2.7f [22, 24]. For both the “on” and “off” states the multiple factors causes the polarization to decay once the electric field is reduced below the threshold of the coercive field, eventually leading to

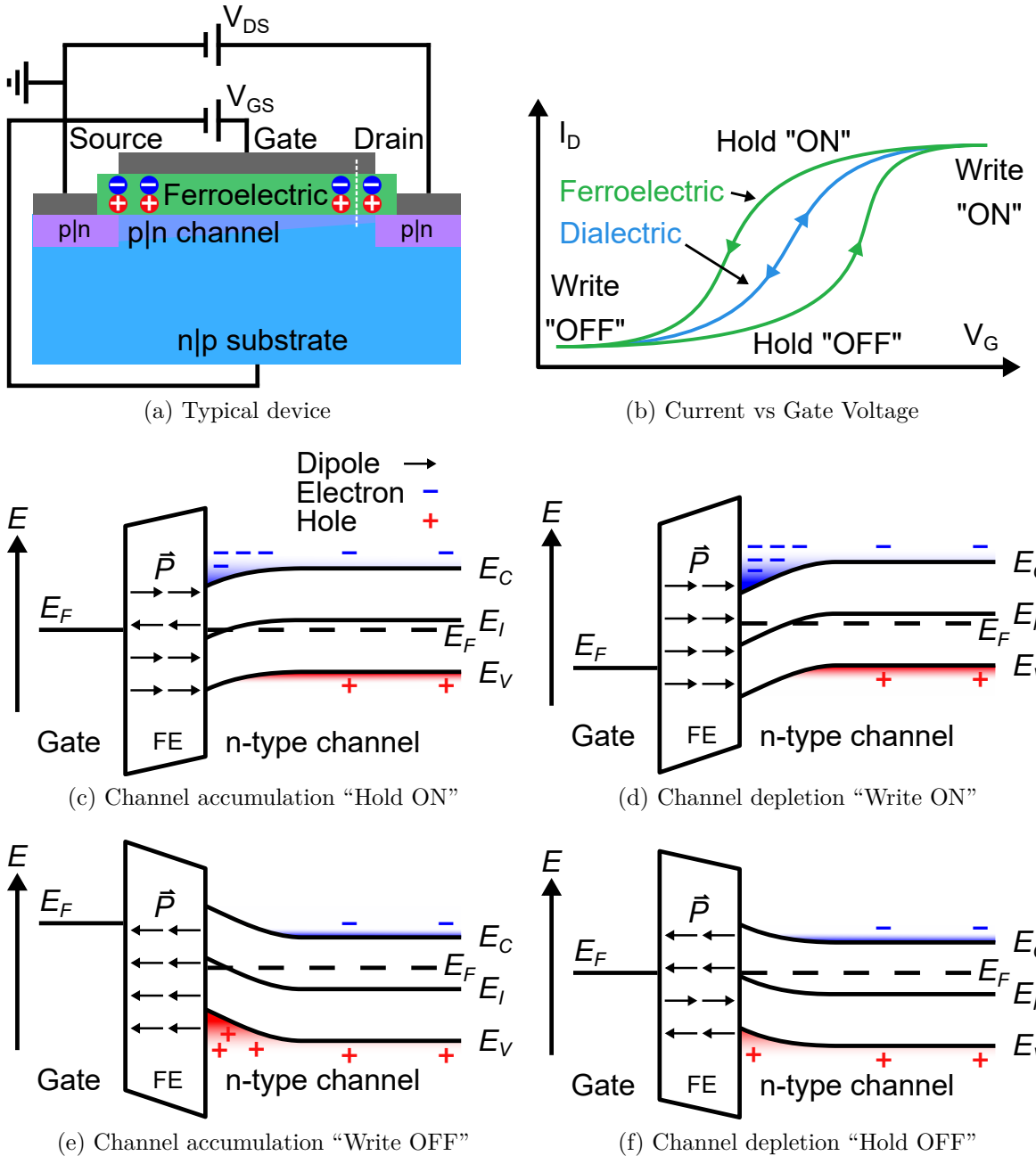


Figure 2.7: Ferroelectric field effect transistors

(a) A typical FeFET device. (b) Source-drain current of the FeFET while increasing the gate voltage from negative to positive and back, a typical FET dielectric response without the ferroelectric deviation is shown in the center. Simplified energy band diagram of the gate-ferroelectric-channel matching the cross section in (a) for "hold ON" (c), "write ON" (d), "write OFF" (e), and "hold OFF" (f) stages of the FeFET show in (b).  $E_F$ ,  $E_c$ ,  $E_I$ ,  $E_v$  are the Fermi energy, conduction band, intrinsic band, and valance band respectively.

the depolarization of the device.

One of the practical challenges of FeFETs is increasing the longevity of the polarization state. Often thermal energy may cause the polarization to relax over time as the dipoles reorient so materials must be chosen to minimize this effect. Likely the largest cause of long term polarization degradation is leakage current through the gate [22]. A common modification of FeFETs is to include a dielectric layer between the ferroelectric and semiconductor to improve the interface between the two (MFIS-FET) and reduce leak currents higher energy electrons from damaging the ferroelectric. Another is to add a floating metal and dielectric layer forming a metal-ferroelectric and channel (MFMIS-FET) to redistribute the electric field evenly over the channel and reduce the effect of domain formation within the ferroelectric. Improving film quality to reduce trapped charges, increasing the metal-ferroelectric Schottky barrier, and using a high-k dielectric can be used to further reduce leak currents in a FeFET [22]. Another common challenge with producing a commercial FeFET RAM is fatigue in the ferroelectric layer as conventional RAM is expected to be able to switch  $\sim 10^{12}$  in its lifetime [22].

### 2.2.5 Ferroelectric tunnel junctions (FTJs)

Ferroelectric tunnel junctions (FTJs) are an alternative to FeFETs being explored for data storage [16]. They consist of a thin ferroelectric in between two metal electrodes, where the ferroelectric polarization is along the axis of the metal-ferroelectric-metal structure, figure 2.8a [25, 26]. The polarization direction will produce a net positive and negative charge distribution in the ferroelectric along the respective electrode junction, figure 2.8c. The electrons in the metal will adjust to screen out the charge at the junction, all together producing a varying potential across the junction. When a voltage is placed across the FTJ some electrons will tunnel through the barrier forming a measurable current. The voltage produces an electric field across the ferroelectric, and if large enough will cause the polarization to switch. The switched polarization will alter the potential across the two junctions and the tunneling current. By measuring the current at a particular voltage it is possible to determine which direction the polarization is orientated giving rise to a binary state that can be used to store information. If the voltage is kept below the coercive field the FTJ will act similar to a non-ferroelectric junction allowing the current state to be read out without being overwritten. Figures 2.8e and 2.8f show two possible resistive switching behaviors, the first with symmetric electrode-ferroelectric interfaces, the second with asymmetric interfaces.

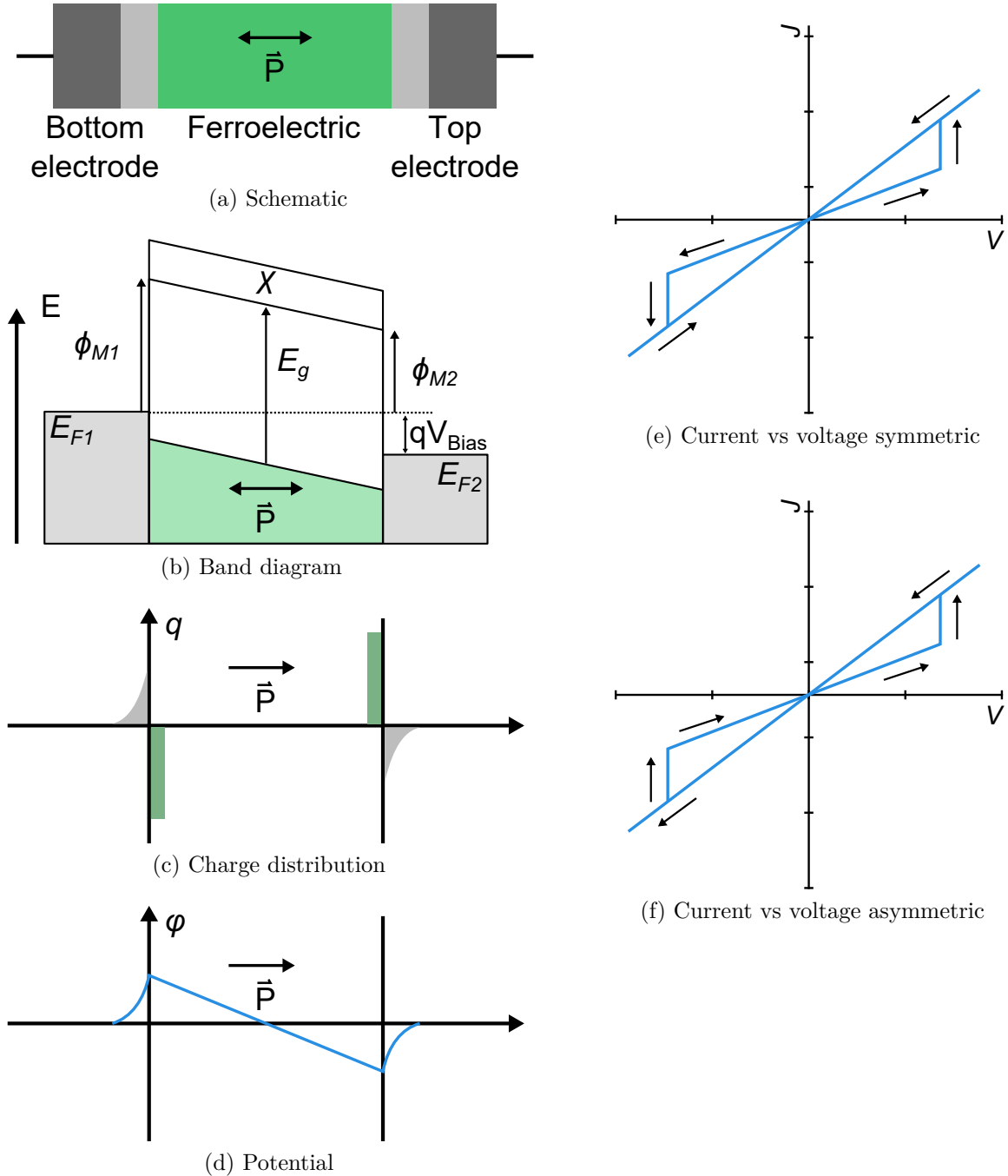


Figure 2.8: Ferroelectric tunnel junctions

FTJ schematic (a) with top and bottom electrodes and depleted regions. Corresponding upward biased band diagram (b) where  $q$  is the fundamental charge,  $V_{bias}$  is the bias across the electrodes,  $E_g$  is the ferroelectric band gap,  $E_F$  the Fermi energy,  $\chi$  is the electron affinity,  $\phi_M$  is the barrier height. (c) charge distribution and (d) potential with the FTJ in an upward polarization. Current density vs voltage of a FTJ with (e) symmetric (f) asymmetric electrode-ferroelectric interfaces.

## 2.2.6 Polar metals

Polar metals, metals that contain dipoles, were first proposed in 1965 [27] to explain the structural transition in  $V_3Si$  but only recently seen experimental verification in  $LiOsO_3$  [28]. Polar metals must show a continuous phase transition from non-polar to polar at their Curie temperature [29] breaking inversion symmetry. As metals have an abundance of free charge carriers, the electric fields within the material are screened, suggesting that metallicity is the antithesis to both prerequisites in the traditional definition of ferroelectricity. The carrier screening suppresses long-range coulomb interactions necessary for dipole formation and the fields to orient the dipoles.  $LiOsO_3$  was shown to shift from  $R\bar{3}c$  to  $R3c$  at  $T = 140\text{ K}$  by the shifting of the Li ion [28], forming a similar structure to several insulating ferroelectrics, and accompanied by several changes in the optical and electronic properties attributed to the dipole formation [28, 30–32]. Similar dipole formation has been seen in  $Ca_3Ru_2O_7$  [33],  $BaTiO_3$  [34],  $LaAuGe$ ,  $LaPtSb$  [35] and other materials. Ferroelectricity was reported in 2-3 layer  $WTe_2$  [36], a 2D Van der Waals chalcogenide metal. The 2D material was stacked between two insulating layers of hexagonal Boron Nitrite ( $hBN$ ) in a double-gated FeFET. The gating response showed a clear transition behavior in  $WTe_2$  conductivity while the thin graphene layers used to gate the material showed a hysteresis in their conductivity, both are attributed to the polarized electric field from the  $WTe_2$ . Later measurements demonstrated the existence of ferroelectric domains with bulk crystals and thin films [37].

The free carriers in a polar metal may move to the edges of the material, to the excess electrical charge normally found on the surface of insulating ferroelectrics, instead producing a neutral charge distribution. This freedom can remove the depolarization field found in a typical ferroelectric [33] possibly extending the polarized state of the crystal. The charge screening also lowers the system energy from domain walls of different dipole orientations in close proximity, allowing for opposing polarization domains to form  $1\text{nm}$  apart with only  $10\text{s}$  of  $\text{meV}$  potential difference [38]. Potential polar metal applications include reducing the size of ferroelectric capacitors [39], FeFETs [36], tunnel barriers [40], and nonreciprocal charge transport [41].

## 2.2.7 FeFETs with ferroelectric channels

TODO

## 2.3 2D materials

Started by the discovery of graphene, 2D materials have become a large area of research due to their unique qualities and ability to integrate with conventional electronics. Typically defined by layered nature, many can be mechanically exfoliated to small crystals or grown as thin films. The sharp reduction in one dimension often provides additional fundamental electronic properties from the bulk that can be exploited. Chalcogenides, typically sulfides, selenides, tellurides; often form 2D materials with Van der Waals inter-layer bonding with a semiconductor bandgap. Some of the most studied of these compounds are the transition metal dichalcogenides with the stoichiometry  $MX_2$ , where  $M$  is a transition metal such as  $Mo$  or  $W$  and  $X$  a chalcogen  $S$ ,  $Se$ , or  $Te$ .

### 2.3.1 Trapped charge in 2D FETs? (TODO)

2D FETs have a high in-plane to out-of-plane ratio, as devices can be made on several nanometer thick films or flakes, forcing surface properties to play a large role in the behavior of a device. This often manifests in a hysteresis of the source drain current to changes in FET gate voltage, the origin of which is still an area of active research.

TODO

Fermi pinning?

### 2.3.2 In-Se compounds

Indium-Selenium together can form a variety of binary compounds ranging with completely disparate properties. Depending on the temperature and prevalence of each element it is possible to get different In-Se alloy growth and structure. Figure 2.9 shows a phase diagram compiled from various experimentally published sources up to 2003 as well as calculations. The plethora of compounds, and the sensitivity to both temperature and concentration, makes growth of a single uniform compound harder to control. Alternate configurations of the same stoichiometry have made past literature somewhat inconsistent as each configuration may have unique properties while the specific configuration was not reported.

#### 2.3.2.1 $In_2Se_3$ polymorphs in literature

$In_2Se_3$  is perhaps one of the most complicated of the In-Se compounds. Currently there are thought to be  $\alpha$ ,  $\beta$ ,  $\gamma$ ,  $\delta$ , and  $\kappa$  stable phases of  $In_2Se_3$ , in addition to  $\alpha'$ ,  $\beta'$ , and

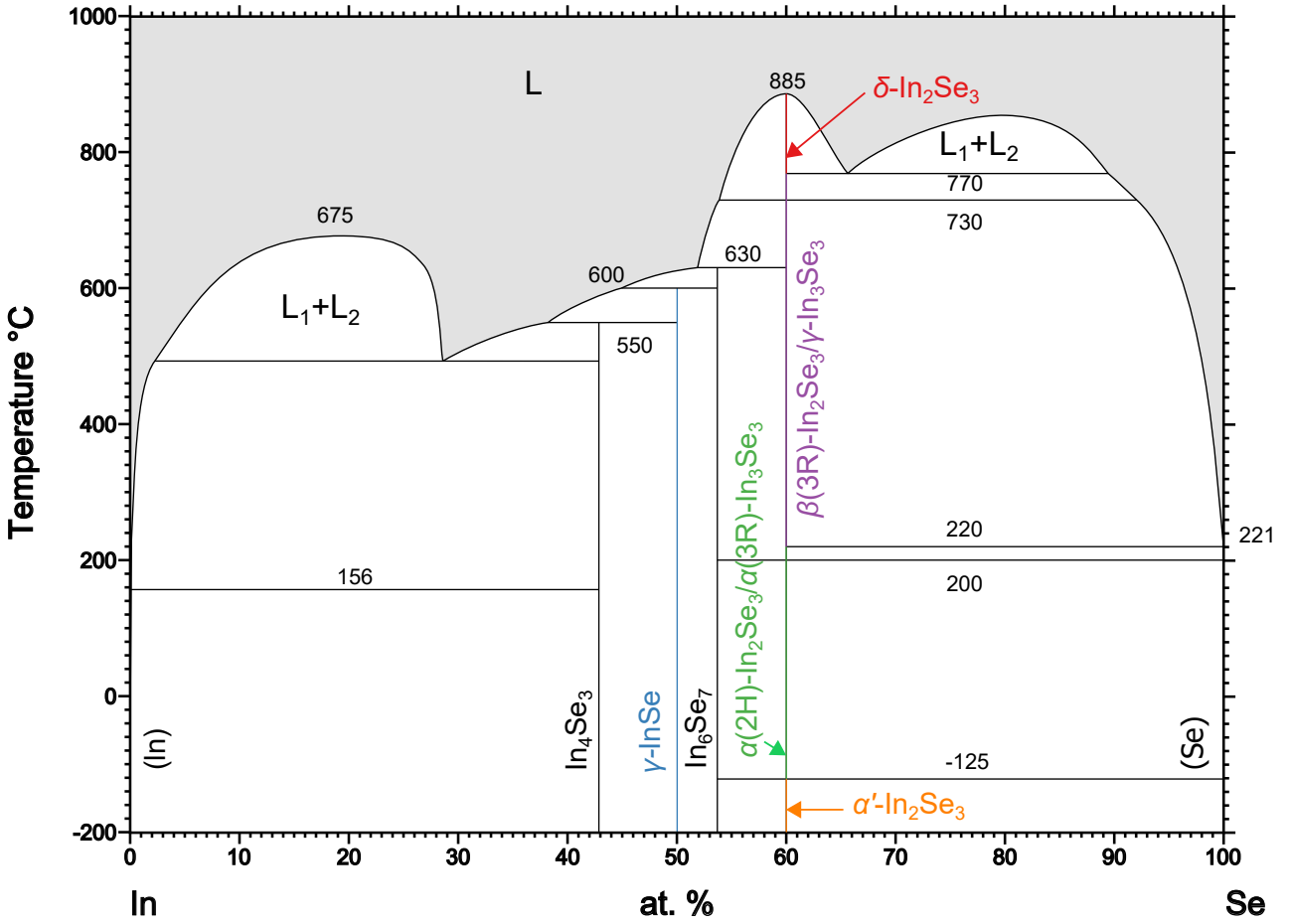


Figure 2.9: In-Se alloy phase diagram.

The various Indium-Selenium compounds grown from literature using both experimental and calculated data. Compiled by ref [42].

$\gamma'$  metastable phases [43]. Ref [44] is likely the most comprehensive single study of the  $\alpha$ ,  $\beta$ ,  $\gamma$  phase structures currently reported.  $\alpha$ ,  $\beta$ ,  $\delta$  and  $\kappa$  are 2D layered Van der Waals materials while  $\gamma - In_2Se_3$  is 3D in nature.  $\alpha$  and  $\beta$  are semiconductors and have multiple sub-polymorphic structures with different layer stacking.  $\kappa - In_2Se_3$  is typically formed by doping with impurities like Ag, Sb, Te, and Zn, and is similar to the  $\alpha$  phase [45, 46, 46, 47]. It is possible to transform among the different polymorphs using pressure, heat, electric potential, or other techniques. This has somewhat added to discrepancies in the literature as one type will be determined then the properties of the material measured after or during annealing when the material changes phases.  $\alpha'$  was made by cooling  $\beta'$  [48].  $\beta'$  forms under pressure from  $\alpha$  [?] or at lower temperatures from  $\beta$  [48]. Last,  $\gamma'$  was formed from heating the  $\beta$  polymorph [49]. Table 2.1 lists the different polymorphs reported in literature and the identified space groups.

Polymorph	Structure	Space group {number}
$\alpha$	Rhombohedral [3R]	$R\bar{3}m \{160\}$ [?, 44, 50–53] (or $R\bar{3}m \{166\}$ [54–56])
	Hexagonal [2H]	$P6_3mc \{186\}$ [?, 44] (or $P6_3/mmc \{194\}$ [54]) [57]
$\beta$	Trigonal [1T]	$P\bar{3}m1 \{162\}$ [44]
	Hexagonal [2H]	$P6_3mc \{186\}$ [44] (or $P6_3/mmc \{194\}$ [58])
	Rhombohedral [3R]	$R\bar{3}m \{166\}$ [?, 51, 52, 54, 56, 58, 59]
$\gamma$	Hexagonal	$P6_1 \{169\}$ [44, 60–62] (or $P6_5 \{170\}$ [44, 57, 60, 63]) [58, 64]
$\delta$	Trigonal	$P\bar{3}m1 \{156\}$ [58] or $P3m1 \{164\}$ [54, 59]
$\kappa$	Hexagonal	[45, 46, 46, 47, 65, 66]
$\alpha'$	Rhombohedral	$R\bar{3}m \{160\}$ [59]
$\beta'$	Monoclinic	$C2/m \{12\}$ [52]
	Rectangular	[67, 68]

Table 2.1:  $In_2Se_3$  polymorphs

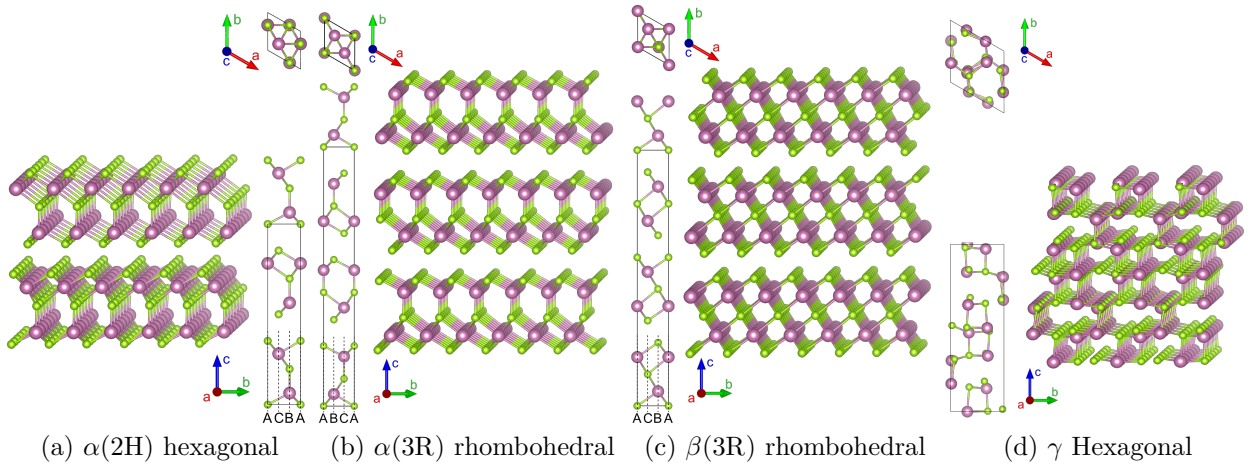


Figure 2.10:  $In_2Se_3$  crystal structure

$\alpha$  (2H– $P6_3mc$ ) [50],  $\alpha$  (3R– $R\bar{3}m$ ) [50],  $\beta$  ( $3R$ – $R\bar{3}m$ ), and  $\gamma$  ( $P6_1$ ) crystal stuctures.

TODO: Ferroelectricity in  $In_2Se_3$ ? (TODO, maybe leave for later chapter)

Maybe:

Polymorph	Structure	Spac group
$\beta$	Hexagonal	$P6_3/mmc$ [69]
$\gamma$	Rhombohedral	$R\bar{3}m$ [69]
$\varepsilon$	Hexagonal	$P\bar{6}m2$ [69]

Table 2.2: *InSe* polymorphs

# **Chapter 3 |**

# **Sample fabrication and measurement methods**

This chapter serves as an overview of the experimental techniques used or referenced in other chapters. A brief summary of each technique and some of the relevant applications to the overall discussion are described. For some methods, additional specific details are given in an effort to make any reproduction of experimental results or other future works as efficient as possible. A description of the reasoning behind a few experimental choices are also provided for context.

## **3.1 Introduction**

The relatively simple innovation of using adhesive tape to exfoliate van der Waals crystal spearheaded a boom in 2D material research and driven the development of new techniques to explore these materials. 2D crystals are typically manufactured in one of two methods: films grown on premanufactured substrates or exfoliated flakes from van der Waals crystals. Films are sought for material commercialization as they can be incorporated into large-scale manufacturing processes. Industrial scale process require a lot of time to development to insure the film can be grown uniformity, using a reliable process that scales and is cost effective. Exfoliated crystals are typically used in initial material development and characterization as they are often easier to produce and faster to work with on small scale initial devices. By growing a bulk crystal, the parameters of the substrate lattice are removed from the crystal growth, reducing many complications seen in film development. Due their self-contained nature, flakes can be easier to physically manipulate when developing a new process as they are not bonded to a substrate. Flakes may additionally be stacked in layered hetrostructures to create

devices with more unique properties, and can display new phenomena such as interface effects between the layers. Advances in flake devices often drive development of film manufacturing to incorporate the 2D crystal properties into commercial devices.

Both flake and film device manufacture follow similar processes to add wires or pattern the crystal by etching. Figure 3.1 shows an example of the two different processes while the details of each are given in the respective sections below. For most films and some flakes any unwanted material must first be removed to reduce the crystal down to the desired size and shape. The substrate is first covered with a protective polymer resist that forms a uniform coating over the entire surface. The polymer is patterned using photo or electron-beam lithography process to leave only the desired material covered. The excess crystal is then removed using an etching process, this can be using something like a gas-plasma or a wet process with a chemical that reacts with the crystal, such as a strong acid. The chemical etch can often destroy the protective layer or begin to eat through the exposed sides, so the duration and method of the etch must be considered. The polymer is then removed with solvents so only the patterned crystal remains on the substrate. For adding wires to the the crystal, substrate is (again) covered with a protective polymer and patterned, exposing the surfaces to be covered by metal contacts. Typically the wires will cover a portion of the crystal top and a small sidewall, then extend into other parts of the substrate to connect to other crystals or expose the wires. Metal is evaporated, sputtered, or otherwise deposited onto the surface to adhere to the exposed surfaces of the crystal and substrate. The polymer is dissolved, taking with it the excess metal deposited on the polymer, and leaving only desired metal leads. This process can be repeated after additional crystals are added, allowing us to create complex devices with layered crystals, each with their own contacts.

## 3.2 Flake generation

### 3.2.1 Manufacturing alignment marker wafer chips

For fabricating flake devices we chose a wafer platform to work that gave us a near-optimal optical contrast [70] and then added markers for reference locations and align lithography patterns to. We started with 4 inch wafers of  $500\mu m$  phosphorus doped silicon with  $300nm$  of thermally oxidized  $\text{SiO}_2$  as a substrate ( $<100>$  thermal oxide, purchased from Si-Tech) with a mechanically polished surface. The doped silicon allows us to use

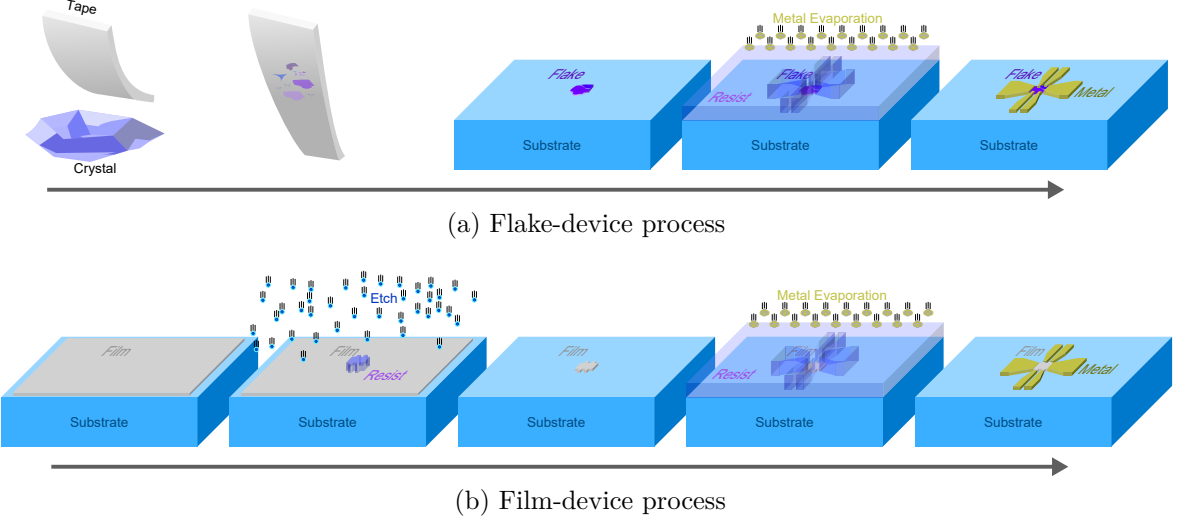


Figure 3.1: Device manufacture.

(a) Flake manufacture of devices. Flakes are exfoliated from a crystal then placed on a substrate. Metal leads are then added to the flake for device measurements. (b) Film manufacture of devices. Film is etched with a protective layer of resist to leave material for device. Metal leads are added for material measurements.

the bulk of the silicon as a conductive gate, and the  $300\text{nm}$  oxide would give a high contrast for most 2D materials under white light. The substrate was cleaned for better adhesion of photoresist polymer. To remove the protective resist added before shipping the wafer is sonicated in acetone for 5 minutes, followed by 5 minutes in 2-isopropanol remove acetone residue, and finally dried using compressed nitrogen gas. Using standard photolithography (see 3.4.1.1) we patterned the surface with a  $\sim 5\text{nm}$  thin layer of titanium for adhesion, then  $\sim 35\text{nm}$  of gold. The metals were laid out with a repeating pattern of numbers and lines, allowing us to record substrate location and easily find a flake on the substrate when moving between tools, figure 3.2a. We spun a protective layer of PMMA resist over the substrate then diced the wafer into  $8\text{mm}$  square chips with a ADT 7100 ProVectus Dicing Saw. This allowed us to make many devices per wafer in one quick process, each chip could then be arranged in a custom orientation and pattern for each flake-device. The resist was then removed from the chips using acetone, 2-isopropanol, and deionized (DI) water then dried with compressed nitrogen. To remove any residue organics we soaked the chips in Nano-Strip (a sulfuric acid and hydrogen peroxide compound, VWR) for 10 minutes, rinsed in DI-water, then repeated the initial solvent clean. After several devices experienced dialectic breakdown across the  $\text{SiO}_2$  we switched the residue clean to an oxygen surface treatment for some devices. This was done in a M4L Plasma Processing System with 300 sccm oxygen, 100 sccm helium, at

500mTorr of pressure, and 100W power for 1 minute.

### 3.2.2 Mechanical exfoliation from bulk crystals to thin flakes

Flakes of van der Waals materials were mechanically exfoliated using Scotch 3M Transparent Tape to break the weaker bond between layers. A piece of tape was pressed into a larger bulk crystal of the material then peeled off, resulting in a few smaller, dispersed crystals. To further cut down on crystal size and increase the surface density the tape is then folded over itself so the crystals are pressed into different areas of tape, ideally without coming into contact with each other and increasing the flake density. The tape was then peeled apart so that the crystals break additional van der Waals bonds and form thinner layered crystals. This process was repeated several times to provide a region of crystal coverage roughly 8 to 10mm in diameter, to match the size of the alignment mark substrate. This region of tape is then pressed into a fresh region of tape, providing a new exposed surface of crystals with less tape residue and further decreasing the flake thickness. This can be repeated to thin the layers of crystal but must be balanced against decreasing tape coverage. The thickness of some materials, such as graphene, can be estimated by their reflectivity on the tape, giving a rough guess of how many times the folding process should be repeated. The tape and crystals are then placed on a cleaned alignment marker chip, ideally maximizing the amount of crystals within the center of the chip, as flakes near the edges can be hard to work with during the lithography and wiring steps. The tape is lightly pressed into the chip with a soft tool so that as much of the crystals as possible are in contact with the surface of the chip. This can cause the flakes to crack so a balance in tool pressure and pattern must be used, and this must be calibrated to the crystal hardness and ease of layer separation. To promote adhesion to the surface, the chip can then be heated for 1-2 minutes at 100C to improve adhesion to the substrate. [71] The chips are then allowed to cool and the tape peeled off, leaving a freshly cleaved surface on both the substrate and top of the flakes. The angle and speed of the tape removal may influence the number and quality of flakes on the substrate, but there is very little control of either when done by hand. Figure 3.2b shows a starting bulk crystal, adhesive tape with exfoliated crystals using the described process, and the final alignment marker chip with flakes.

After exfoliation we scanned each chip for flakes using a Nikon Eclipse LV150 microscope with 10x, 50x and 100x objectives. We chose 300nm of thermally oxidized SiO<sub>2</sub> to increase visibility of 2D materials under white light, a green filter can be used for a monochrome search have a high optical contrast with some 2D materials when only

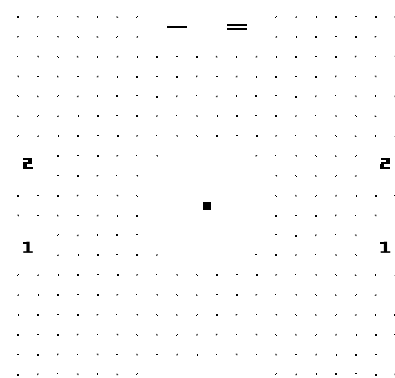
a few layers thick [70]. Flakes are chosen for uniformity (lacking in visible cracks or damage that would impact electronic measurements), thinness, and lateral sizes large enough for photolithography processing. Flake thickness is very hard to judge using an optical measurement and depends on the material used, the lighting, and substrate chosen. To create a rough estimation of thickness we fabricate a color code for new materials while fixing as many microscope parameters as possible. A Bruker Icon Atomic Force Microscope (AFM) is used to measure flake height and later compared against the optical pictures. Below 30nm most of the flakes of various materials became translucent rather than changing color, increasing the difficulty of finding flakes and using optical measurements to estimate flake thickness. Figure 3.2c-e shows the AFM measurement of a flake of  $\alpha$ -In<sub>2</sub>Se<sub>3</sub>, the microscope picture with labeled thicknesses, and final color code created using the maps from several flakes.

For many of the measurements we sought flakes under 10nm down to a single layer as they may display properties not shown in bulk crystals. Care must be taken to distinguish flakes from tape residue which will often appear very similar to thin flakes in color. Flakes may often be distinguished by sharp edges as many 2D materials tend to tear along straight lines, though tape residue can mimic this by adhering to flakes on the tape, then sticking to substrate while the flake remains on the tape. After identification of useful flakes, images were taken using a Nikon Ds-Fi1 camera with increased exposure times using the 100x objective and 10x to record the flake conditions before fabrication and its location relative to markers.

## 3.3 Thin crystal characterization

### 3.3.1 Scanning probe microscopy

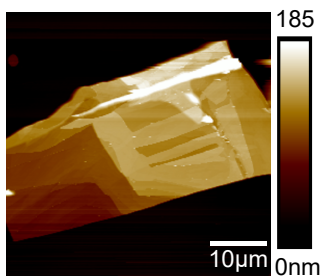
Scanning probe microscopy (SPM) is a series of techniques to produce detailed characterization over a 3D surface. A long, sharp needle of material is held perpendicular to the plane of the surface allowing the SPM to measure the interactions of the tip and surface. The tip is traced across the plane forming a map of the tip-surface interactions. Piezoelectric crystals attached to the tip let the tip move in over short distances in any direction with fine precision. This is often combined with additional motors, such as a stepper motor, can move the entire piezoelectric crystals and tip structure over larger distances but sacrifice precision to do so. With an isolated environment, engineered to shield the tip from external noise, and a sharp tip, a SPM map can provide details down



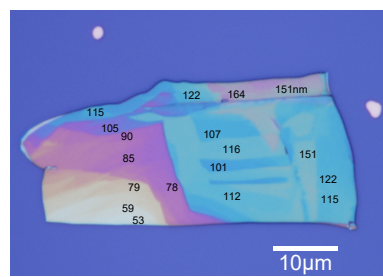
(a) Alignment marker pattern



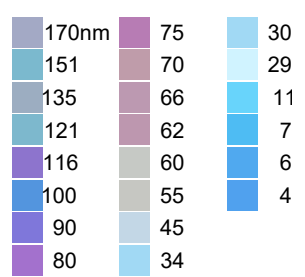
(b) Tape exfoliation



(c)  $\text{In}_2\text{Se}_3$  flake AFM



(d) Optical  $\text{In}_2\text{Se}_3$  flake with thickness



(e)  $\text{In}_2\text{Se}_3$  color code

Figure 3.2: Mechanical exfoliation of thin flakes of bulk crystal

(a) Photograph, from left-to-right: the starting bulk crystal, transparent tape with exfoliated thin flakes of crystal, and Si/SiO<sub>2</sub> alignment marker substrate with flakes. (b) One square of alignment marks used to pattern the substrate. The marks formed a repeating pattern of six numbers in both directions; with the overall pattern repeated four times on a chip. (c) An atomic force microscope height measurement of a flake of  $\alpha$ -In<sub>2</sub>Se<sub>3</sub>, the map was used to mark an optical image of the flake (d) with the corresponding thicknesses, and then create a partial color code (e) for  $\alpha$ -In<sub>2</sub>Se<sub>3</sub>.

to the atomic level. There are many different varieties of SPM that measure quantities like magnetic field, density of states, and spin; and far too many to discuss here, so only a brief overview of the most relevant are below. Figure 3.3 shows the typical setup of most SPM microscopes.

### 3.3.1.1 Atomic force microscopy

Atomic force microscopy (AFM) is used to measure detailed topographical information from 3D surfaces with small variations in height. The tip is fixed to a small, flexible cantilever and the cantilever is extended horizontally over the surface so that the tip

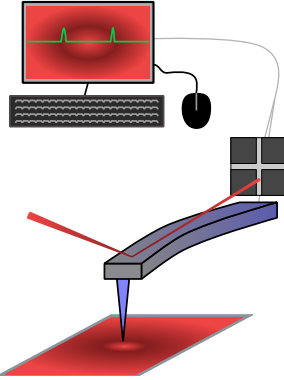


Figure 3.3: Atomic force microscope

An atomic force microscope tip on a cantilever extends over a 3D surface with varied topography. The relative deflection of the tip is measured by a laser reflected off the back of the cantilever to a photodetector capable of measuring the shifts in the horizontal and vertical as the cantilever bends and twists.

points perpendicular between the cantilever and surface. The tip interacts with the surface will cause the cantilever to bend and twist. To measure the movement of the cantilever and tip a laser aligned to reflect of the top of the cantilever. The top of the cantilever, polished for this purpose, reflects the laser to a photodetector. As the cantilever flexes and tilts the reflected laser moves across the photodetector, optically measuring the tip deflection with great precision. The AFM computer monitors the tip deflection as it traces the tip across the surface, and can modify the movement in a feedback loop to increase measurement precision. Because the tip deflection is dependent on the materials involved and other interaction conditions, an AFM scan is not a true topography map of the surface, but for most purposes they are near-indistinguishable and it is typically treated as a topography measurement for most purposes. [72]

There are different methodologies of AFM measurement, though all measure some form of force interactions between the tip and the surface. As the tip is brought close to the surface it is initially repelled by the van der Walls forces, but as the distance continues to decrease the force becomes attractive, pulling the tip towards the surface. The original method, contact AFM, keeps the tip in the attractive region of the force interactions as it moved across the material surface, figure 3.4a. The cantilever force is kept constant by moving the cantilever holder up and down to maintain the deflection, making the holder z-position a measurement of the surface topography. Keeping the tip in contact during lateral movements can damage soft materials and the tip thus distorting the image, but allows for faster measurements and high resolution [72]. To avoid the surface and tip damage, tapping mode AFM was devised, which keeps the tip

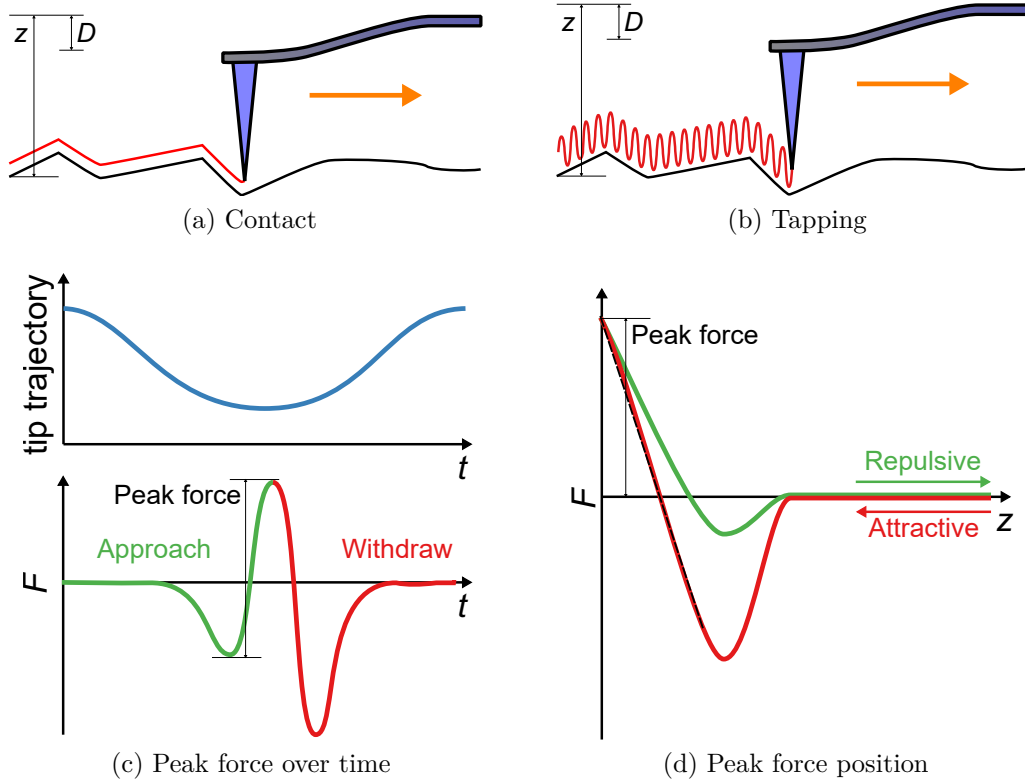


Figure 3.4: AFM interaction modes

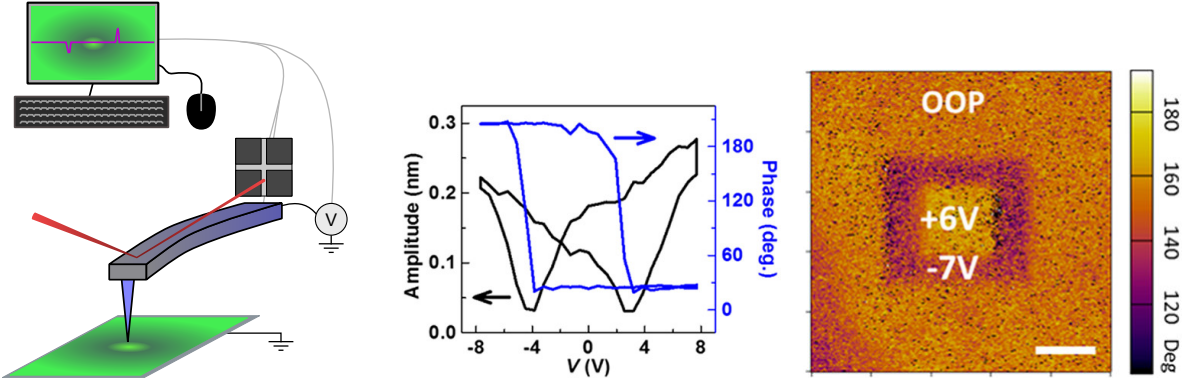
(a) Contact and (b) tapping mode tip movements of an AFM during a topography scan. (c) the tip trajectory over time and the forces on the tip while moving along that trajectory. (d) the forces on the tip relative to the cantilever position, showing the hysteresis in tip forces as the tip switches between repulsive and attractive regimes. [73]

at longer distances from the surface during lateral moves. In tapping mode the cantilever is driven to oscillate at or slightly below its resonant frequency and lightly taps the surface to measure height, figure 3.4b. Tapping mode monitors the amplitude of the cantilever as it oscillates, keeping it constant as the tip is scanned, providing the height measurement [72]. Non-contact AFM moves the tip farther from the surface than tapping mode, so the tip is operating in the repulsive force range. The repulsive forces in this range are weaker, so to increase measurement precision the frequency is used in place of the amplitude to monitor tip forces. In this mode the cantilever is driven at or slightly above its resonate frequency. As the tip approaches the surface the forces cause cantilever to shift in oscillation frequency. By adjusting cantilever height to keep the frequency constant during a scan we again have a measurement of surface topography. This has the lowest resolution of the three modes and is the slowest, but has the least chance of interacting with the surface, keeping tip and sample damage to a minimum [72].

The last tapping mode we will discuss, peak force tapping, measures the force-tip-distance curve as the cantilever is brought close to the surface and then pulled away. The cantilever is driven well below its resonant frequency, avoiding the need to tune the cantilever as in the previous modes and reducing some complexity in the measurement setup. The tip oscillates the surface, similar to the last two modes. As it moves the Van der Waals force switches between repulsive, attractive, and then back to repulsive, figure 3.4c. The force curve forms a hysteresis loop with respect to distance, figure 3.4d. The continuous monitoring of the force curve allows the AFM to keep the force below a set threshold thus minimizing the damage to sample and tip. The difference between the maximum (peak) force on tip as it is contact with the surface and the tip fully withdrawn is kept constant as the AFM scans the surface, providing the topography map of the surface [73]. All AFM measurements reported in this text were done using peak force tapping on a Bruker Dimension Icon AFM with ScanAsyst tips (Bruker Scanasyst-Air). All images generated and height analysis was done in the software Bruker NanoScope Analysis (v2.0).

### 3.3.1.2 Piezoresponse force microscopy

Piezoresponse force microscopy (PFM) is an extension of AFM that looks at the electronic response of a surface topography. While none of the experimental work in this text contains any PFM data, it is an important tool in identifying ferroelectricity in thin films and 2D flakes, so we discuss it in that context. PFM uses a conductive AFM tip and cantilever, often through and added metallic surface coating or itself metallic, electrically connected to an external voltage source. Samples are connected to the same circuit ground, typically by including a conductive substrate or material layer underneath. The tip is placed in contact with the material to form an electric field like two plates of a capacitor. As the name suggests, PFM measures the piezo-deformation response of the sample as a voltage is applied between the sample and tip. This includes movement in the z-direction through vertical tip deflections, along with in plane shearing through the twisting of the cantilever as the sample moves. Combined, this is used to form a vector map of the responses for materials with complex responses, such as ferroelectrics with multiple polarization axes. An alternating voltage bias is used to drive the electric field, usually by a lock-in amplifier, and the PFM measures the phase difference and amplitude of the tip oscillations. The driving frequency and amplitude used by the PFM can play an important role in the sample response and the signal to noise ratio. [74, 75] One common method, band excitation, uses a multiple frequency wave



(a) Piezoresponse force microscope (b) Phase and amplitude measurement (c) Remnant polarization measurement

Figure 3.5: PFM and ferroelectric materials

a) a piezoresponse force microscope, the configuration is similar to an AFM with a lock-in amplifier and variable voltage source connected electronically to a conductive tip. (b) PFM phase and amplitude measurements on a single point of an 6nm thick  $\alpha$ -In<sub>2</sub>Se<sub>3</sub> flake showing hysteresis typical for a ferroelectric material. (c) remnant polarization in the out-of-plane direction written into a similar flake using a bias tip with +6V and -7V, then read back using an unbiased tip. Scale bar is 1  $\mu$ m. (b-c) Adapted with permission from [78]. Copyright 2018 American Chemical Society.

pack around the cantilever's resonant frequency and the responses combined through a simple harmonic oscillator model into a single measurement. Alternatively, dual AC resonance tracking, uses the difference in amplitude responses above and below the resonant frequency to measure the sample. [74–76] More complex techniques combines both phase and amplitude variance for more accurate measurements in an effort to distinguish ferroelectricity from other phenomena and measurement biases [77].

There are two common PFM techniques commonly used to identify ferroelectricity, namely the observation electromechanical hysteresis loops and remnant states [74]. In the first method, the bias voltage is increased and decreased in a positive to negative loop at a single point on the surface. Past the positive and negative coercive fields, a domain begins to nucleate and spreads out with time and increasing voltage. In ferroelectrics this shows a butterfly-like hysteresis in phase and loop-like hysteresis in amplitude, as seen in figure 3.5b. The second method uses the PFM to manipulate ferroelectric domains in the out of plane direction and their subsequent observation as evidence for the domains. The dipoles of the domain are aligned by scanning regions of the surface with different voltage biases, using the electric fields to form a pattern of different domains. The surface is then scanned again with the PFM at zero bias, which looks for evidence of

the altered ferroelectric domain pattern, like what is shown in figure 3.5c. This is often known as domain writing/reading or observation of remnant polarization states. A square pattern typically chosen is a series of rectangles encompassing one another, but domain manipulation can be used to write complex shapes if the sample dimensions support it. Both PFM techniques can be used to look for the crossover from ferroelectric to paraelectric as temperature crosses  $T_c$ .

Caution must be used when using PFM to identify ferroelectric behaviors as multiple phenomena cause similar responses. A short list of some of the most common follows, and they are discussed in depth elsewhere [75, 79]. The voltage bias from the tip can inject charged particles into the surface of the material, and while they typically dissipate after several hours in an insulator, the injected trapped charges will appear very similar to writing remnant states and hysteresis loops in a ferroelectric. Large currents from the tip to the surface can also cause joule heating, distorting the lattice and can be again picked up from a subsequent PFM scan. Strain gradients from the tip putting pressure on thin crystals can reverse polarization, the flexoelectric effect. The voltage bias from a PFM tip can move ions in a crystal within a unit cell or between cells, the former a characteristic of ferroelectric dipoles while the latter is ionic conduction. Both cause distortion of the crystal structure and are virtually indistinguishable from each other by PFM. At high enough electric fields, amplified by the sharp point of the PFM tip, the surface chemistry can be altered through electrochemical reactions, especially with oxides. These changes can be either reversible or irreversible, even within the same material using different voltages. [75, 79] There are other less common pit-falls not listed here, and ways to mitigate some of the problems mentioned, but both are beyond the scope of what should be discussed here. PFM should almost never be taken as complete proof that a material is ferroelectric, but still can be an excellent tool to used to study properties of ferroelectric materials such as domain propagation.

### 3.3.2 Optical second harmonic generation

A process frequently used to study crystal structure and material properties is optical second harmonic generation (SHG). A single frequency laser is used to measure the crystal medium. As can be inferred from its name, pairs of photons interact with the medium and generate photons at twice the initial frequency. Keeping to the electric field contribution, this nonlinear process is described mathematically as

$$P(2\omega) = \chi^{(2)} E(\omega) E(\omega) \quad (3.1)$$

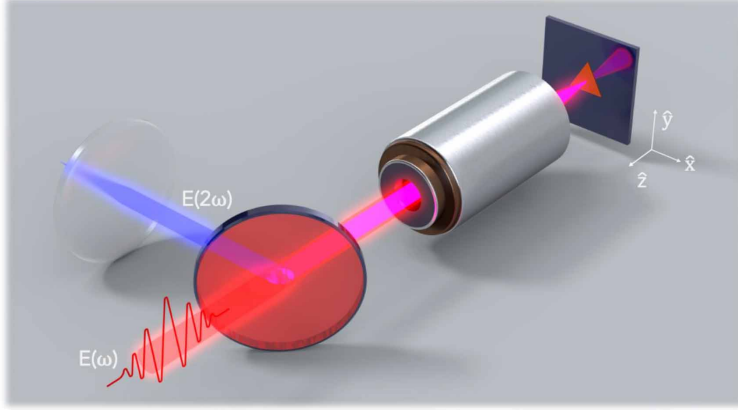


Figure 3.6: Optical second harmonic generation

Schematic of an optical second harmonic measurement setup. Laser light (starting from the left left) passes through a dichroic mirror and is focused on a crystal medium. Generated light is reflected back through the lens and partially reflects off the mirror (to the top left) so that the intensity of the generated-reflected light may be measured. Used with permission of IOP Publishing, (ref [83]) “Second harmonic generation in two-dimensional transition metal dichalcogenides with growth and post-synthesis defects,” Murray et al., 2D Materials, 7(4), 2020; permission conveyed through Copyright Clearance Center, Inc.

where  $P$  is the induced dipole per unit volume,  $E(\omega)$  the electric field from a photon with frequency  $\omega$ , and  $\chi$  the three-rank nonlinear susceptibility tensor of the material [80]. If we approximate  $\chi$  in a multipole expansion

$$\chi^{(2)}(\omega, \vec{q}) \approx \chi_{ED}^{(2)}(\omega) + \chi_{EQ}^{(2)}(\omega) + O(\vec{q}^2)$$

where  $q$  is the wave vector of the incident photon,  $\chi_{ED}$  is the electric dipole contribution, and  $\chi_{EQ}$  electric quadrupole [81]. Typically the quadrupole response is much smaller than the dipole, though it can still be measured and gives valuable information about some crystal structures, but we can neglect it for this discussion. The  $\chi_{EQ}$  tensor is constrained by several symmetries giving it just 10 independent parameters, but most importantly it goes to  $\chi_{EQ,ijk} = 0$  in a centrosymmetric system. As ferroelectricity can only exist in non-centrosymmetric systems, SHG response is an important test to see if a crystal is a possible ferroelectric material. [81] While it can not identify ferroelectricity, SHG can quickly screen out non-ferroelectric materials, and can measure 2D crystals down to a single layer [82]. Figure 3.6 shows a simplified setup of how this can be done in practice.

One of the notable advantages of SHG is its ability to measure materials down to

a single layer thick. SHG intensity scans across a material may be used to identify structural transitions such as grain boundaries [83]. At a grain boundary or defect, photons can interfere with each other destructively resulting in a decrease in output intensity compared to a uniform crystal. Another area in which SHG excels is identifying phase transitions, such as a paraelectric to ferroelectric temperature transition, though the slope of the change in response intensity. [84]

Using polarized light, the SHG measurement of the electric dipole term can help determine the spacial symmetry of a crystal. [85] The intensity of the light response is given by

$$I_{\parallel} = I \cos^2(3\theta) \quad (3.2)$$

$$I_{\perp} = I \sin^2(3\theta) \quad (3.3)$$

where  $\theta$  is the angle between the laser light and the crystalline armchair direction,  $I_{\parallel}$  and  $I_{\perp}$  are the parallel and perpendicular polarization-resolved intensity. [86] Polarization resolved SHG is often used in place of TEM and other more resource intensive tools to identify crystal polymorphs as it can be done quickly and cheaply. A Ti:Sapphire femtosecond laser (150 fs, 80 MHz) with a wavelength centered around  $\lambda = 800\text{nm}$  was used for the measurements reported here, along with a  $\lambda/4$  wave plate to followed by a linear polarizer that could be freely rotated for both the excitation and generated photon beam [87].

### 3.3.3 Raman (TODO: review)

Another optical process often used for crystal characterization of 2D materials is Raman spectroscopy, that uses the inelastic scattering of photons to measure vibration modes in the material. A laser is used to excite electrons in into a higher virtual energy state. Most electrons will drop back down to the initial energy level and emit a photon with the same frequency as the initial photons, a process known as Rayleigh scattering. A small percentage of the electrons will interact with phonons or other excited states. When those electrons return to a lower energy level they emit a photon with lower (higher) energy and frequency in a process known as (Anti-)Stokes scattering. To quantify this, the frequencies of emitted light light are spatially separated using a diffraction grating and their relative intensity recorded. [88–90] Figure 3.7a shows the three aforementioned scattering mechanisms and 3.7b a simplified Raman setup.

The resulting light forms distinct peaks at different frequencies that correspond to

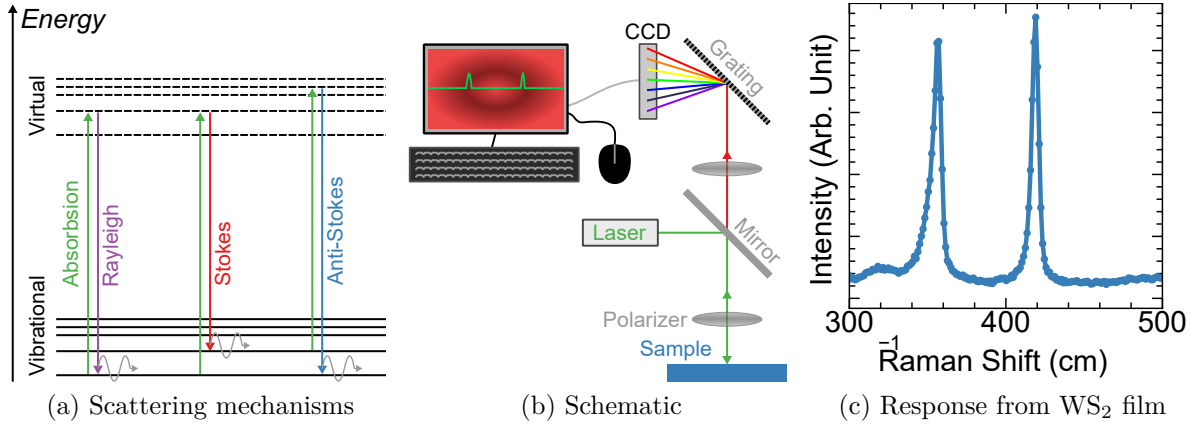


Figure 3.7: Raman Spectroscopy

(a) Three of the scattering mechanisms of monochromatic light seen in Raman spectroscopy measurements: Rayleigh, Stokes, and Anti-Stokes. Each absorbs a photon for a charge particle to reach an excited state in a virtual band before dropping back down to the virtual state and emitting a photon with the respectively same, less, and more energy than the absorbed photon. (b) A simplified Raman measurement system. Monochromatic light is directed onto a sample then the emitted light is separated out using a grating before being measured using a CCD camera. Polarizers included in some measurements are shown as well. (c) Data from a  $\text{WS}_2$  film taken at room temperature showing two distinctive peaks using a Horiba LabRam HR Evolution microscope. These peaks are typically found around 360 nm ( $\text{E}_{\text{g}2}^1$ ) and 420 nm ( $\text{A}_{1\text{g}}$ ) [91].

the vibration modes of the material, similar to what is shown in figure 3.7c. By looking for specific peak frequencies for a given material it is possible to identify or narrow down the possible polymorphs of a 2D crystal [89, 90]. This provides a quick, nondestructive method to distinguish materials and properties of a material, similar to SHG. Raman spectroscopy can also use relative intensity of different peaks to distinguish the number of layers of a van der Waals material [88, 92] as well as identify defects within the crystal structure when mapping over the surface [93, 94]. All Raman measurements discussed here were done using a Renishaw inVia Raman or Horiba LabRam HR Evolution microscope. Software was used to remove the substrate signal from the background and can fit the peaks to find the wavelength shift for each maximum.

Raman spectroscopy can be used to look for signs of ferroelectricity or transition to a ferroelectric state. This is often done by monitoring for Raman modes appear (disappear) corresponding to the structural transition to a ferroelectric (paraelectric) state while changing temperature [31, 95], pressure [96], or other mechanisms. Raman spectroscopy can also be enhanced to use polarized measurements by including rotatable

linear polarizers on the excitation and emitted photon beams [97]. This can give additional information about the orientation of the crystal [97, 98], separate signal from different modes [97, 99, 100], and show atomic displacements [101].

## 3.4 Device manufacture

### 3.4.1 Photolithography

Photolithography is a common technique used by industry and academia alike, used to pattern electronics at sizes far below what can be easily done with mechanical manipulations. In most variants of photolithography, a series of photosensitive polymers, or resists, are spread over a surface then exposing the polymer to light to change the chemical makeup of the polymer. This can be done by spinning a solution of the desired polymer, made with a compatible solvent, at high speeds over a substrate. The solution is dripped on the substrate either statically or dynamically under a slower rotation. The substrate is then rotated at high speeds until the desired thickness of polymer is left on the surface, the excess being spun off the substrate edges. The solvent is partially removed by baking the substrate and polymer for a short time so the resist reaches a consistent durability. The resist is then exposed to light or an electron beam that causes the polymer to react. After exposure the undesired resist is then removed by soaking the substrate in a chemical developer. Developer selection must take into account any chemistry between the developer and working materials as some developers can react with the exposed material. For negative resists, exposed regions of polymer are removed when developed, positive resists will only have non-exposed regions removed. For devices that change based on the flake, the resist pattern is generated on a computer and then written by a moving laser to fit the device dimensions. In commonly used patterns, a mask of chrome on quartz is prefabricated. The mask is moved over the flake then the entire surface is flooded with light at once, exposing the regions with the desired resist pattern. We typically choose a multiple layer resist stack as allowing the bottom layer dissolve long enough to undercut the top allows for easier liftoff when removing evaporated metals (See 3.4.3). Resist can also be used to protect part of a sample when etching allowing a patterned etch of the substrate or testing device.

### 3.4.1.1 LOR/SPR stack

The LOR/SPR negative resist stack is easy to use and allows for high resolution patterns down to  $2\mu m$ . Before any resist is added the substrate is given a dehydration bake of  $115C$  for  $60s$  to remove any water. A layer of LOR-2A is statically deposited as the first layer of the stack. The substrate is then spun at  $4000RPM$  for  $45s$  reducing the LOR-2A to a  $\sim 200nm$  thick coating. [102] Finally we bake it at  $180C$  for  $60s$  on a hot plate to remove some solvent. Next a layer of SPR-3012 is dynamically dispensed at  $900RPM$ . The substrate is then sped up and spun again at  $4000RPM$  for  $45s$  flattening the SPR-3012 to  $\sim 1.3\mu m$  thick. [103] This is then baked for  $95C$  for  $60s$  on a hot plate. The resist stack and flake is then exposed using a MA/BA Gen4 or Gen2 Contact Aligner (SUSS MicroTec) with  $54mW$  of light. The patterned resist is then developed for  $60s$  in Microposit CD-26 (Tetramethylammonium hydroxide 1-5% and water, Shipley).

Table 3.1: Lithography resists

Resist	Soft bake	Developer	Liftoff
LOR-2A	$180C$ for $60s$	CD-26	Remover-PG
SPR-3012	$95C$ for $60s$	CD-26	Remover-PG
PMMA	$180C$ for $180s$	MIBK	Acetone/Remover-PG
SF6-slow	$200C$ for $60s$	101A	Remover-PG

The resist polymer, chemical developers, and liftoff solvents used in the photo and e-beam lithography processes.

### 3.4.1.2 PMMA/PMGI/SPR stack for alkali-sensitive materials

Some chalcogenides react with alkali developers such as CD-26 [104] so we developed an alternate photolithography resist stack with a solvent used to develop the layer closest to the material. First a layer of Polymethyl methacrylate (PMMA-2A) (Microchem) is statically deposited, spun at  $2500RPM$  for  $45s$  to give a  $\sim 600nm$  layer, then baked at  $180C$  for  $180s$ . [105] Next a layer of PMGI SF6-slow is dynamically spun at  $900RPM$ , then  $4000RPM$  for  $45s$  to reduce the thickness to  $\sim 300nm$ , and baked at  $180C$  for  $60s$ . [106] Finally, a top-coat of SPR-3012 is dynamically dispensed at  $900RPM$ . This is then spun at  $4000RPM$  for  $45s$  for a thickness  $\sim 1.3\mu m$  and baked for  $95C$  for  $60s$ . The SPR-3012 is then exposed using a MA/BA Contact aligner with  $54mW$  of light (peak  $365nm$ ), developed for  $60s$  in in Microposit CD-26 from Shipley (3.4.1.1), then rinsed

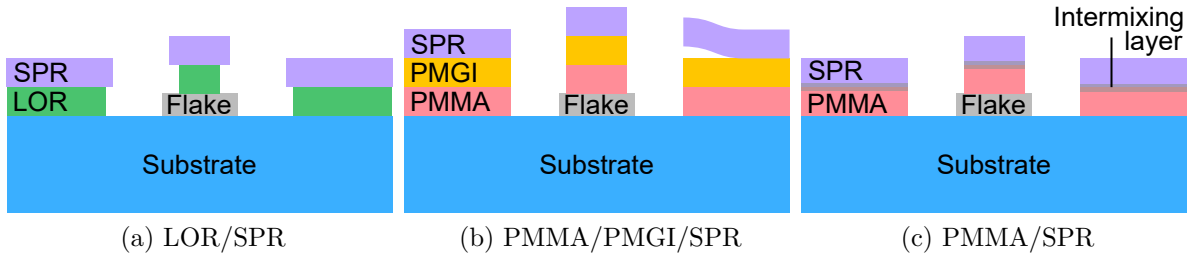


Figure 3.8: Photoresist stacks

Three of the resist stacks used in device manufacture. (a) LOR/SPR used in most of our devices, (b) PMMA/PMGI/SPR used in devices with alkali-sensitive materials, (c) PMMA/SPR alternative stack used initially in some of our alkali-sensitive materials before the (b) stack was developed.

in water. The PMMA and SF6 under-layers are exposed for 30 minutes in a Deep UV (peak 270nm, OAI Deep UV Flood Exposure) at 5.3mW (~9.5 J). The SF6 is developed in 101A developer (Microchem) for 90s then rinsed in water. Finally the PMMA is developed for 10 minutes in methyl isobutyl ketone (MIBK) and a trace amount of water. The substrate is moved though the water for 5 – 10s then to the MIBK, where a thin bubble of water continues to adhere to the resist near the exposed region. After allowing the water to sit on the sample for another 10 – 30s, the substrate is gently shaken back and forth with tweeters to dislodge the SPR layer from the top of the sample. This prevents the SPR from later partially peeling up then adhering to the substrate, ruining the lithography pattern. The sample is left in the MIBK for another 5 – 10m to develop the PMMA down to the substrate. The MIBK is then removed with 2-propanol.

An alternate version of this process used a thicker PMMA (6A) with SPR-3012 on top. Because the SPR uses a PMMA-compatible solvent (Cyclopentanone) the two layers would intermix and form a layer that was unable to be dissolved in either developer. This was removed by ashing the layer for 515 seconds in the M4L with 250 sccm oxygen, 50 sccm helium, 500mTorr pressure, 450W power. This process varied greatly depending on polymer uniformity and location of device on the substrate so later devices included the PMGI/SF6 layer to eliminate the inconsistency.

### **3.4.2 Thin filament shadow mask**

As an alternative to lithography, we used an all-dry quartz filament shadow mask for metal evaporation (3.4.3). This allowed us to test contact resistance of an underlying material without introducing the polymers, chemicals, and processing to the material that may damage the surface or leave a residue between the material and metal contacts. We heated two quartz rod ends with an acetylene torch until semi-molten. We then lightly touched the two ends together and quickly pulled the ends apart within the flame. If done correctly, this produced several  $2 - 10\text{cm}$  long strands of quartz that were  $< 2\mu\text{m}$  in diameter. These were identified under a florescent light by their thread-like behavior, losing most stiffness and free to float in the air when  $\lesssim 2\mu\text{m}$  in diameter. These filaments were then caught on glass forks by dragging the filament across the opening and snapping the end attached to the quartz rod. The forks were cut to fit over the sides of our sample chip substrates and reinforced with metal for durability. The sample chip was attached to a glass slide with double-sided tape. These filaments were then draped over the sample material with the glass fork. The ends of the filament were then cut with a tungsten needle and the glass fork removed. The filament could be adjusted by pulling it gently with a thin copper wire until it was in place and laying flat against the surface. This often caused the quartz to snap so the range of movement was limited to within a few 10s of microns from where it started. Once the filament was maneuvered it was fixed in place by wrapping the ends in Teflon tape that wrapped around the glass slide. Teflon tape was chosen as it is unlikely to scratch the material and has no adhesive that would cause the filament to move when securing it. The tape was also used to reduce the exposed area so only a small region around the material was included and reduce the risk of a short between the two sides. We found a filament less than  $.5\mu$  tended to cause a short between the two sides while greater than  $3\mu\text{m}$  would not sit flush against the surface. Metal choice is similarly important as certain metals like indium tended to “wet” across the surface and short at any diameter.

### **3.4.3 Metal evaporation and liftoff**

Metal deposition was done using the Lab-18 Thin Film Deposition System (Kurt J. Lesker Co.). This was used to add contacts to a lithography-patterned flake by covering a substrate with layers of metal. We used electron beam evaporated titanium and gold for the uniform deposition and high conductivity. First  $\sim 5\text{nm}$  of titanium was deposited at  $\sim 1\text{\AA/s}$  as titanium adheres well to  $\text{SiO}_2$ . Next a layer of  $35 - 50\text{nm}$  of gold was

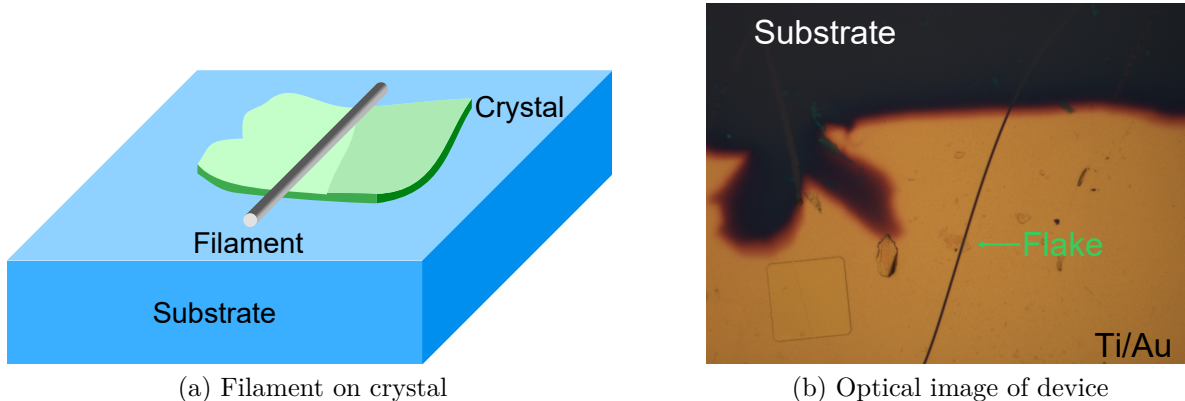


Figure 3.9: Filament device

(a) Filament shadow mask and (b) flake filament device made to test dry contact process.

evaporated at  $\sim 1\text{\AA/s}$  on top of the titanium. The gold provided a highly conductive protective layer that was inert in atmosphere and safe to use when wiring samples.

The Lab-18 Thin Film Deposition System also had an in situ ion source that could be used to clean and roughen the surface of a material before deposition occurred. A typical process used 10sccm of argon gas flowed over a metal coil with 2.5A of emission current and 150V between the coil and the substrate. The ion source is undirected which caused trace amounts of iron from the chamber itself to be knocked loose and deposited on the surface of the sample.

To remove excess metals from the substrate the lithography resist was then removed through a 'lift-off' process. The resist stacks were designed to have a small undercut between the top and bottom layer to allow solvents to dissolve the resists from the edges even if metal had deposited on the sides of the upper layers. For LOR-based (see 3.4.1.1) stacks the substrate was soaked in heated Remover-PG (Microchem) for 10 minutes at 60C. The Remover-PG was then gently blown with a pipette over the surface of the substrate to push away any metals that were no longer adhered to resist. This process was repeated until all of the resist and metal adhered to it were removed. As smaller features had less surface area of resist for the solvent to resolve, more forceful streams were sometimes needed. If this was not enough to peel off the resist, sonication in a water bath was sometimes used. This often pulled off the metals deposited on the substrate, flake, or even the flake itself, so was used only when necessary. The Remover-PG was then removed by soaking the material in 2-propanol for 5 minutes and blow-dried with a nitrogen gun. For PMMA based stacked unheated acetone was used in the place of

Remover-PG while the rest of the process was the same.

### 3.4.4 Sample wiring

Sample flake and film crystals were typically a few tens of microns across while wires used in any electronics are far larger. Our wiring process allowed for us to make connections first to a sample mount with fixed wiring attachments, the mount could then be attached to larger devices without removing the wires from the sample or risk damaging the materials. Lithography wiring patterns were designed with .5 – 1mm, per side, square pads that connected by metal leads running along the substrate to the sample material. To connect the pads to a preexisting wiring system we used a series of indium dots and thin gold wires (99.95% Au, 25 $\mu$ m, Alfa Aesar). We first adhered the gold wire to the wiring structure with lead-free solder, this avoided any currents from the soldering iron from damaging the sample. Next we placed an indium dot (TODO source) on each of the sample wiring pads using modified tweezers. The tweezers were cut down to a single prong, then the tip cut flat at a 45 degree angle and further sanded smooth using the side of a razor blade. This allowed the indium dot to adhere to the tip easily. The modified tweezers can be held similar to a pen for increased dexterity and use with samples in recessed mounts, and greatly increase ease of wiring and speed. The gold wire was then bent down and pressed into the indium dot on the wiring pad, so the dot was only slightly flattened and the wire remained fastened. A second indium dot was pressed into the first, forming a sandwich-like structure, that held the gold wire firmly in place. The excess gold wire was then bent away from the sample along the original wire to prevent it from coming into contact with any part of the sample or other wires. This process was repeated for each of the wiring pads on the device. Figure 3.10a shows a sample wired to a PPMS puck using this method.

To prevent static discharge from damaging the material devices several measures were taken. A ionizing fan (Chapman VSE3000 static eliminator) was constantly blown across the sample and wiring station at all times to discharge any static build up. The person wiring was grounded with a static wrist strap to the building ground at all times when touching the device. The modified tweezers were held without gloves to connect it to the building ground through the body. The wiring station used a rubber floor mat with metal stool to isolate the person from the floor and prevent any charge buildup from the ground. Finally, clothing was chosen to reduce the buildup of static, especially in winter as the dryer air made hazardous amounts of static buildup fairly frequent. [15] Figure 3.10b shows the setup typically used to prevent static discharge into the sample.

### 3.4.5 Layer Transfer (TODO: review)

Layer Transfer a method to create complex heterostructures of 2D materials, typically flakes, by vertically stacking multiple materials. Stacked heterostructures can take advantage of the distinct properties of each material without the lower layers altering the growth of subsequent compounds. We began by making thin stamps of PDMS (polydimethylsiloxane), a clear resin that is commonly used for layer transfers. The PDMS stamps are formed using a mix of Sylgard 184 Silicone Elastomer and curing agent in a 12:1 ratio in a flat plastic or petri dish to form a 1mm thin film. The mix is stirred for 3 minutes, sonicated for 4 minutes on low power to remove most bubbles, and any remaining bubbles in the mixture popped by hand using a thin needle or rod. The PDMS is then left to cure for about 12 hours, covered to avoid any particle contamination. The resulting film can be diced to any desired size, and applied to glass slides or other flat platforms to work with. Care must be taken to use a dish with a very flat bottom and it is allowed to cure levelly or the surface of film will move out of microscope focus under horizontal translation.

We started by exfoliating flakes of crystal directly on to PDMS stamps and identifying the flakes under the optical microscope, similar to what would be done on a typical substrate. This has the advantage of using the fewest steps and compounds to do the transfer [107] with the trade-off that flakes less than 10 nm are hard to identify on the clear resin. Once the desired flake on PDMS is identified it can be transferred to the desired substrate. The glass slide is affixed to a mount with the PDMS stamp facing down, with the mount connected to a manual micro precision linear stage capable in moving in any direction, figure 3.11. The target substrate is placed on a heating block directly under the stamp and affixed with tape to prevent it adhering to stamp. The flake and target are separately moved to the center of the field of view then aligned with each other. This was typically done by drawing the outline of the substrate on monitor with marker and moving the flake to match. The stamp is then lowered into contact with the substrate, taking into account any lateral stamp-to-substrate shifting from the contact. Once the flake is in contact with the desired part of the substrate the underlying heating is set to 80 C, softening the PDMS. While heated, the flake-substrate van der Waals bond should be stronger than the PDMS-flake bond, so the slide can be removed while the flake adheres to the target. We also used an alternative metal slide with an optical window cut into the center for the PDMS to hang from if the stamp was not flat. The center of the stamp hung below the edges so the flake would always be able to make contact, but the flake was more wont to shift horizontally and force realignment while

making contact.

## 3.5 Device characterization

### 3.5.1 Electronic measurement systems (TODO: review)

The electronic measurements of most devices were done using a series of Keithley instruments and a cryostat networked to a computer. Each instrument was networked through a series of GPIB (IEEE 488) cables to a computer for control. GPIB is an older protocol and port for connecting and working with instruments, but was chosen as it worked with all electronics and cryostats used in the lab. It allows for daisy chaining of multiple instruments together where the analog signal is amplified and passed along cables. The protocol is not fault tolerant so care must be taken to ensure instruments do not lock up the entire setup and communication timeouts were set appropriately to deal with instrument reliability while still providing a large enough window for data to be taken.

For semiconductor measurements a Keithley 6430 was typically used to provide the DC source bias, as it had the largest voltage range and impedance option of the available electronic instruments. The 6430 also worked with triax cabling to reduce parasitic capacitance and external EM fields. It also measured current or voltage for the respective voltage and current feedback loops that could be recorded for two-point data. A Keithley 2400 was used to provide gating bias as it works similar to the 6430 but with less range and unshielded cabling. A Keithley 2182 current source was used for sourcing current with any metallic samples. Finally two Keithley 2182A nano-voltmeters were used in conjunction with the other instruments for measuring additional voltages between leads. Figure 3.12 shows the electronics setup used in material measurements.

All instruments were controlled and monitored from a single LabView program Project Unity, see B. While LabView is a terrible language for writing a large program in it was chosen because it integrated well with past code and current lab equipment. Project Unity contains a series of launchers that contained easy to change configurations for most measurements. The launcher would then pass the configuration parameters to a separate thread to process. This allowed multiple measurements to be queued, and for subsequent tasks and edited before being run. All measurement parameters were saved in the beginning of each data file in INI format to preserve as much of the state with the data, all data was saved in CSV format. The main thread was responsible for initial

configuration of all tools, setting up measurement environments, sending commands and recording instrument data, as well as monitoring overall progress and instrument status. A separate thread was responsible for graphing and fitting live data so it did not impact the run time of the main thread.

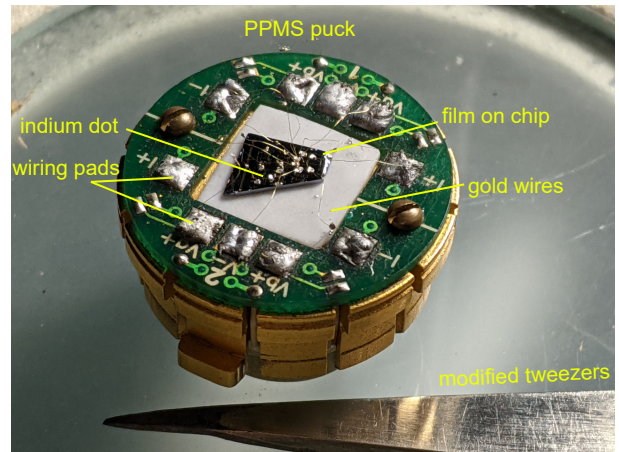
### 3.5.2 PPMS (TODO: review)

Most of the manufactured devices mentioned in this text were measured in a Physical Property Measurement System (PPMS) from quantum design as it provides an ideal measurement environment platform. The PPMS uses sample wiring puck, figure 3.10a, that can be exchanged while the system is filled with liquid helium without stopping and drying the system out. The puck fits into an inner chamber with wiring pins. The pins are connected to an external port with six pairs of twisted wire, then from the port to a BNC breakout box via a single shielded cable with twisted pairs of all wires. This allowed us to change connections to different Keithley or other electronics without removing the sample from the chamber. While filled with helium the chamber could reach pressures near 0.1 mTorr [108] with the Cryopump High-Vacuum Option (Quantum Design). The PPMS has a temperature range of 1.7 to 400 K with the ability to cool a puck from room to base temperature in a few hours. Our PPMS was equipped with a 9 T magnet, with field errors around .002 T at low magnetic fields [108], allowing us to do hall and magnetoresistance measurements.

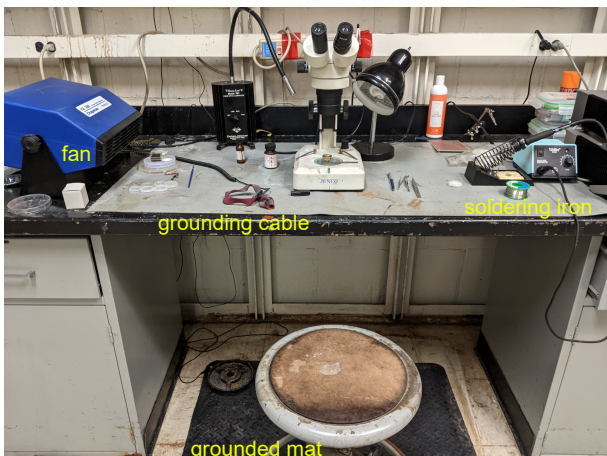
The PPMS cryostat was run using a Model 6000 (Quantum Design) computer and gas handling system, figure 3.12. The Model 6000 controlled helium circulation and chamber temperature though an integrated series of electronic valves and an external rotary vane pump (Alcatel 2010SD). Because helium is a finite resource, all helium gas was sent to be recovered though an external helium recovery system. All of the the Model 6000 computer system and options were connected to the electronics control desktop computer via GPIB, except the magnet which used a separate USB-connected controller. This allowed the PPMS to be run both at the Model 6000 interface and with the desktop program MultiVu (Quantum Design). A .net SDK with LabView interface provided a way to integrate the PPMS temperature and magnetic field control into Project Unity.

### 3.5.3 Hall probe (TODO)

algorithm?



(a) PPMS puck with wired sample and tweezers



(b) Wiring station

Figure 3.10: Sample wiring

(a) A PPMS puck with substrate chip, etched film, and evaporated wiring pads. The wiring pads are connected to the PPMS puck using indium dots and gold wires. The modified tweezers are also shown. (b) The larger wiring station setup to prevent static discharge into the sample. A ionizing fan blows air across the sample while wiring to prevent static buildup. The person wiring is isolated from the floor and table using grounded mats. They are also connected to the same ground using an additional cable and conductive strap that ties around an arm. The soldering iron is used to attach gold wires to the sample mount.

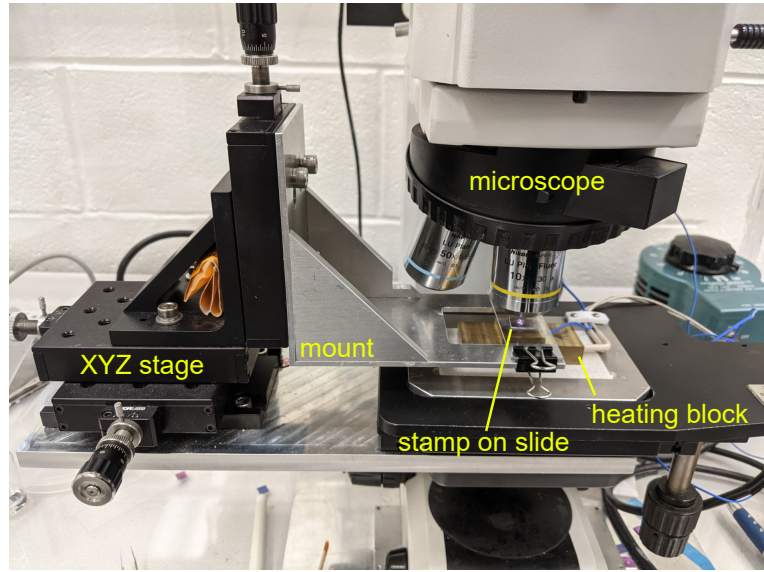


Figure 3.11: Layer transfer station setup

Our setup to transfer flakes on to substrates with an accuracy of a few microns. (left) XYZ stage with attached transfer mount, (top) Eclipse LV150 microscope (Nikon), and (center) PDMS stamp on glass slide over substrate on heating block.

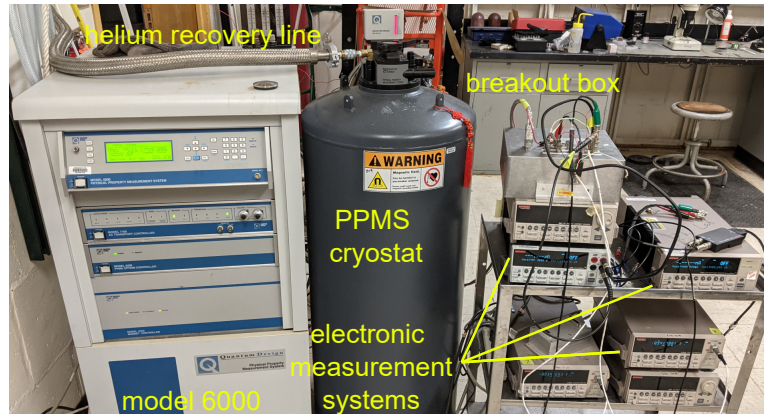


Figure 3.12: PPMS and electronics measurement system

Our PPMS measurement systems attached electronics used in material measurements. (left) Model 6000 PPMS computer and gas handling system. (middle) PPMS cryostat with High-Vacuum Option. (right) Electronics measurement system connected to PPMS. The breakout box and electronics are set up for a typical four-point resistance or hall measurement with gating.

# **Chapter 4 |**

# **Electric field induced metallic behavior in thin crystals of ferroelectric $\alpha$ -In<sub>2</sub>Se<sub>3</sub>**

## **4.1 Introduction**

Ferroelectric field effect transistors (FeFETs, see 2.2.4) are a natural evolution to field effect transistors (FET), providing a means of maintaining the transistor state without the need for a constant gate voltage. Typically this is achieved as a standard FET with a ferroelectric replacing gate dielectric. [109, 110] Further engineering for use in devices like ferroelectric random access memory add a metal layer in between the ferroelectric and channel to enhance the field, and adapt the FinFET design to utilize this design. [111] FeFET commercialization, in FRAM and beyond, still faces many engineering challenges including retention duration, finding an optimal coercive field and polarization strength, leakage current through the ferroelectric dielectric, material interface mismatches, limits to minimization of the ferroelectric. [111, 112] With the discovery of conductive ferroelectric compounds, see 2.2.6, we can construct a new variation of the FeFET, where the ferroelectric acts the role of the semiconductor device channel. [113] Ferroelectric semiconductor field effect transistors (FeSmFETs) opens up many new possibilities for future devices and may one day answer the aforementioned obstacles.

In 2017  $\alpha$ (3R)- and  $\beta$ -In<sub>2</sub>Se<sub>3</sub> were first predicted to be ferroelectric down to one unit cell. [114] The  $\alpha$ -phase prediction indicated a combined binary in-plane (IP) and out-of-plane (OOP) polarization as the selenium atom shifted in the lattice, while

the  $\beta$ -phase showed only binary IP polarization. Due to the conductive nature of polar metals it is difficult to perform traditional capacitance-polarization methods on a crystal as much of the capacitance voltage simply leaks through the material. In lieu of those measurements many distinct experiments form a pool of evidence for the existence of ferroelectricity in  $\alpha\text{-In}_2\text{Se}_3$ . Second harmonic generation (SHG) shows a breaking of inversion symmetry [115–117], a necessary requirement for ferroelectricity. Piezoelectric force microscopy (PFM) has also shown evidence supporting ferroelectricity [78, 115, 118–120], though PFM can often give false positives as similar responses arise from other phenomena. [75] To counter this some authors have looked at both IP and OOP PFM response correlation [44, 78, 115, 116, 119, 120], as well as observing the effect IP electric fields to alter the OOP polarization measured by PFM [119], narrowing the possibilities of what may be producing false positives.

The largest experimental verification of ferroelectricity in  $\alpha\text{-In}_2\text{Se}_3$  comes from several disparate devices designs that show signs of polarization. The most explicit example was from an  $\alpha\text{-In}_2\text{Se}_3$ /graphene heterostructure FET. The graphene channel fermi-level shifts from the electric field produced by the FET gate and the  $\alpha\text{-In}_2\text{Se}_3$  polarization, forming two peaks in the channel resistance as gate voltage is swept and the fermi-level passes through the charge neutral point. [121] The authors use this to estimate a polarization value of  $0.92 \mu\text{C}/\text{cm}^2$ , similar to the original theoretical prediction of  $0.6 \mu\text{C}/\text{cm}^2$  [114]. Extensive work has been carried out by multiple group using  $\alpha\text{-In}_2\text{Se}_3$  to create IP [78, 115, 120] and OOP [118, 122] rectifying devices. For  $V_{DS}$  sweeps below the coercive field threshold, the devices act as a typical semiconductor channel. Above the threshold voltage the device current shows a significant change in slope, and a large hysteresis between increasing and decreasing voltage sweeps, see figure 4.3c and f. Finally, the recent pioneering of the first FeSmFET using thin crystals of  $\alpha\text{-In}_2\text{Se}_3$  with gate dielectric of 90-nm-thick  $\text{SiO}_2$  or 15-nm-thick  $\text{HfO}_2$ . When gated, the channel current showed a large hysteresis, forming clockwise and counterclockwise loops with the respective gate dielectric, and persisting down to liquid helium temperatures. [113] Below we discuss the manufacture and measurement of similar  $\alpha\text{-In}_2\text{Se}_3$  FeSmFET devices that show a metallic transition when gated through a  $\text{SiO}_2$  dialectic.

## 4.2 Device manufacture

Thin crystals of  $\alpha\text{-In}_2\text{Se}_3$  were grown by a modified Bridgman method. Transport measurements were carried out on both bulk and thin mechanically-exfoliated crystals.

Sample	$t$ (nm)	$L_{volt}$ ( $\mu m$ )	$L_{current}$ ( $\mu m$ )	$w$ ( $\mu m$ )	Device pattern
A	20	2	12	5	four-point probe
B	13	4	16	30	four-point probe
C	110	5	15	10	Hall bar
D	110	2	12	9	Hall bar

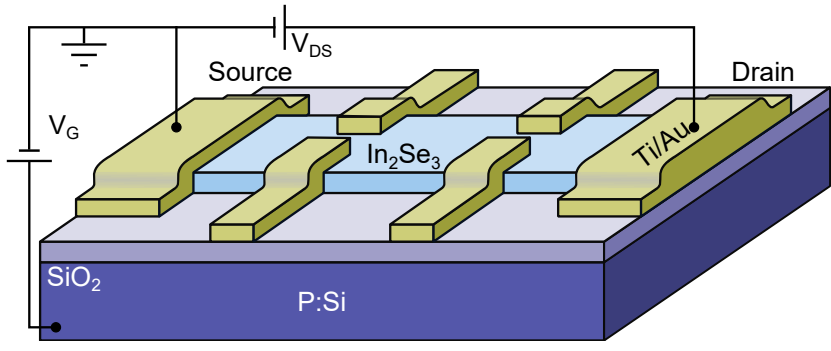
Table 4.1: Device parameters

Physical dimensions of the  $\alpha$ -In<sub>2</sub>Se<sub>3</sub> crystals used in the sample devices and the lead configuration.  $L_{volt}$  and  $L_{current}$  are the distance between the respective voltage and current leads,  $w$  the channel width of the crystal, and  $t$  the thickness of the crystal.

For bulk resistivity measurements, silver paint was used to form conductive terminals. In-plane resistivity measurements were carried out using a hall bar pattern along the longest axis of the bulk crystal. For out-of-plane measurements, to ensure a fresh surface, the previous leads were removed with a razor before new leads were added on. A modified four-point pattern was used to accommodate the thin c-axis of the crystal: a current lead was placed in the center of the crystal on the opposing sides of the c-axis with a voltage lead encircling each current lead.

Flakes of thin crystals of  $\alpha$ -In<sub>2</sub>Se<sub>3</sub> on Si:P/SiO<sub>2</sub> were manufactured using mechanical exfoliation as described in 3.2.2. Flakes were identified using an optical microscope and atomic force microscopy was used to establish a rough microscope color code to judge the thickness of the flakes. Below 20nm, flakes hue was unchanged but appeared increasingly transparent as thickness decreased. To promote better van der Walls adhesion of the flake to the substrate, the latter was first cleaned in Nanostrip, Acetone, 2-Propanol, and DI-water, before flake exfoliation, and the substrate was heated to 100C while in contact with the tape prior to the final removal. After optical identification, flake-substrates were kept in a drybox, or later in vacuum, to avoid water contamination and oxidation.

Flakes of crystal were made into four-point probe and Hall bar FET devices using photolithography and e-beam metal deposition. Similar to many other van der Waals chalcogenide materials, In<sub>2</sub>Se<sub>3</sub> is sensitive to the alkali (base) developers used in many photodevelopment processes. [123, 124] Initial Hall bar devices with thinner crystal flakes were completely inoperative after manufacture, while thicker devices showed substantial Schottky barriers on various contacts. Milling away crystal material between the lithography and metal evaporation produced better contacts, but inconsistently, and only worked with thicker devices. To circumvent this effect, we modified our lithography step to only allow solvent developers in contact with the flake material, with the procedure



(a) Hall bar schematic

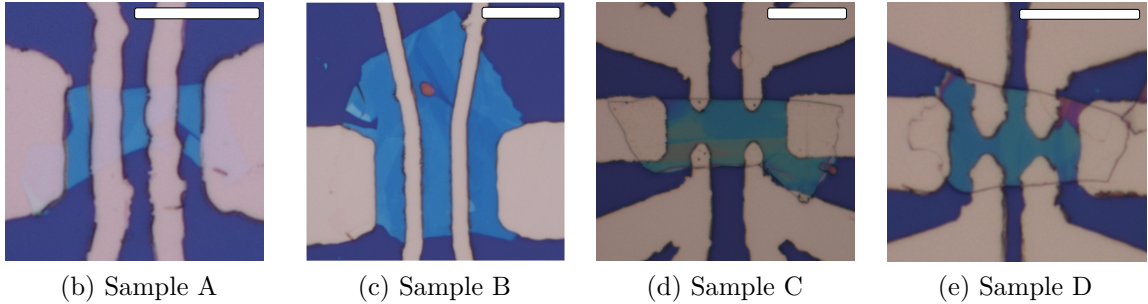


Figure 4.1: Device images

(a) Schematic of the Hall bar device with used in flake measurements, samples A and B had connected voltage leads for four-point measurements while C and D had separated leads for hall measurements. (b-e) Optical images of sample devices following this design with  $10 \mu\text{m}$  scale bars.

described in section 3.4.1.2. 5 nm of titanium and 45 nm of gold was evaporated using either a Lab-18 Thin Film Deposition System (Kurt J. Lesker Co.) or a Temescale FC2000 (Ferrotec). The excess material was removed using the solvent Remover-PG (Microchem). Figure 4.1 shows the layout and optical images of the devices measured in this chapter, table 4.1 the corresponding parameters of those devices. All measurements were carried out in low vacuum, less than 1 mTorr, in a Model 6000 Physical Properties Measurement System (PPMS, Quantum Design). A Keithley 6340 was used as the current and voltage bias source as well as the corresponding two-point voltage and current measurements, two Keithley 2182A were used for four-point and hall measurements across the voltage leads, and a Keithley 2400 was used to provide the gate voltage bias.

### 4.3 Optical crystal measurements

Indium and selenium can form a variety of compounds, and the growth process is complicated and may result in crystals with mixed polymorphs, see section 2.3.2. [44]

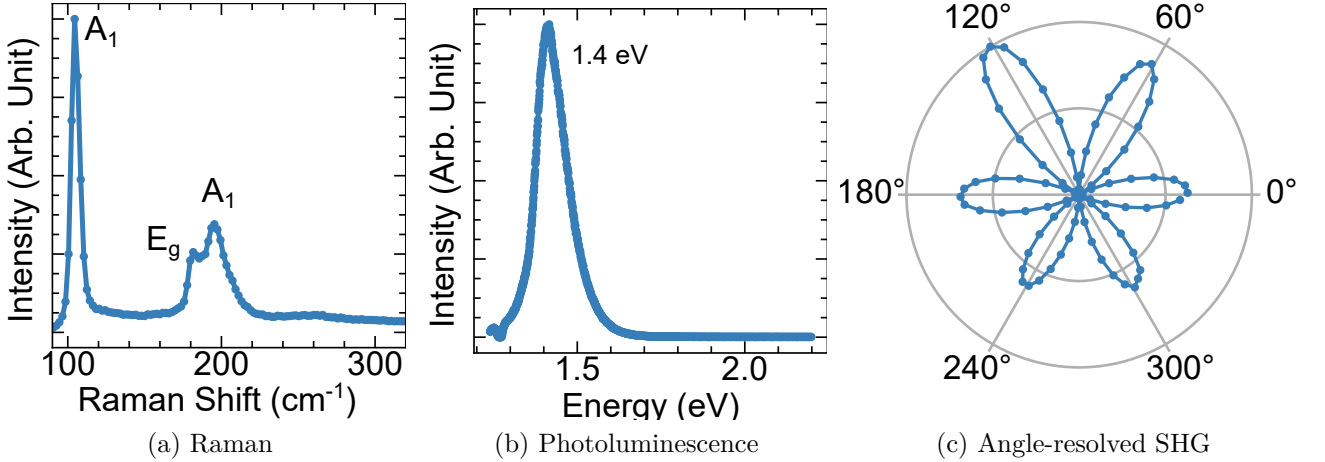


Figure 4.2: Optical measurements of  $\alpha\text{-In}_2\text{Se}_3$ .

Raman (a), photoluminescence (b), and angle-resolved SHG (c) of exfoliated  $\alpha\text{-In}_2\text{Se}_3$  flakes on Si-SiO<sub>2</sub> substrate.

Because of this, several optical measurements were used to confirm the stoichiometry and lattice stacking of the material used in our devices. X-Ray diffraction measurements displayed peaks corresponding to the  $R3m$  or  $R\bar{3}m$  space groups, indicating  $\alpha$ - or  $\beta$ -phase. Raman showed peaks near  $104$ ,  $179$ , and  $193 \text{ cm}^{-1}$  corresponding to the  $A_1^1$ ,  $E^3$ , and  $A_1^4$  peaks of  $\alpha\text{-In}_2\text{Se}_3$ . [44, 125] Photoluminescence showed an energy gap of  $1.4 \text{ eV}$ , consistent with previous  $\alpha\text{-In}_2\text{Se}_3$  optical measurements. [125] Finally, angle-resolved SHG showed a six-fold symmetry establishing the material as stacking in a  $R3m$  (166) space group lattice. [115, 116, 120] Figure 4.2 shows the Raman, photoluminescence, and SHG measurements performed on exfoliated flakes of crystal on Si:P/SiO<sub>2</sub> wafer chips. Raman and photoluminescence measurements were taken using a Renishaw inVia Raman microscope (488 nm laser).

## 4.4 FET measurements

Thin crystals of  $\alpha\text{-In}_2\text{Se}_3$  were manufactured into Hall bar and four-point probe FETs. Devices were made on conductive substrates of doped silicon with an insulating layer of 300nm thermally grown Si:P/SiO<sub>2</sub>, allowing us to use the substrate as the gate in the FETs. Figure 4.3 shows sample A source-drain current  $I_D$  measured against voltage bias  $V_{DS}$  from 0 to 5 V, and separately for 0 to -5 V, for fixed back gate voltages. Gate voltages were fixed in 25 V intervals from -75 V to 75 V for each sequence. The rapid

increase in  $I_D$  at low voltages is indicative of two back-to-back Schottky diodes, see section 2.1.1. Samples B and C showed a similar measurement with both the increasing and decreasing  $V_{DS}$  bias for fixed gate voltages, figures C.2 and C.3. None of the samples measured were seen to saturate within  $\pm 10$  V for any gate bias. The lower  $I_D$  for negative  $V_{DS}$  bias than positive is typical of n-type semiconductors, which is seen in most reports of  $\alpha\text{-In}_2\text{Se}_3$  [126, 127]. Sample A  $V_{DS}$  was cycled from 0 V, 10 V, -10V, to 0 V, forming asymmetric hysteresis in the current. The switching behavior is similar to previous reports of  $\alpha\text{-In}_2\text{Se}_3$  rectifying devices, where the ferroelectric polarization field is thought to modify the Schottky barrier between the material and the metal leads. [78, 115, 118, 122] The increasing drain current with positive gate voltages is indicative of a *n*-type semiconductor [15], consistant with previous measurements on  $\alpha\text{-In}_2\text{Se}_3$  [?, 126].

FET transistor transfer curves, current as a function of gate voltage  $V_G$ , were measured for each device. All measurements shown were performed with a fixed  $V_{DS} = .1V$ , with the  $V_G$  cycled from 0 V, to -75 V, 75 V, -75 V, to 0 V, shown in figure 4.4. For clarity, only the data between -75 V, 75 V, to -75 V is shown, as that behavior is persistent across multiple loops. The measurement was repeated at various, fixed temperatures from 300 K to 2-4 K, the lowest temperature reached is sample dependent due to ice blockages in the PPMS cooling. For each gate voltage sweep sweep the current formed a clockwise hysteresis loop. In all samples the width of the loop decreased with decreasing temperature, though each sample still exhibited a finite hysteresis at the lowest temperature. Samples B and C showed similar clockwise hysteresis behavior, shown in C.4 and C.5. This behavior is consistent with previous work with *n*-type  $\alpha\text{-In}_2\text{Se}_3$  on  $\text{SiO}_2$  FeSmFETs. [113]

## 4.5 Discussion

When cooled from 300 to 2 K, the  $\alpha\text{-In}_2\text{Se}_3$  bulk crystal showed an increase in resistivity emblematic of most semiconductors, seen in figure 4.5a, with variable range hopping conduction appearing below approximately 40 K. In contrast thin gated crystals of  $\alpha\text{-In}_2\text{Se}_3$  showed a more positive  $dR/dT$  slope for increasing positive gate voltages. Figure 4.5b-d show a cross section of the  $I_D(V_G)$  transport measurements taken at different temperatures of samples A, B, and C, shown in figures 4.4, C.4, and C.5.  $V_G = 0$  shows a similar behavior to the bulk crystal, while 50 V and 75 V have a  $dR/dT$  slope indicative of a metallic state. The cross section of  $I_D(V_G)$  is used to examine the metallic transition of the devices as the increased conductivity state was quickly destroyed with changing

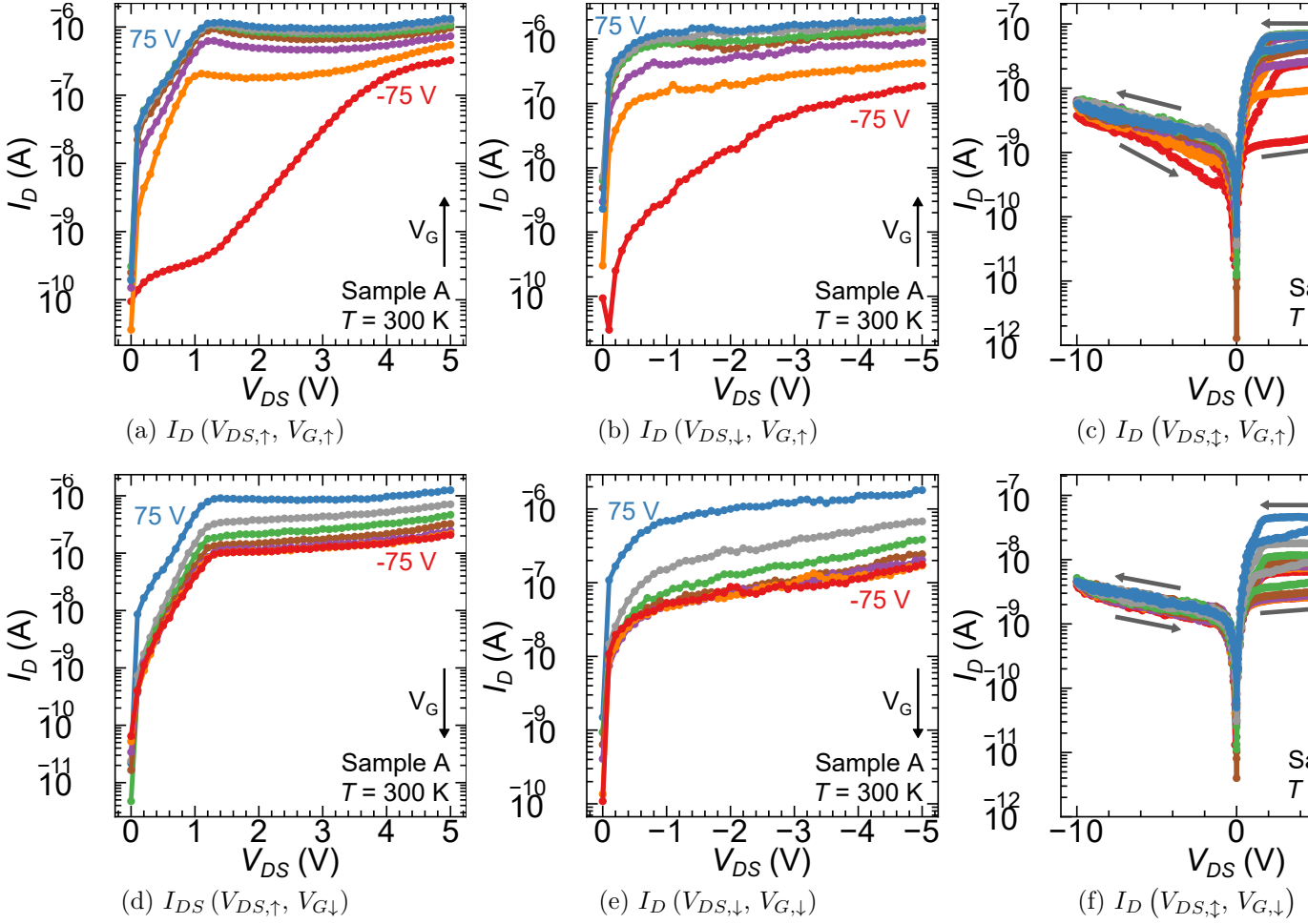


Figure 4.3: Sample A:  $I_D(V_{DS})$

$I_D(V_{DS})$  of sample A with positive-increasing (a & d) and negative-decreasing (b & e)  $V_{DS}$ . (c & f) hysteresis in  $I_D$  as  $V_{DS}$  is cycled from 0 V, 10 V, -10 V, to 0 V. Measurements (a - c) are taken while  $V_G$  is held at 25 V intervals that increase sequentially for each curve, and (d - f) decreasing for  $V_G$  intervals. All measurements were done at 300 K.

temperatures, and was sensitive to the previous state of the system, see figure C.6. In all samples the onset of the uptick in conductivity occurs at higher voltages as temperatures decrease, leading to a shrinking but finite hysteresis loop. These behaviors seem to be independent of ramping rate of  $V_G$  (C.7) and contact resistance does not appear to play a significant role in sample resistance (figures C.6 and C.8).

The magnetoconductance (MC) of sample A displayed weak localization even while gated to the metallic state at 1.8 K (figure 4.6d), as well as 10 and 50 K (figure C.10). The MC data was quantitatively fit to the Hikami-Larkin-Nagaoka theory of 2D weak localization with spin-orbital coupling [128]

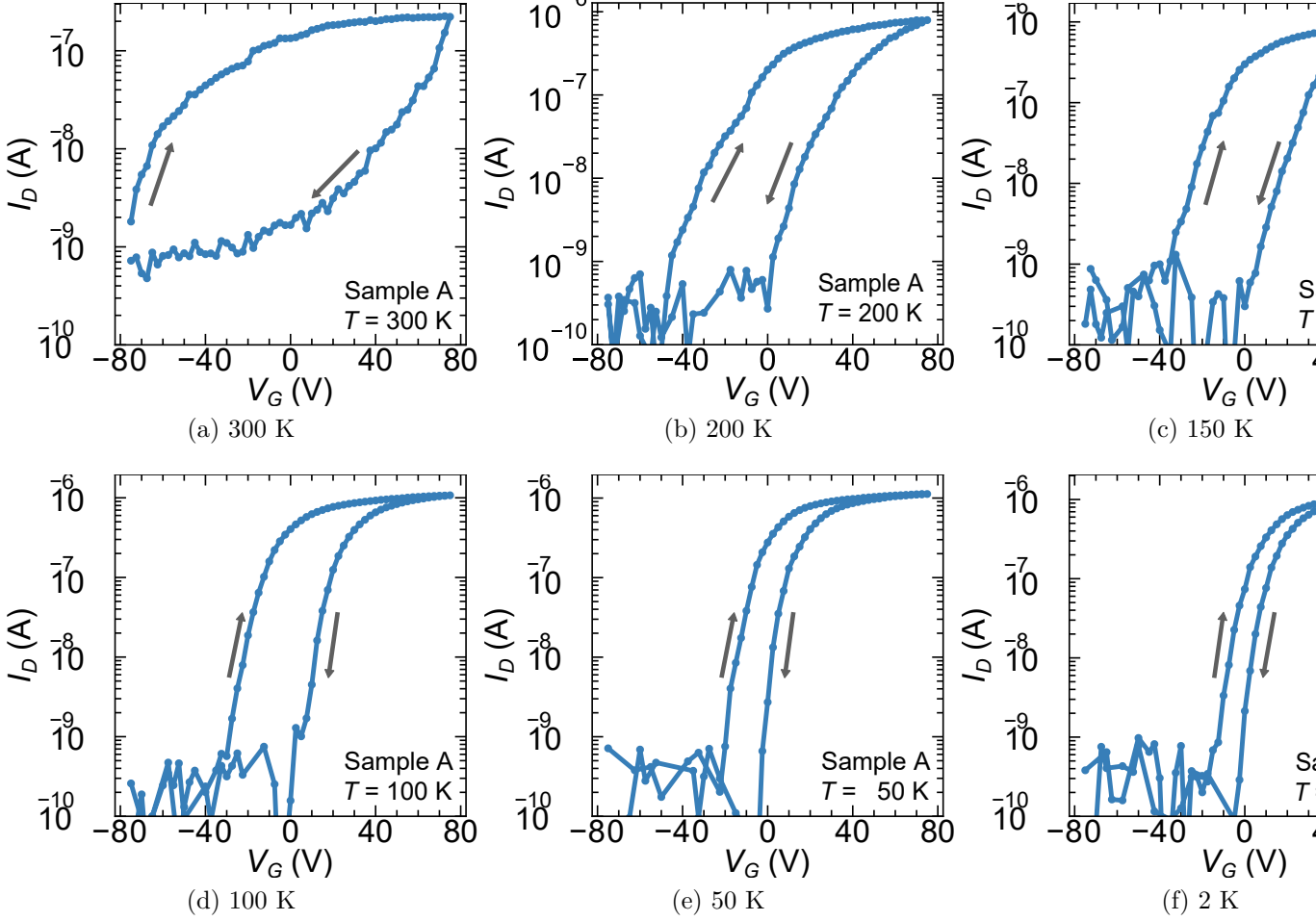


Figure 4.4: Sample A:  $I_D (V_G)$  transfer characteristics  
 $I_D (V_G)$  of sample A at the indicated fixed temperatures. Each was measured with  $V_{DS} = 0.1 V$  as  $V_G$  was cycled, a clockwise hysteresis current loop was seen at all temperatures.

$$\Delta\sigma(B) = \alpha \frac{e^2}{2\pi^2\hbar} \left[ \ln\left(\frac{B_\phi}{B}\right) - \psi\left(\frac{1}{2} + \frac{B_\phi}{B}\right) \right] \quad (4.1)$$

where  $\psi$  is the digamma function,  $B_\phi$  is the dephasing magnetic field,  $\alpha = 1/2$  for weak anti-localization and 1 for weak localization. Sample C shows a small uptick in cross-section resistance near liquid helium temperatures, this is likely a result of disorder in the sample C crystal. Weak localization in a 2D system can manifest a non-metallic, negative  $dR/dT$  at low temperatures. [129]

FIXME: smooth discussion transition

FIXME: Max 2D electric conductivity? No idea where the  $80\sigma_0$  (quantum conduction

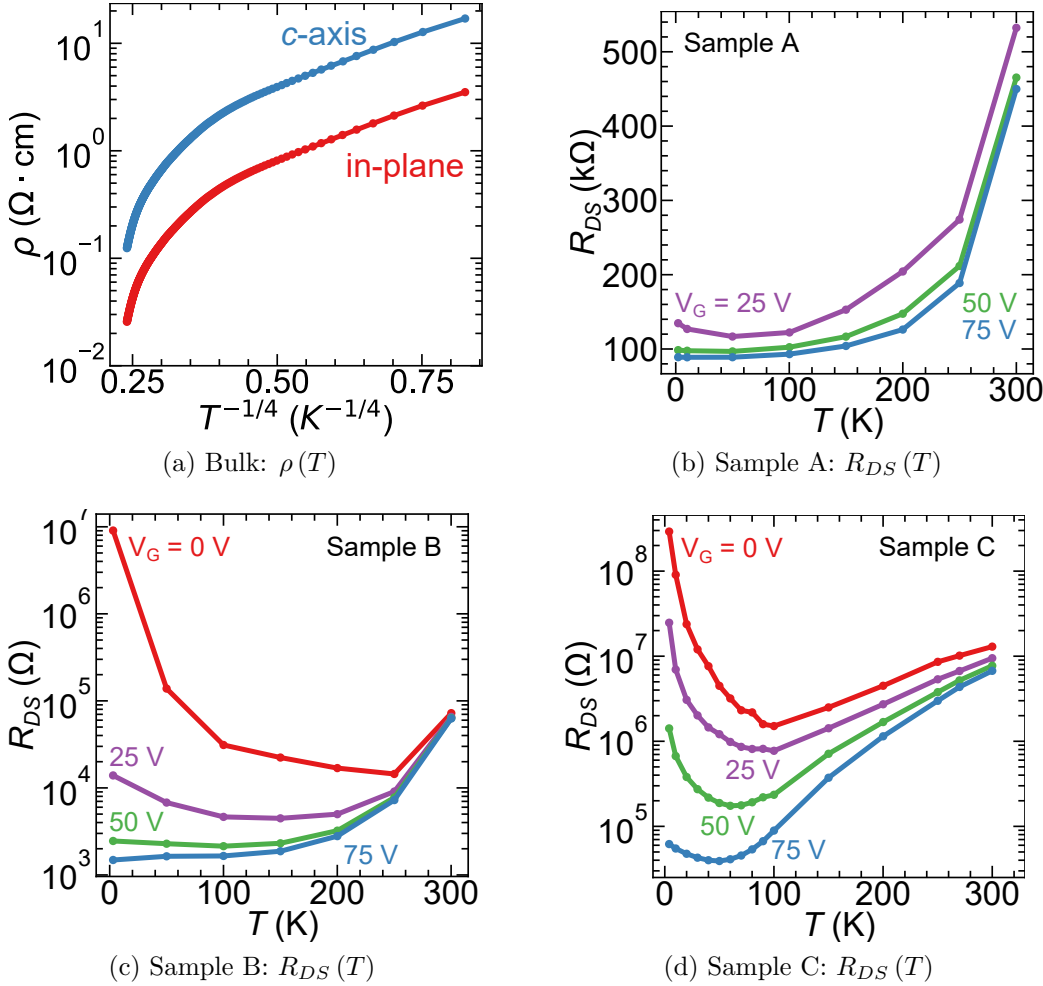


Figure 4.5: Temperature dependence

(a) Bulk crystal resistivity along the *c*-axis and in-plane. (b-d) Temperature cross-section of the  $I_D(V_G)$  transfer characteristics for samples A, B, and C for the curves shown in figures 4.4, C.4, and C.5 respectively. Each data-point is taken from the increasing  $V_G$  (top) portion of the respective  $I_D(V_G)$  curves for 0, 25, 50, and 75 V.

tance) calculation comes from.

FIXME: hysteresis shrink, polarization exists at 2K (invoke 6?)

FIXME: discuss how polarization may change metallic transition

FIXME: Polarization measurement failure in beginning?

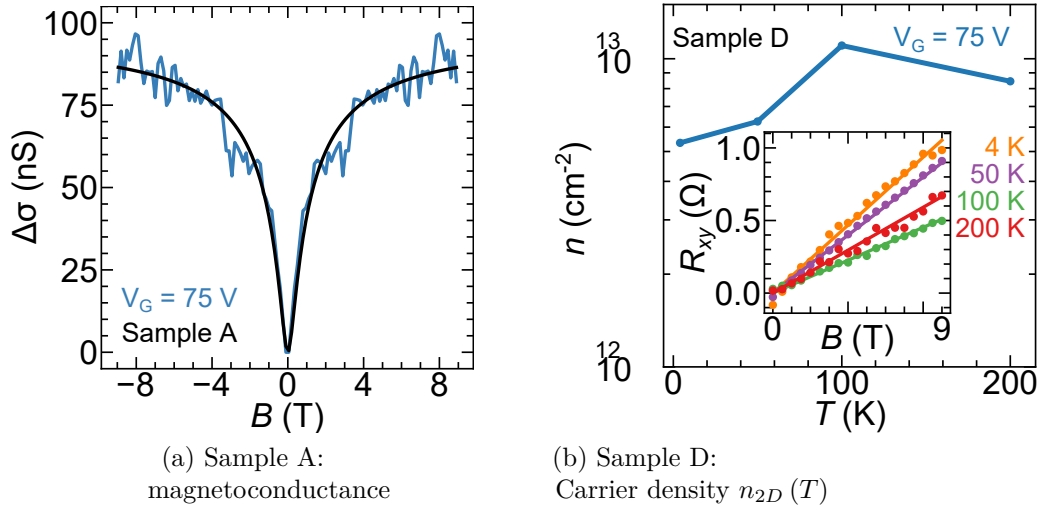


Figure 4.6: Magnetic field measurements

(a) The magnetoconductance of sample A taken at 1.8 K. The data was symmetrized to remove odd-term magnetic field dependence, and normalized to the difference from the measured value at zero-field. (b) Sample D carrier density at various temperatures, the inset shows the hall data used the the carrier density calculations.



# Appendix A |

## 3D crystal symmetry groups

There are a total of 32 possible 3D crystal point groups. The following table lists the groups and are colored according to related phenomena:

- Pyroelectrics, possible ferroelectrics: 1, 2, m, mm2, 3, 3m, 4, 4mm, 6, 6mm
- Piezoelectrics only: 222, 4, 422, 42m, 32, 6, 622, 6m2, 23, 43m
- Non-centrosymmetric and non-piezoelectric: O
- Centrosymmetric:  $\bar{1}$ ,  $2/m$ ,  $mmm$ ,  $4/m$ ,  $4/mmm$ ,  $\bar{3}$ ,  $\bar{3}m$ ,  $6/m$ ,  $6/mmm$ ,  $m3$ ,  $m\bar{3}m$

Table A.1: 3D crystal classes [1]

Crystal system #	Point group			Space groups	
	Hermann– Mauguin		Schoen- flies	Order	
	1	1	$C_1$	1	P1
Triclinic	2	$\bar{1}$	$C_i$	2	$P\bar{1}$
	3–5	2	$C_2$	2	$P2$ , $P2_1$ , $C2$
Monoclinic	6–9	m	$C_s$	2	$Pm$ , $Pc$ , $Cm$ , $Cc$

					$P2/m, P2_1/m,$
10–15	$2/m$	$C_{2h}$	4		$C2/m, P2/c, P2_1/c,$
					$C2/c$
16–24	$222$	$D_2$	4		$P222, P222_1, P2_12_12_1, C222_1,$ $C222, F222, I222, I2_12_12_1$
25–46	$mm2$	$C_{2v}$	4		$Pmm2, Pmc2_1, Pcc2, Pma2, Pca2_1, Pnc2,$ $Pmn2_1, Pba2, Pna2_1, Pnn2,$ $Cmm2, Cmc2_1, Ccc2, Amm2, Aem2,$ $Ama2, Aea2,$
Orthorhombic					
					$Fmm2, Fdd2,$
					$Imm2, Iba2, Im2$
47–74	$mmm$	$D_{2h}$	8		$Pmmm, Pnnn, Pccm, Pban, Pmma, Pnna,$ $Pmna, Pcca, Pbam, Pccn, Pbcm, Pnnm,$ $Pmmn, Pbcn, Pbca, Pnma,$ $Cmcm, Cmce, Cmmm, Cccm, Cmme, Ccce,$ $Fmmm, Fddd,$
					$Immm, Ibam, Ibca, Imma$
75–80	4	$C_4$	4		$P4, P4_1, P4_2, P4_3, I4, I4_1$
81–82	$\bar{4}$	$S_4$	4		$P\bar{4}, I\bar{4}$
83–88	$4/m$	$C_{4h}$	8		$P4/m, P4_2/m, P4/n, P4_2/n,$ $I4/m, I4_1/a$
89–98	$422$	$D_4$	8		$P422, P42_12, P4_122, P4_12_12, P4_222,$ $P4_22_12, P4_322, P4_32_12,$ $I422, I4_122$
Tetragonal					
99–110	$4mm$	$C_{4v}$	8		$P4mm, P4bm, P4cm, P4_2nm, P4cc, P4nc,$ $P4_2mc, P4_2bc,$ $I4mm, I4cm, I4_1md, I4_1cd$

					$P\bar{4}2m, P\bar{4}2c, P\bar{4}2_1m, P\bar{4}2_1c, P\bar{4}m2, P\bar{4}c2,$
111–122	$\bar{4}2m$	$D_{2d}$	8	$P\bar{4}b2, P\bar{4}n2,$	
				$I\bar{4}m2, I\bar{4}c2, I\bar{4}2m, I\bar{4}2d$	
					$P4/mmm, P4/mcc, P4/nbm, P4/nnc,$
					$P4mbm, P4/mnc, P4/nmm, P4/ncc,$
123–142	$4/mmm$	$D_{4h}$	16	$P4_2/mmc, P4_2/mcm, P4_2/nbc, P4_2/nnm,$	
				$P4_2/mbc, P4_2/mnm, P4_2/nmc, PP4_2/ncm,$	
				$I4/mmm, I4/mcm, I4_1/amd, I4_1/acd$	
143–146	3	$C_3$	3	$P3, P3_1, P3_2,$	
				$R3$	
147–148	$\bar{3}$	$S_6$	6	$P\bar{3}, R\bar{3}$	
Trigonal	149–155	32	$D_3$	6	$P312, P321, P3_112, P3_121, P3_212, P3_221,$
				$R32$	
156–161	3m	$C_{3v}$	6	$P3m1, P31m, P3c1, P31c$	
				$R3m, R3c$	
162–167	$\bar{3}m$	$D_{3d}$	12	$P\bar{3}1m, P\bar{3}1c, P\bar{3}m1, P\bar{3}c1,$	
				$R\bar{3}m, R\bar{3}c$	
168–173	6	$C_6$	6	$P6, P6_1, P6_5, P6_2, P6_4, P6_3,$	
174	$\bar{6}$	$C_{3h}$	6	$P\bar{6}$	
175–176	$6/m$	$C_{6h}$	12	$P6/m, P6_3/m$	
Hexagonal	177–182	622	$D_6$	12	$P622, P6_122, P6_522, P6_222, P6_422,$
				$P6_322$	
183–186	6mm	$C_{6v}$	12	$P6mm, P6cc, P6_3cm, P6_3mc$	
187–190	$\bar{6}m2$	$D_{3h}$	12	$P6\bar{m}2, P\bar{6}m2, P\bar{6}2m, P\bar{6}2c$	
191–194	$6/mmm$	$D_{6h}$	24	$P6/mmm, P6/mcc, P6_3/mcm, P6_3/mmc$	

195–199    23 <hr/> 200–206 $m\bar{3}$ <hr/> Cubic      207–214    432	$T$ <hr/> $T_h$ <hr/> $O$	12 <hr/> 24 <hr/> 24	$P23, F23, I23,$ $P2_13, I2_13$ <hr/> $Pm\bar{3}, Pn\bar{3}, Fm\bar{3}, Fd\bar{3}, Im\bar{3}, Pa\bar{3}, Ia\bar{3}$ <hr/> $P432, P4_232,$ $F432, F4_132,$ $I432,$ $P4_332, P4_132, I4_132$ <hr/> $P\bar{4}3m, F\bar{4}3m, I\bar{4}3m,$ $P\bar{4}3n, F\bar{4}3c, I\bar{4}3d$
			$Pm\bar{3}m, Pn\bar{3}n, Pm\bar{3}n, Pn\bar{3}m,$ $Fm\bar{3}m, Fm\bar{3}c, Fd\bar{3}m, Fd\bar{3}c,$ $Im\bar{3}m, Ia\bar{3}d$



# Appendix B | Project Unity control software

## B.1 Running Unity

There are several <Measurement Environment> IV launchers for running typical lab measurements with the same electronics setups. You can select different number/type of measurement by selecting the static (constant) or dynamic current and voltage tabs. Individual settings will show additional information and suggestions when the mouse is hovered over them. There are check boxes to disable any gate voltage, temperature, field, rotator position, and others measurements so the program may be run without any knowledge of those components. Static environment parameters allow you to set the measurement conditions before and after the measurement. Dynamic sequences must be set as they are always run. You can create custom launchers by what dynamic and static environments are handed used. Adding more than one dynamic environment will allow you to do a sweep for each data point in the other environment sweeps creating an ND space map of each parameter. The sweeps are done in order, so at each point in the first environment the second environment sweep runs completely once before the first is changed. This is useful if you want to vary the gate voltage at every temperature to test a FET device quickly or similar setups. Multiple measurement setups can also be queued, so you do not have to wait for each to finish to hit "run." If there are multiple measurements in the queue, not-yet-run measurements can be edited using the "MultiSequence Execution.vi". Once a sequence is started it cannot be edited without aborting and restarting. The overall program progress can be monitored on "Generic ND Data Collection.vi" while the data can be seen on "Generic Plot Window.vi." Individual current and voltage measurements can be monitored by using "Measure V Source I.vi" and "Measure I Source V.vi." As the dilution fridge is more complicated to run the necessary VI to run and monitor it are included in the Dilution Fridge folder.

## B.2 Main Program Structure

Project unity aims to take a generic transport measurement configuration then automatically run that measurement while abstracting away setup. Each launcher contains all the settings for a given run, "Generic ND data collection" runs each measurement sequence, and the data is then plotted in "Generic Plot Window" and written to the data file. All the settings are stored in class files. Classes are used in object-oriented

programming (OOP) to group data with functions that act on that data. One of the big advantages to OOP is the ability to create a sub-class of an already existing class and inherit all its functions. This allows you to create special classes for each task while still retaining all the original functionality. Functions can optionally be overridden in the sub-class so that the sub-class has its own function while the programmer using it will still be able to just call the original function and not have to deal with each new specific variant.

### B.2.1 Static Environments

There are two different sets of classes: Static Environments and Dynamic Environments, and several stand alone classes. Static Environment provides the experimental setup before any actual measurement will run and should stay constant while the entire experiment is running. There current Static Environment classes are: Static Environments all have the following functions (VIs)

- Read Config From File – Loads all the settings from a file into the class
- Write Config To File – Writes all the settings to a file from the class
- Configure Environment – configures all the hardware associated with the static environment (PPMS, Fridge, . . . )
- Set Initial Environment – returns true/false if the environment should be changed before the measurement process begins
- Set Final Environment – returns true/false if the environment should be changed after the measurement process finishes
- Setup Initial Static Environment – Uses the hardware to set up the environment hardware before the measurement process begins
- Setup Final Static Environment – Uses the hardware to set up the environment hardware after the measurement process finishes
- Measurement Names – The column name(s) for any data taken. E.g. Temperature for monitoring the temperature as data is taken
- Measure – Record any data associated with the static environment

### B.2.2 Dynamic Environments

Dynamic Environments change the environment over the course of a measurement. The Dynamic Sequence class can be used to chain multiple Dynamic Environments to execute one after another, this is different from chaining launchers which is explained later. Dynamic Environments all have the following functions (VIs)

- Read Config From File – Loads all the settings from a file into the class
- Write Config To File – Writes all the settings to a file from the class
- Read/Write Current Step N – gets/sets the current step counter of the environment
- Increment N – Increments the step counter
- Read/Write Number of Steps – gets/sets the total number of steps the environment should take

- Configure environment - configures all the hardware associated with the static environment (PPMS, Fridge, voltmeters, . . . )
- Check if finished – Returns true if the environment is finished taking all data
- Cleanup – run after measurement finishes to make sure hardware is safe to leave (e.g. no current on)
- Get Next Step Text – get the text to display to the user to let them know what the measurement is doing and monitor progress
- Get Static Environment – Produces a static state configuration to measure a single data point
- Setup Step – Sets the hardware to the desired state before data is measured

- Measurement Names - The column name(s) for any data taken. E.g. Temperature for monitoring the temperature as data is taken
- Measure Data – Record any data associated with the dynamic environment
- Set Write To File – Set this to false to avoid generating a new file name when writing to file (this is a bit of a hack)

### B.2.3 Stand alone classes

Stand alone classes:

- System information – Helper class that contains all the information for cryogenic hardware configurations (PPMS, Fridge, He3, Dip)

## B.3 Main Algorithm

For any measurement run the “Generic ND Data Collection.vi” takes in an array of Static Environments, array of Dynamic Environments, and System Information, and file info. The “Generic ND Data Collection.vi” then does the following

1. Configures all hardware, launches Generic Plot Window, sets starting parameters
2. Sets up the Static Environment(s) in the array in the order given
- a. Checks each to see if the initial environment should be set
- b. Displays the setup text to the user
- c. Sets the hardware for the initial environment
3. For each Dynamic environment in the array
- a. Sets up step X of the current Dynamic Environment
- b. Measures data for the all dynamic environments, all static environments, and system
- c. Writes all data to the data file
- d. Increments the counter of the last Dynamic Environment, check to see if finished
- If finished increment second to last dynamic environment and reset own counter to 0
- Continues down the chain until one is not finished and can just be incremented by 1 or all are done
- e. If all environments are not finished go to (a), otherwise continue
4. Cleanup all Dynamic Environment hardware (e.g. turn off current)
5. Sets up the Static Environment(s) in the array in the order given to their ‘final’ configuration
6. Cleanup any system hardware

The dynamic environment execution sequence is a bit complicated to allow them to be interleaved. For example, take Temperature, Magnetic Field, then Current environments in an array. For each Temperature point, the program would sweep the entire magnetic field, and for each magnetic field point within that a current sweep would run. This lets us set up a single launcher and run a long 4D measurement. For most of the launchers, they offer a static current/voltage configuration which is just translated into a dynamic current/voltage with only a single data point. “Set Write To File.vi” is used to prevent each data point producing a separate file in this case.

## B.4 File format (Parameters to/from File)

Each data file contains all the settings for an individual run before the data, so both are kept together. The parameter information is stored in the .ini format because it is one of the few LabVIEW supports. Data is appended immediately after that in tab separated columns (CSV format) with the first row containing all the measurement names from dynamic and static environment classes. The parameters VIs can both read and write to files to keep the logic together and consistent.

## **B.5 Hardware (System Specific Subprograms)**

In an effort to be able to run everything on new equipment without having to fork the program the hardware interfaces have been separated out and abstracted away as much as possible. The sub-folders contain specific functions written for each piece of hardware to make things simpler. The main hardware interfaces contain VIs for reading/setting magnetic fields, temperature, gate voltage, and rotator positions. Each contain the code for specific platforms under case structures so each machine can individually edited or new ones can be added.

## **B.6 DC (Sourcing and Measuring)**

**Subprograms** This section contains the configuration and measurement programs responsible for managing current and voltage sources and measurement. It makes use of the system specific subprograms for individual helper functions but is largely designed to abstract away each specific action so each meter and source can be run the same as any of the others. The main program will start by calling the configure voltage and source VIs for each machine it will use, these VIs will call a several VIs to ensure the machine is in a consistent state for each run. Sourcing and Measuring are handled by a similar set of VIs that seek to provide a consistent way of measuring and sourcing current and voltage across devices. The main 2 VIs that work with all of these are “Measure V Source I.vi” and “Measure I Source V.vi.” These handle the source and measurement timing and flip, subtract bias, and static modes. They also display the data as it is taken so you can monitor how the measurement is doing.

## **B.7 Queueing measurements**

When each launcher runs a measurement it calls “Add to Execution queue.vi.” This VI adds the environment arrays to a queue and starts an asynchronous call to “Generic ND Data Collection.vi.” “Generic ND Data Collection.vi” will then take the environment arrays out of the queue in order of when they were added. This queueing structure allows more than one measurement to be set without the need to wait for the first to finish. “MultiSequence Execution.vi” can edit and rearrange the queue. Any VI that touches the queue should first have acquired the semaphore “ExecutionQueue.” This prevents more than one VI from changing things at the same time and introducing a race condition.



# **Appendix C |**

## **Additional $\alpha$ -In<sub>2</sub>Se<sub>3</sub> Figures**

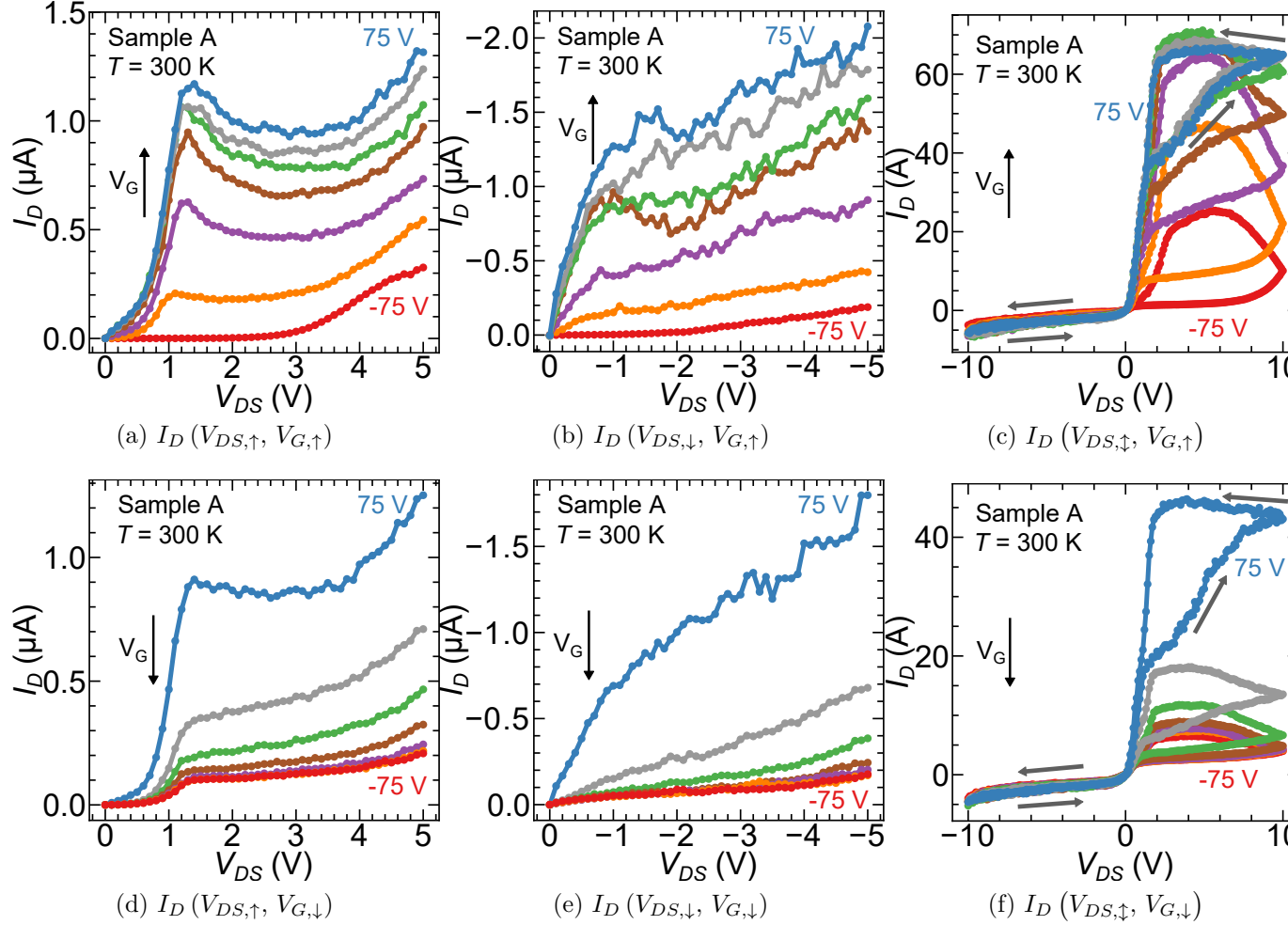
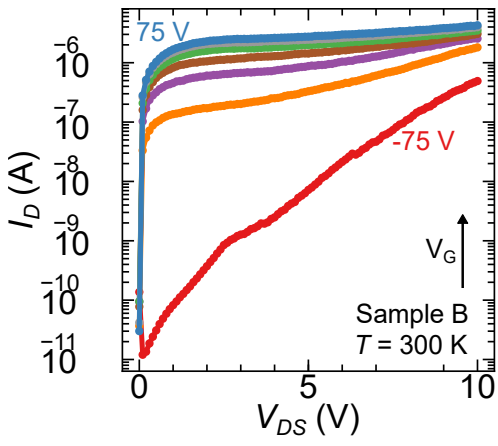
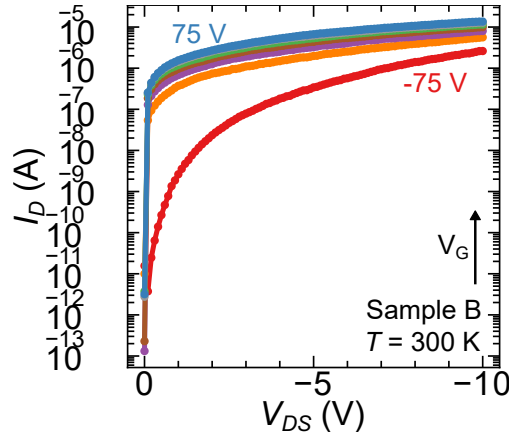


Figure C.1: Sample A:  $I_D(V_{DS}, V_G)$

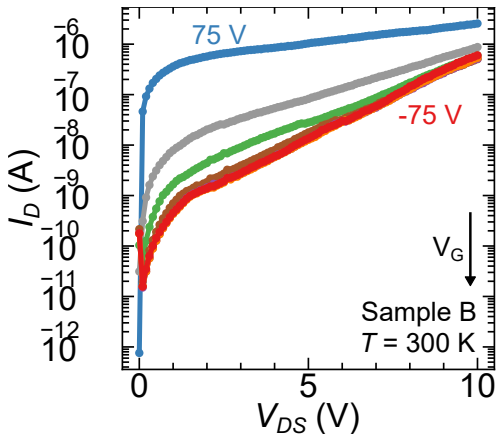
$I_D(V_{DS})$  of sample A, linear scaling of data shown in figure 4.3. (a & d) Show positive-increasing  $V_{DS}$  and (b & e) negative-decreasing  $V_{DS}$ . (c & f) hysteresis in  $I_D$  as  $V_{DS}$  is cycled from 0 V, 10 V, -10 V, to 0 V. Measurements (a - c) are taken while  $V_G$  is held at 25 V intervals that increase sequentially for each curve, and (d - f) decreasing for  $V_G$  intervals. All measurements were done at 300 K.



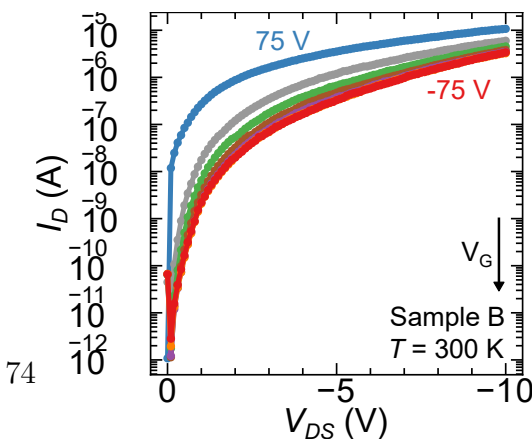
(a)  $I_D (V_{DS,\uparrow}, V_{G,\uparrow})$



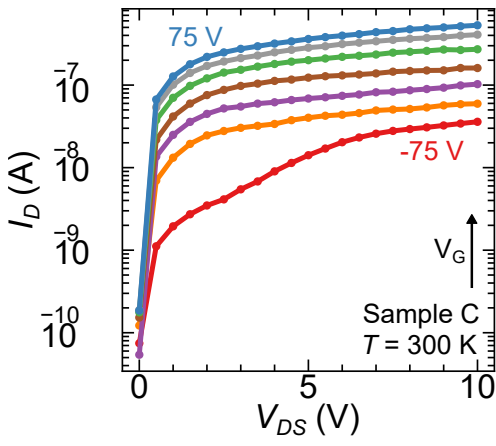
(b)  $I_D (V_{DS,\downarrow}, V_{G,\uparrow})$



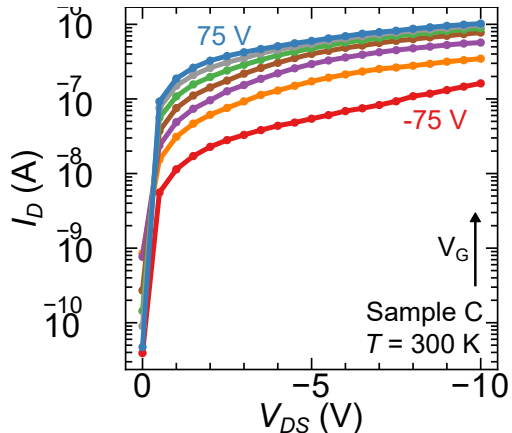
(c)  $I_D (V_{DS,\uparrow}, V_{G,\downarrow})$



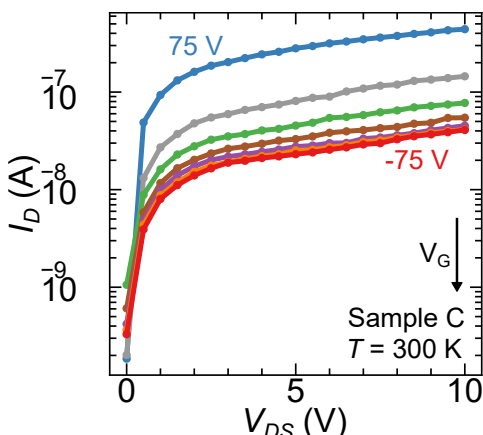
(d)  $I_D (V_{DS,\downarrow}, V_{G,\downarrow})$



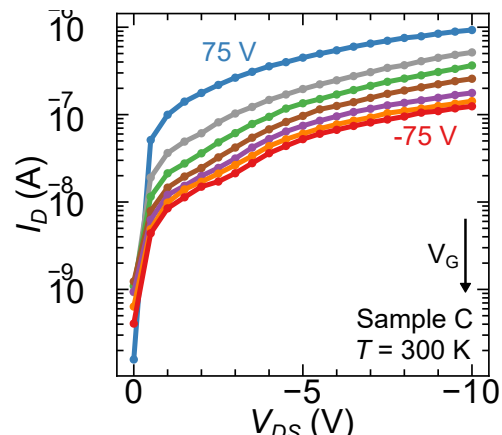
(a)  $I_D (V_{DS,\uparrow}, V_{G,\uparrow})$



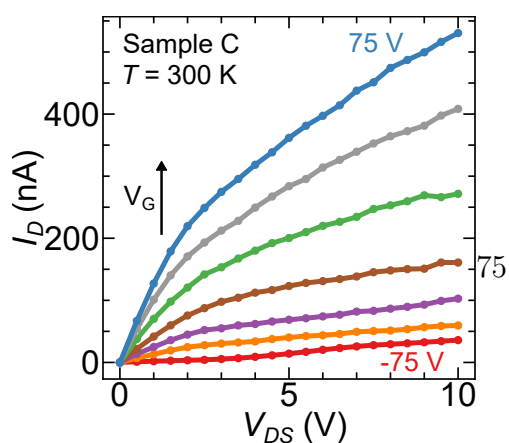
(b)  $I_D (V_{DS,\downarrow}, V_{G,\uparrow})$



(c)  $I_D (V_{DS,\uparrow}, V_{G,\downarrow})$



(d)  $I_D (V_{DS,\downarrow}, V_{G,\downarrow})$



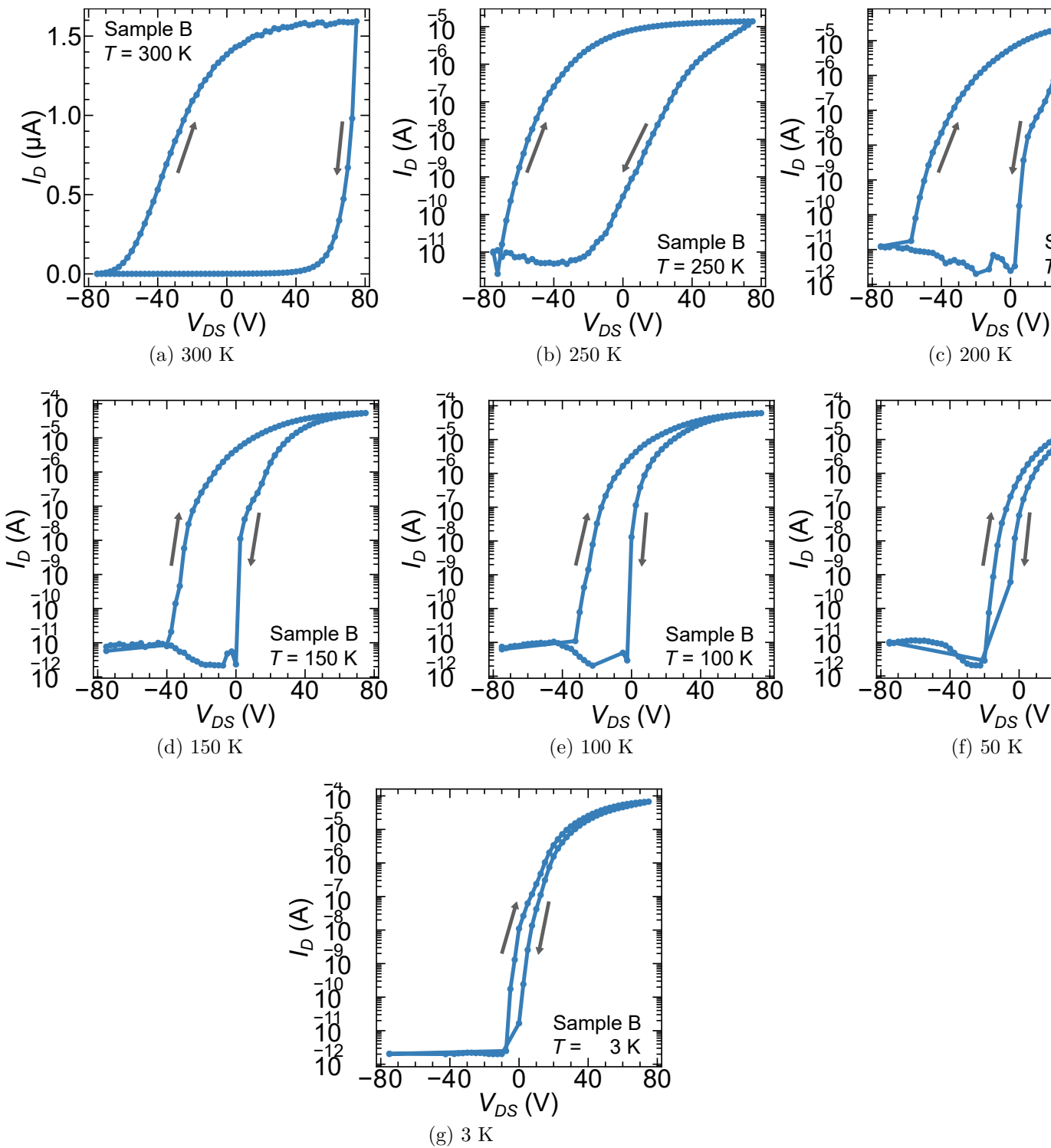


Figure C.4: Sample B:  $I_D (V_G)$  transfer characteristics  $I_D (V_G)$  of sample B at the indicated fixed temperatures. Each was measured with  $V_{DS} = 0.1 \text{ V}$  as  $V_G$  was cycled, a clockwise hysteresis loop was seen at all temperatures.

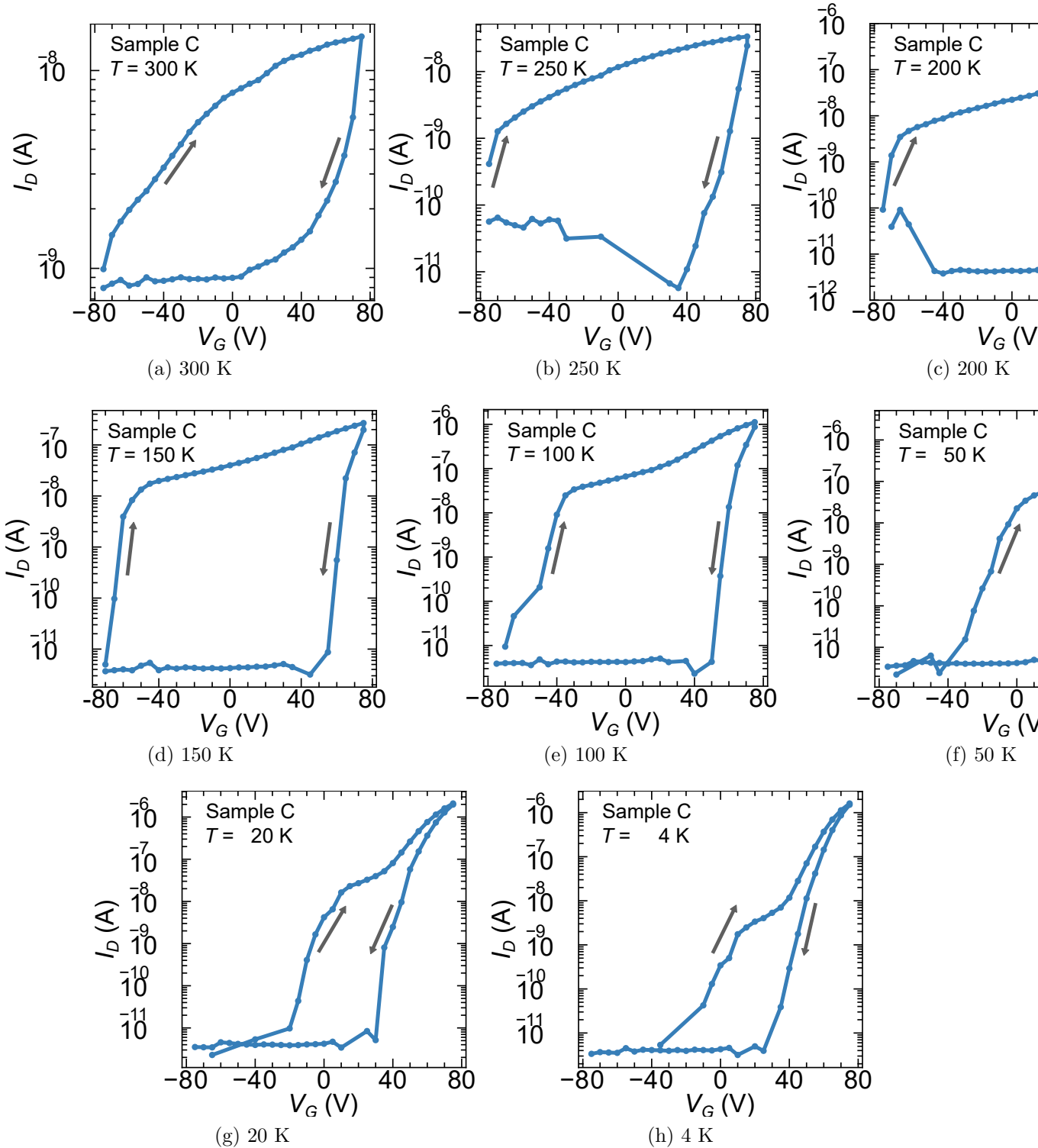


Figure C.5: Sample C:  $I_D (V_G)$  transfer characteristics  $I_D (V_G)$  of sample C at the indicated fixed temperatures. Each was measured with  $V_{DS} = 0.1 \text{ V}$  as  $V_G$  was cycled, a clockwise hysteresis loop was seen at all temperatures.

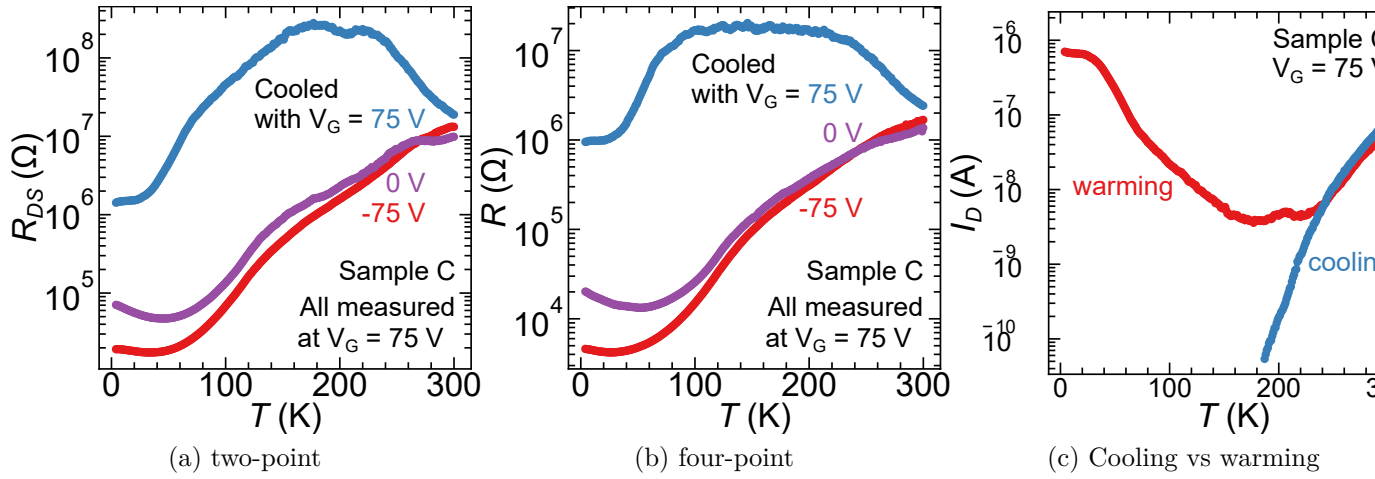


Figure C.6: Sample C: effects of warming and cooling while gated

Sample C (a) two-point and (b) four-point resistance measured at  $V_G = 75$  V with increasing temperature from 2 to 300 K. Before each measurement, sample were cycled at 300 K to  $V_G = -75$  V, then fixed at 25, 50, and 75 V as indicated, then finally cooled from 300 to 2 K with the  $V_G$  still held constant. (c) Sample was cycled at 2 K (300 K) to  $V_G = -75$  V then to 75 V and held fixed.  $I_D$  was measured while sample was warmed (cooled) with constant  $V_G$  and  $V_{DS} = 1$  V.

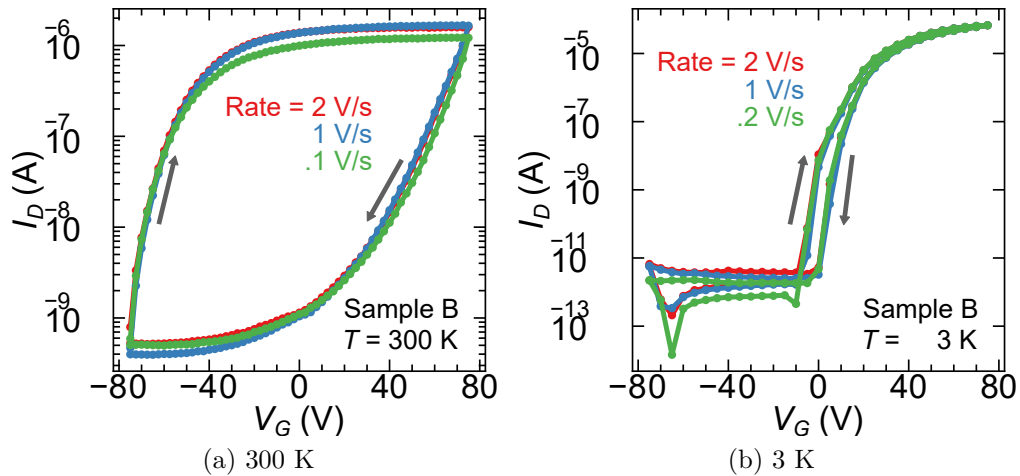


Figure C.7: Sample B:  $I_D$  ( $V_G$ ),  $V_G$  rate dependence

$I_D$  ( $V_G$ ) of sample C taken at (a) 300 K and (b) 3 K. Each curve was taken with  $V_G$  increased and decreased at the indicated rate with  $V_{DS} = 0.1$  V.

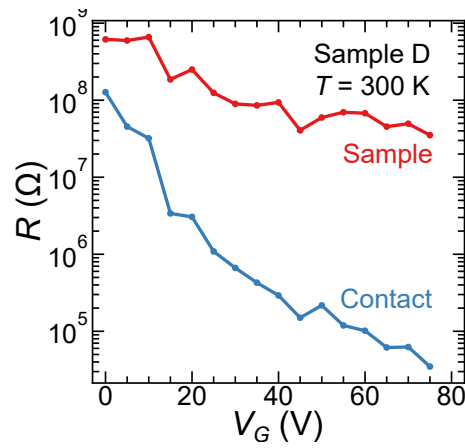


Figure C.8: Sample D: contact resistance

Sample D  $R(V_G)$  contact and four-point sample resistance, taken at 300 K with increasing  $V_G$ .

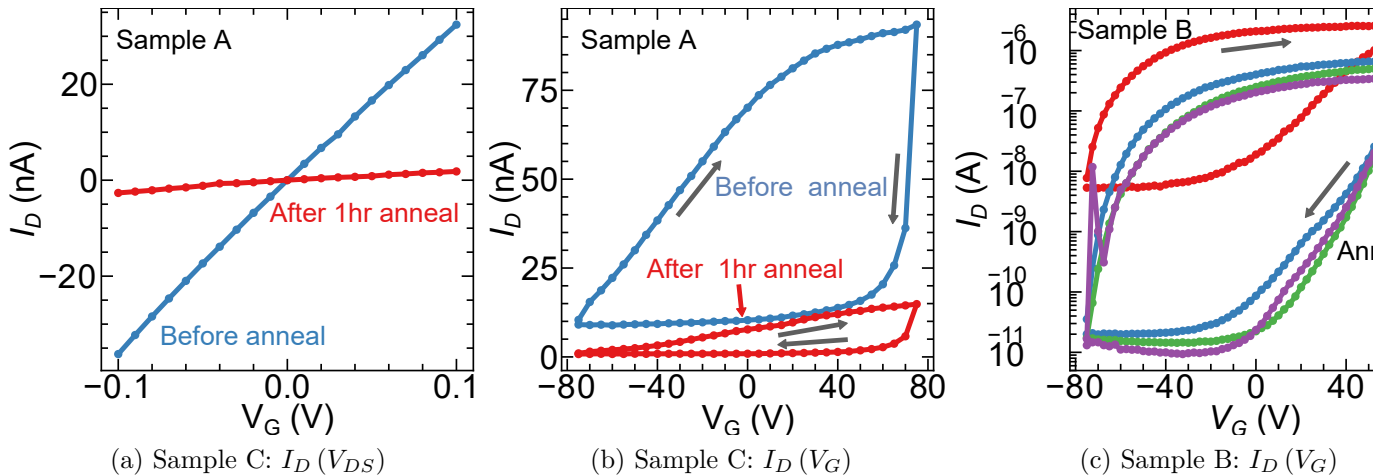


Figure C.9: Sample A and B: annealing

Samples A (a & b) and B (c) were annealed in vacuum at 400 K in 1 hour intervals. (a) Show  $I_D(V_{DS})$  measurements and (b & c)  $I_D(V_G)$ , each taken at 300 K.

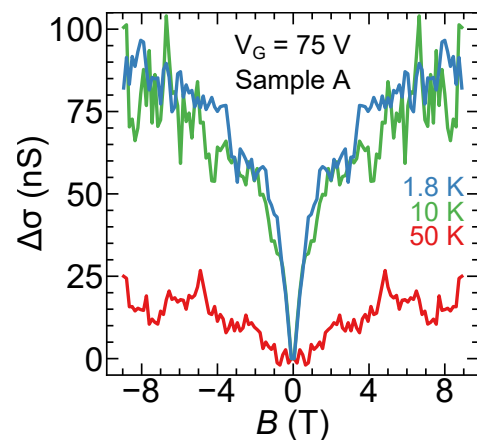


Figure C.10: Sample A: magnetoconductance  
The magnetoconductance of sample A taken at 1.8, 10, and 50 K.

# Bibliography

- [1] SHI, P.-P., Y.-Y. TANG, P.-F. LI, W.-Q. LIAO, Z.-X. WANG, Q. YE, and R.-G. XIONG (2016) “Symmetry breaking in molecular ferroelectrics,” *Chemical Society Reviews*, **45**(14), pp. 3811–3827, 00176.  
URL <https://www.doi.org/10.1039/C5CS00308C>
- [2] (2020) “A century of ferroelectricity,” *Nature Materials*, **19**(2), pp. 129–129, number: 2 Publisher: Nature Publishing Group.  
URL <https://www.doi.org/10/gg9tbs>
- [3] VALASEK, J. (1921) “Piezo-Electric and Allied Phenomena in Rochelle Salt,” *Physical Review*, **17**(4), pp. 475–481, zSCC: 0001114 Publisher: American Physical Society.  
URL <https://www.doi.org/10/d994m8>
- [4] DEVONSHIRE, A. F. (1949) “XCVI. Theory of barium titanate,” *The London, Edinburgh, and Dublin Philosophical Magazine and Journal of Science*, **40**(309), pp. 1040–1063, zSCC: 0001424 Publisher: Taylor & Francis \_eprint: <https://doi.org/10.1080/14786444908561372>.  
URL <https://www.doi.org/10.ghz28v>
- [5] SCOTT, J. F. (2007) “Applications of Modern Ferroelectrics,” *Science*, **315**(5814), pp. 954–959, 02469 ZSCC: 0002469 Publisher: American Association for the Advancement of Science Section: Review.  
URL <https://www.doi.org/10.1126/science.1129564>
- [6] SCOTT, J. F. and C. A. P. D. ARAUJO (1989) “Ferroelectric Memories,” *Science*, **246**(4936), pp. 1400–1405, publisher: American Association for the Advancement of Science Section: Articles.  
URL <https://www.doi.org/10.1126/science.246.4936.1400>
- [7] TUNG, R. T. . (2014) “The physics and chemistry of the Schottky barrier height,” *Applied Physics Reviews*, **1**(1), p. 011304.  
URL <https://www.doi.org/10.1063/1.4858400>
- [8] LIU, Y., J. GUO, E. ZHU, L. LIAO, S.-J. LEE, M. DING, I. SHAKIR, V. GAMBIN, Y. HUANG, and X. DUAN (2018) “Approaching the Schottky–Mott limit in van

- der Waals metal–semiconductor junctions,” *Nature*, **557**(7707), pp. 696–700, 00173. URL <https://www.doi.org/10/gdg5pp>
- [9] GONG, C., L. COLOMBO, R. M. WALLACE, and K. CHO (2014) “The Unusual Mechanism of Partial Fermi Level Pinning at Metal–MoS<sub>2</sub> Interfaces,” *Nano Letters*, **14**(4), pp. 1714–1720. URL <https://www.doi.org/10/f5x5dw>
- [10] KITTEL, C. (2005) *Introduction to Solid State Physics*, 8th ed., Wiley, 00000.
- [11] O’SULLIVAN, C. M. and J. A. MURPHY (2012) “Schottky Diodes,” *Field Guide to Terahertz Sources, Detectors, and Optics*, pp. 35–37, 00001. URL <https://www.doi.org/10/gf9xn5>
- [12] ELHADIDY, H., J. SIKULA, and J. FRANC (2011) “Symmetrical current–voltage characteristic of a metal–semiconductor–metal structure of Schottky contacts and parameter retrieval of a CdTe structure,” *Semiconductor Science and Technology*, **27**(1), p. 015006, 00044. URL <https://www.doi.org/10/bhsvcr>
- [13] OSVALD, J. (2015) “Back-to-back connected asymmetric Schottky diodes with series resistance as a single diode,” *physica status solidi (a)*, **212**(12), pp. 2754–2758, 00014. URL <https://www.doi.org/10/f3cxd2>
- [14] NOUCHI, R. (2014) “Extraction of the Schottky parameters in metal-semiconductor-metal diodes from a single current-voltage measurement,” *Journal of Applied Physics*, **116**(18), p. 184505, 00025. URL <https://www.doi.org/10/ggjfqm>
- [15] HOROWITZ, P. and W. HILL (2015) *The Art of Electronics*, 3 edition ed., Cambridge University Press, New York, NY, 05483.
- [16] BAIN, A. K. and P. CHAND (2017) *Ferroelectrics: Principles and Applications*, 1 edition ed., Wiley-VCH, zSCC: 0000025.
- [17] LIU, J. and S. T. PANTELIDES (2018) “Mechanisms of Pyroelectricity in Three- and Two-Dimensional Materials,” *Physical Review Letters*, **120**(20), p. 207602, 00014 ZSCC: 0000014 Publisher: American Physical Society. URL <https://www.doi.org/10/gdg636>
- [18] IEVLEV, A. V., S. KC, R. K. VASUDEVAN, Y. KIM, X. LU, M. ALEXE, V. R. COOPER, S. V. KALININ, and O. S. OVCHINNIKOVA (2019) “Non-conventional mechanism of ferroelectric fatigue via cation migration,” *Nature Communications*, **10**(1), pp. 1–8, zSCC: 0000002 Number: 1 Publisher: Nature Publishing Group. URL <https://www.doi.org/10.1038/s41467-019-11089-w>

- [19] GENENKO, Y. A., J. GLAUM, M. J. HOFFMANN, and K. ALBE (2015) "Mechanisms of aging and fatigue in ferroelectrics," *Materials Science and Engineering: B*, **192**, pp. 52–82, zSCC: 0000157.  
URL <https://www.doi.org/10.1016/j.mseb.2014.10.003>
- [20] DAI, J. (2020) *Ferroic Materials for Smart Systems*, John Wiley & Sons, Ltd, 00000 ISBN: 9783527815388.  
URL <https://www.doi.org/10.1002/9783527815388>
- [21] WONG, C. K. and F. G. SHIN (2007) "A simplified treatment of the Landau theory of phase transitions for thin ferroelectric films," *American Journal of Physics*, **76**(1), pp. 31–38, 00004 Publisher: American Association of Physics Teachers.  
URL <https://www.doi.org/10.dpz4k3>
- [22] PARK, B.-E., H. ISHIWARA, M. OKUYAMA, S. SAKAI, and S.-M. YOON (eds.) (2020) *Ferroelectric-Gate Field Effect Transistor Memories: Device Physics and Applications*, Topics in Applied Physics, 2 ed., Springer Singapore, zSCC: NoCitationData[s0].  
URL <https://www.doi.org/10.1007/978-981-15-1212-4>
- [23] GEORGIOU, V., D. VEKSLER, J. P. CAMPBELL, P. R. SHRESTHA, J. T. RYAN, D. E. IOANNOU, and K. P. CHEUNG (2018) "Ferroelectricity in Polar Polymer-Based FETs: A Hysteresis Analysis," *Advanced Functional Materials*, **28**(10), zSCC: 0000003 Publisher: John Wiley & Sons, Ltd.  
URL <https://www.doi.org/10.1002/adfm.201705250>
- [24] ——— (2018) "Ferroelectricity in Polar Polymer-Based FETs: A Hysteresis Analysis," *Advanced Functional Materials*, **28**(10), p. 1705250, 00003 Publisher: John Wiley & Sons, Ltd.  
URL <https://www.doi.org/10.ggqbnq>
- [25] KOHLSTEDT, H., N. A. PERTSEV, J. RODRÍGUEZ CONTRERAS, and R. WASER (2005) "Theoretical current-voltage characteristics of ferroelectric tunnel junctions," *Physical Review B*, **72**(12), p. 125341, zSCC: 0000355 Publisher: American Physical Society.  
URL <https://www.doi.org/10.1103/PhysRevB.72.125341>
- [26] SHEN, X.-W., Y.-W. FANG, B.-B. TIAN, and C.-G. DUAN (2019) "Two-Dimensional Ferroelectric Tunnel Junction: The Case of Monolayer In:SnSe/SnSe/Sb:SnSe Homostructure," *ACS Applied Electronic Materials*, **1**(7), pp. 1133–1140, zSCC: 0000003 Publisher: American Chemical Society.  
URL <https://www.doi.org/10.1021/acsaelm.9b00146>
- [27] ANDERSON, P. W. and E. I. BLOUNT (1965) "Symmetry Considerations on Martensitic Transformations: "Ferroelectric" Metals?" *Physical Review Letters*, **14**(7), pp. 217–219, zSCC: 0000351 Publisher: American Physical Society.  
URL <https://www.doi.org/10.1103/PhysRevLett.14.217>

- [28] SHI, Y., Y. GUO, X. WANG, A. J. PRINCEP, D. KHALYAVIN, P. MANUEL, Y. MICHIE, A. SATO, K. TSUDA, S. YU, M. ARAI, Y. SHIRAKO, M. AKAOGI, N. WANG, K. YAMAURA, and A. T. BOOTHROYD (2013) “A ferroelectric-like structural transition in a metal,” *Nature Materials*, **12**(11), pp. 1024–1027, zSCC: NoCitationData[s0] Number: 11 Publisher: Nature Publishing Group.  
URL <https://www.doi.org/10.1038/nmat3754>
- [29] BENEDEK, N. A. and T. BIROL (2016) “‘Ferroelectric’ metals reexamined: fundamental mechanisms and design considerations for new materials,” *Journal of Materials Chemistry C*, **4**(18), pp. 4000–4015, zSCC: 0000067 Publisher: The Royal Society of Chemistry.  
URL <https://www.doi.org/10.1039/C5TC03856A>
- [30] PADMANABHAN, H., Y. PARK, D. PUGGIONI, Y. YUAN, Y. CAO, L. GASPAROV, Y. SHI, J. CHAKHALIAN, J. M. RONDINELLI, and V. GOPALAN (2018) “Linear and nonlinear optical probe of the ferroelectric-like phase transition in a polar metal, LiOsO<sub>3</sub>,” *Applied Physics Letters*, **113**(12), p. 122906, zSCC: NoCitationData[s0] Publisher: American Institute of Physics.  
URL <https://www.doi.org/10.1063/1.5042769>
- [31] JIN, F., L. WANG, A. ZHANG, J. JI, Y. SHI, X. WANG, R. YU, J. ZHANG, E. W. PLUMMER, and Q. ZHANG (2019) “Raman interrogation of the ferroelectric phase transition in polar metal LiOsO<sub>3</sub>,” *Proceedings of the National Academy of Sciences*, **116**(41), pp. 20322–20327, zSCC: 0000000 Publisher: National Academy of Sciences Section: Physical Sciences.  
URL <https://www.doi.org/10.1073/pnas.1908956116>
- [32] LAURITA, N. J., A. RON, J.-Y. SHAN, D. PUGGIONI, N. Z. KOOCHER, K. YAMAURA, Y. SHI, J. M. RONDINELLI, and D. HSIEH (2019) “Evidence for the weakly coupled electron mechanism in an Anderson-Blount polar metal,” *Nature Communications*, **10**(1), pp. 1–7, zSCC: 0000005 Number: 1 Publisher: Nature Publishing Group.  
URL <https://www.doi.org/10.1038/s41467-019-11172-2>
- [33] LEI, S., M. GU, D. PUGGIONI, G. STONE, J. PENG, J. GE, Y. WANG, B. WANG, Y. YUAN, K. WANG, Z. MAO, J. M. RONDINELLI, and V. GOPALAN (2018) “Observation of Quasi-Two-Dimensional Polar Domains and Ferroelastic Switching in a Metal, Ca<sub>3</sub>Ru<sub>2</sub>O<sub>7</sub>,” *Nano Letters*, **18**(5), pp. 3088–3095, zSCC: NoCitationData[s0] Publisher: American Chemical Society.  
URL <https://www.doi.org/10.1021/acs.nanolett.8b00633>
- [34] TAKAHASHI, K. S., Y. MATSUBARA, M. S. BAHRAMY, N. OGAWA, D. HASHIZUME, Y. TOKURA, and M. KAWASAKI (2017) “Polar metal phase stabilized in strained La-doped BaTiO<sub>3</sub> films,” *Scientific Reports*, **7**(1), pp. 1–7, zSCC: 0000017 Number: 1 Publisher: Nature Publishing Group.  
URL <https://www.doi.org/10.1038/s41598-017-04635-3>

- [35] DU, D., A. LIM, C. ZHANG, P. J. STROHBEEN, E. H. SHOUROV, F. RODOLAKIS, J. L. MCCHESENEY, P. VOYLES, D. C. FREDRICKSON, and J. K. KAWASAKI (2019) “High electrical conductivity in the epitaxial polar metals LaAuGe and LaPtSb,” *APL Materials*, **7**(12), p. 121107, zSCC: 0000002 Publisher: AIP Publishing LLC.  
URL <https://www.doi.org/10.1063/1.5132339>
- [36] FEI, Z., W. ZHAO, T. A. PALOMAKI, B. SUN, M. K. MILLER, Z. ZHAO, J. YAN, X. XU, and D. H. COBDEN (2018) “Ferroelectric switching of a two-dimensional metal,” *Nature*, **560**(7718), pp. 336–339, zSCC: 0000096 Number: 7718 Publisher: Nature Publishing Group.  
URL <https://www.doi.org/10.1038/s41586-018-0336-3>
- [37] SHARMA, P., F.-X. XIANG, D.-F. SHAO, D. ZHANG, E. Y. TSYMBAL, A. R. HAMILTON, and J. SEIDEL (2019) “A room-temperature ferroelectric semimetal,” *Science Advances*, **5**(7), p. eaax5080, zSCC: 0000009 Publisher: American Association for the Advancement of Science Section: Research Article.  
URL <https://www.doi.org/10.1126/sciadv.aax5080>
- [38] STONE, G., D. PUGGIONI, S. LEI, M. GU, K. WANG, Y. WANG, J. GE, X.-Z. LU, Z. MAO, J. M. RONDINELLI, and V. GOPALAN (2019) “Atomic and electronic structure of domains walls in a polar metal,” *Physical Review B*, **99**(1), p. 014105, zSCC: 0000007 Publisher: American Physical Society.  
URL <https://www.doi.org/10.1103/PhysRevB.99.014105>
- [39] PUGGIONI, D., G. GIOVANNETTI, and J. M. RONDINELLI (2018) “Polar metals as electrodes to suppress the critical-thickness limit in ferroelectric nanocapacitors,” *Journal of Applied Physics*, **124**(17), p. 174102, zSCC: 0000007 Publisher: AIP Publishing LLC.  
URL <https://www.doi.org/10.1063/1.5049607>
- [40] FANG, Y.-W. and H. CHEN (2020) “Design of a multifunctional polar metal via first-principles high-throughput structure screening,” *Communications Materials*, **1**(1), pp. 1–8, zSCC: 0000001 Number: 1 Publisher: Nature Publishing Group.  
URL <https://www.doi.org/10.1038/s43246-019-0005-6>
- [41] TOKURA, Y. and N. NAGAOSA (2018) “Nonreciprocal responses from non-centrosymmetric quantum materials,” *Nature Communications*, **9**(1), pp. 1–14, zSCC: 0000067 Number: 1 Publisher: Nature Publishing Group.  
URL <https://www.doi.org/10.1038/s41467-018-05759-4>
- [42] OKAMOTO, H., H. OKAMOTO, and K. CENZUAL (2006) *In-Se Phase Diagram ASM Alloy Phase Diagrams Center*, ASM International, Materials Park, OH.
- [43] HAN, G., Z.-G. CHEN, J. DRENNAN, and J. ZOU (2014) “Indium Selenides: Structural Characteristics, Synthesis and Their Thermoelectric Performances,”

- Small*, **10**(14), pp. 2747–2765, 00104.  
URL <https://www.doi.org/10/f2spnz>
- [44] LIU, L., J. DONG, J. HUANG, A. NIE, K. ZHAI, J. XIANG, B. WANG, F. WEN, C. MU, Z. ZHAO, Y. GONG, Y. TIAN, and Z. LIU (2019) “Atomically Resolving Polymorphs and Crystal Structures of In<sub>2</sub>Se<sub>3</sub>,” *Chemistry of Materials*, **31**(24), pp. 10143–10149, 00000 ZSCC: 0000000 Publisher: American Chemical Society 3 citations (Crossref) [2021-02-02].  
URL <https://www.doi.org/10.1021/acs.chemmater.9b03499>
- [45] JIANG, Y., Q. WANG, L. HAN, X. ZHANG, L. JIANG, Z. WU, Y. LAI, D. WANG, and F. LIU (2019) “Construction of In<sub>2</sub>Se<sub>3</sub>/MoS<sub>2</sub> heterojunction as photoanode toward efficient photoelectrochemical water splitting,” *Chemical Engineering Journal*, **358**, pp. 752–758, zSCC: 0000008.  
URL <https://www.doi.org/10.1016/j.cej.2018.10.088>
- [46] LI, Y., J. GAO, Q. LI, M. PENG, X. SUN, Y. LI, G. YUAN, W. WEN, and M. MEYYAPPAN (2011) “Thermal phase transformation of In<sub>2</sub>Se<sub>3</sub> nanowires studied by in situ synchrotron radiation X-ray diffraction,” *Journal of Materials Chemistry*, **21**(19), pp. 6944–6947, zSCC: NoCitationData[s0] Publisher: The Royal Society of Chemistry.  
URL <https://www.doi.org/10.1039/C1JM10419E>
- [47] KANG, D., T. RIM, C.-K. BAEK, M. MEYYAPPAN, and J.-S. LEE (2014) “Thermally Phase-Transformed In<sub>2</sub>Se<sub>3</sub> Nanowires for Highly Sensitive Photodetectors,” *Small*, **10**(18), pp. 3795–3802, zSCC: 0000018 \_eprint: <https://onlinelibrary.wiley.com/doi/pdf/10.1002/smll.201400373>.  
URL <https://www.doi.org/10.1002/smll.201400373>
- [48] MANOLIKAS, C. (1988) “New results on the phase transformations of In<sub>2</sub>Se<sub>3</sub>,” *Journal of Solid State Chemistry*, **74**(2), pp. 319–328, zSCC: 0000027.  
URL [https://www.doi.org/10.1016/0022-4596\(88\)90361-1](https://www.doi.org/10.1016/0022-4596(88)90361-1)
- [49] VAN LANDUYT, J., G. VAN TENDELOO, and S. AMELINCKX (1975) “Phase transitions in In<sub>2</sub>Se<sub>3</sub> as studied by electron microscopy and electron diffraction,” *physica status solidi (a)*, **30**(1), pp. 299–314, zSCC: 0000078 Publisher: John Wiley & Sons, Ltd.  
URL <https://www.doi.org/10.1002/pssa.2210300131>
- [50] KÜPERS, M., P. M. KONZE, A. MELEDIN, J. MAYER, U. ENGLERT, M. WUTTIG, and R. DRONSKOWSKI (2018) “Controlled Crystal Growth of Indium Selenide, In<sub>2</sub>Se<sub>3</sub>, and the Crystal Structures of  $\alpha$ -In<sub>2</sub>Se<sub>3</sub>,” *Inorganic Chemistry*, **57**(18), pp. 11775–11781, zSCC: 0000012 Publisher: American Chemical Society.  
URL <https://www.doi.org/10.1021/acs.inorgchem.8b01950>
- [51] OSAMURA, K., Y. MURAKAMI, and Y. TOMIE (1966) “Crystal Structures of  $\alpha$ -and  $\beta$ -Indium Selenide, In<sub>2</sub>Se<sub>3</sub>,” *Journal of the Physical Society of Japan*, **21**(9),

- pp. 1848–1848, zSCC: 0000106 Publisher: The Physical Society of Japan.  
URL <https://www.doi.org/10.1143/JPSJ.21.1848>
- [52] VILAPLANA, R., S. G. PARRA, A. JORGE-MONTERO, P. RODRÍGUEZ-HERNÁNDEZ, A. MUÑOZ, D. ERRANDONEA, A. SEGURA, and F. J. MANJÓN (2018) “Experimental and Theoretical Studies on  $\alpha$ -In<sub>2</sub>Se<sub>3</sub> at High Pressure,” *Inorganic Chemistry*, **57**(14), pp. 8241–8252, zSCC: 0000006 Publisher: American Chemical Society.  
URL <https://www.doi.org/10.1021/acs.inorgchem.8b00778>
- [53] YE, J., S. SOEDA, Y. NAKAMURA, and O. NITTONO (1998) “Crystal Structures and Phase Transformation in In<sub>2</sub>Se<sub>3</sub> Compound Semiconductor,” *Japanese Journal of Applied Physics*, **37**(8R), p. 4264, zSCC: 0000106 Publisher: IOP Publishing.  
URL <https://www.doi.org/10.1143/JJAP.37.4264>
- [54] POPOVIĆ, S., A. TONEJC, B. ČELUSTKA, B. GRŽETA-PLENKOVIĆ, and R. TROJKO (1979) “Revised and new crystal data for indium selenides,” *Journal of Applied Crystallography*, **12**(4), pp. 416–420, 00135.  
URL <https://www.doi.org/10.fwjxs7>
- [55] NGUYEN, T. H., V. Q. NGUYEN, A. T. DUONG, and S. CHO (2019) “2D semiconducting  $\alpha$ -In<sub>2</sub>Se<sub>3</sub> single crystals: Growth and huge anisotropy during transport,” *Journal of Alloys and Compounds*, **810**, p. 151968, zSCC: 0000001.  
URL <https://www.doi.org/10.1016/j.jallcom.2019.151968>
- [56] TAO, X. and Y. GU (2013) “Crystalline–Crystalline Phase Transformation in Two-Dimensional In<sub>2</sub>Se<sub>3</sub> Thin Layers,” *Nano Letters*, **13**(8), pp. 3501–3505, zSCC: 0000102 Publisher: American Chemical Society.  
URL <https://www.doi.org/10.1021/nl400888p>
- [57] JACOBS-GEDRIM, R. B., M. SHANMUGAM, N. JAIN, C. A. DURCAN, M. T. MURPHY, T. M. MURRAY, R. J. MATYI, R. L. MOORE, and B. YU (2014) “Extraordinary Photoresponse in Two-Dimensional In<sub>2</sub>Se<sub>3</sub> Nanosheets,” *ACS Nano*, **8**(1), pp. 514–521, zSCC: 0000231 Publisher: American Chemical Society.  
URL <https://www.doi.org/10.1021/nn405037s>
- [58] LUTZ, H. D., M. FISCHER, H. P. BALDUS, and R. BLACHNIK (1988) “Zur polymorphie des In<sub>2</sub>Se<sub>3</sub>,” *Journal of the Less Common Metals*, **143**(1), pp. 83–92, zSCC: 0000031.  
URL [https://www.doi.org/10.1016/0022-5088\(88\)90033-1](https://www.doi.org/10.1016/0022-5088(88)90033-1)
- [59] LI, W., F. P. SABINO, F. CRASTO DE LIMA, T. WANG, R. H. MIWA, and A. JANOTTI (2018) “Large disparity between optical and fundamental band gaps in layered  $\{\mathrm{In}\}_2\{\mathrm{Se}\}_3$ ,” *Physical Review B*, **98**(16), p. 165134, zSCC: NoCitationData[s0] Publisher: American Physical Society.  
URL <https://www.doi.org/10.1103/PhysRevB.98.165134>

- [60] MARSILLAC, S., A. M. COMBOT-MARIE, J. C. BERNÈDE, and A. CONAN (1996) “Experimental evidence of the low-temperature formation of  $\gamma$ -In<sub>2</sub>Se<sub>3</sub> thin films obtained by a solid-state reaction,” *Thin Solid Films*, **288**(1), pp. 14–20, zSCC: NoCitationData[s0].  
URL [https://www.doi.org/10.1016/S0040-6090\(96\)08799-8](https://www.doi.org/10.1016/S0040-6090(96)08799-8)
- [61] LIKFORMAN, A., D. CARRÉ, and R. HILLEL (1978) “Structure cristalline du sélénium d’indium In<sub>2</sub>Se<sub>3</sub>,” *Acta Crystallographica Section B*, **34**(1), pp. 1–5, zSCC: 0000100 Publisher: International Union of Crystallography (IUCr).  
URL <https://www.doi.org/10.1107/S0567740878002174>
- [62] WEI, X., H. FENG, L. LI, J. GONG, K. JIANG, S. XUE, and P. K. CHU (2020) “Synthesis of tetragonal prismatic  $\gamma$ -In<sub>2</sub>Se<sub>3</sub> nanostructures with predominantly {110} facets and photocatalytic degradation of tetracycline,” *Applied Catalysis B: Environmental*, **260**, p. 118218, zSCC: 0000003.  
URL <https://www.doi.org/10.1016/j.apcatb.2019.118218>
- [63] VASSILEV, G. P., B. DAOUCHI, M.-C. RECORD, and J.-C. TEDENAC (1998) “Thermodynamic studies of the In–Se system,” *Journal of Alloys and Compounds*, **269**(1), pp. 107–115, zSCC: 0000023.  
URL [https://www.doi.org/10.1016/S0925-8388\(98\)00007-3](https://www.doi.org/10.1016/S0925-8388(98)00007-3)
- [64] PFITZNER, A. and H. D. LUTZ (1996) “Redetermination of the Crystal Structure of  $\gamma$ -In<sub>2</sub>Se<sub>3</sub> by Twin Crystal X-Ray Method,” *Journal of Solid State Chemistry*, **124**(2), pp. 305–308, zSCC: 0000063.  
URL <https://www.doi.org/10.1006/jssc.1996.0241>
- [65] JASINSKI, J., W. SWIDER, J. WASHBURN, Z. LILIENTAL-WEBER, A. CHAIKEN, K. NAUKA, G. A. GIBSON, and C. C. YANG (2002) “Crystal structure of  $\kappa$ -In<sub>2</sub>Se<sub>3</sub>,” *Applied Physics Letters*, **81**(23), pp. 4356–4358, zSCC: NoCitationData[s0] Publisher: American Institute of Physics.  
URL <https://www.doi.org/10.1063/1.1526925>
- [66] YU, X., T. HOU, X. SUN, and Y. LI (2013) “Atomistic structures and phase transition of In<sub>2</sub>Se<sub>3</sub> nanowires studied by DFT calculations and synchrotron radiation X-ray diffraction,” *Solid State Communications*, **162**, pp. 28–33, zSCC: 0000008.  
URL <https://www.doi.org/10.1016/j.ssc.2013.03.012>
- [67] ZHANG, F., Z. WANG, J. DONG, A. NIE, J. XIANG, W. ZHU, Z. LIU, and C. TAO (2019) “Atomic-Scale Observation of Reversible Thermally Driven Phase Transformation in 2D In<sub>2</sub>Se<sub>3</sub>,” *ACS Nano*, **13**(7), pp. 8004–8011, zSCC: 0000006 Publisher: American Chemical Society.  
URL <https://www.doi.org/10.1021/acsnano.9b02764>

- [68] COLLINS, J. L., C. WANG, A. TADICH, Y. YIN, C. ZHENG, J. HELLERSTEDT, A. GRUBIŠIĆ-ČABO, S. TANG, S.-K. MO, J. RILEY, E. HUWALD, N. V. MEDHEKAR, M. S. FUHRER, and M. T. EDMONDS (2020) “Electronic Band Structure of In-Plane Ferroelectric van der Waals  $\beta'$ -In<sub>2</sub>Se<sub>3</sub>,” *ACS Applied Electronic Materials*, **2**(1), pp. 213–219, zSCC: 0000000 Publisher: American Chemical Society. URL <https://www.doi.org/10.1021/acsaelm.9b00699>
- [69] SROUR, J., M. BADAWI, F. EL HAJ HASSAN, and A. POSTNIKOV (2018) “Comparative study of structural and electronic properties of GaSe and InSe polytypes,” *The Journal of Chemical Physics*, **149**(5), p. 054106, zSCC: 0000013 Publisher: American Institute of Physics. URL <https://www.doi.org/10.gd2q5m>
- [70] JESSEN, B. S., P. R. WHELAN, D. M. A. MACKENZIE, B. LUO, J. D. THOMSEN, L. GAMMELGAARD, T. J. BOOTH, and P. BØGGILD (2018) “Quantitative optical mapping of two-dimensional materials,” *Scientific Reports*, **8**(1), pp. 1–8, 00008. URL <https://www.doi.org/10.gdg5dr>
- [71] HUANG, Y., E. SUTTER, N. N. SHI, J. ZHENG, T. YANG, D. ENGLUND, H.-J. GAO, and P. SUTTER (2015) “Reliable Exfoliation of Large-Area High-Quality Flakes of Graphene and Other Two-Dimensional Materials,” *ACS Nano*, **9**(11), pp. 10612–10620, 00179. URL <https://www.doi.org/10.f72s64>
- [72] CELANO, U. (2019) “The Atomic Force Microscopy for Nanoelectronics,” *Electrical Atomic Force Microscopy for Nanoelectronics*, pp. 1–28, publisher: Springer, Cham. URL [https://www.doi.org/10.1007/978-3-030-15612-1\\_1](https://www.doi.org/10.1007/978-3-030-15612-1_1)
- [73] XU, K., W. SUN, Y. SHAO, F. WEI, X. ZHANG, W. WANG, and P. LI (2018) “Recent development of PeakForce Tapping mode atomic force microscopy and its applications on nanoscience,” *Nanotechnology Reviews*, **7**(6), pp. 605–621, publisher: De Gruyter Section: Nanotechnology Reviews. URL <https://www.doi.org/10.1515/ntrev-2018-0086>
- [74] MARTIN, S., B. GAUTIER, N. BABOUX, A. GRUVERMAN, A. CARRETERO-GENEVRIER, M. GICH, and A. GOMEZ (2019) “Characterizing Ferroelectricity with an Atomic Force Microscopy: An All-Around Technique,” *Electrical Atomic Force Microscopy for Nanoelectronics*, pp. 173–203, publisher: Springer, Cham. URL [https://www.doi.org/10.1007/978-3-030-15612-1\\_6](https://www.doi.org/10.1007/978-3-030-15612-1_6)
- [75] VASUDEVAN, R. K., N. BALKE, P. MAKSYMOVYCH, S. JESSE, and S. V. KALININ (2017) “Ferroelectric or non-ferroelectric: Why so many materials exhibit “ferroelectricity” on the nanoscale,” *Applied Physics Reviews*, **4**(2), p. 021302, zSCC: 0000109 Publisher: American Institute of Physics. URL <https://www.doi.org/10.1063/1.4979015>

- [76] NEUMAYER, S. M., S. SAREMI, L. W. MARTIN, L. COLLINS, A. TSELEV, S. JESSE, S. V. KALININ, and N. BALKE (2020) “Piezoresponse amplitude and phase quantified for electromechanical characterization,” *Journal of Applied Physics*, **128**(17), p. 171105, publisher: AIP Publishing LLCAIP Publishing.  
URL <https://www.doi.org/10.1063/5.0011631>
- [77] BALKE, N., P. MAKSYMOVYCH, S. JESSE, A. HERKLOTZ, A. TSELEV, C.-B. EOM, I. I. KRAVCHENKO, P. YU, and S. V. KALININ (2015) “Differentiating Ferroelectric and Nonferroelectric Electromechanical Effects with Scanning Probe Microscopy,” *ACS Nano*, **9**(6), pp. 6484–6492, publisher: American Chemical Society.  
URL <https://www.doi.org/10.1021/acsnano.5b02227>
- [78] CUI, C., W.-J. HU, X. YAN, C. ADDIEGO, W. GAO, Y. WANG, Z. WANG, L. LI, Y. CHENG, P. LI, X. ZHANG, H. N. ALSHAREEF, T. WU, W. ZHU, X. PAN, and L.-J. LI (2018) “Intercorrelated In-Plane and Out-of-Plane Ferroelectricity in Ultrathin Two-Dimensional Layered Semiconductor  $\text{In}_2\text{Se}_3$ ,” *Nano Letters*, **18**(2), pp. 1253–1258, 00000.  
URL <https://www.doi.org/10.1021/acs.nanolett.7b04852>
- [79] BALKE, N., P. MAKSYMOVYCH, S. JESSE, A. HERKLOTZ, A. TSELEV, C.-B. EOM, I. I. KRAVCHENKO, P. YU, and S. V. KALININ (2015) “Differentiating Ferroelectric and Nonferroelectric Electromechanical Effects with Scanning Probe Microscopy,” *ACS Nano*, **9**(6), pp. 6484–6492, publisher: American Chemical Society.  
URL <https://www.doi.org/10.1021/acsnano.5b02227>
- [80] MA, H., J. LIANG, H. HONG, K. LIU, D. ZOU, M. WU, and K. LIU (2020) “Rich information on 2D materials revealed by optical second harmonic generation,” *Nanoscale*, **12**(45), pp. 22891–22903, publisher: The Royal Society of Chemistry.  
URL <https://www.doi.org/10.1039/DONR06051H>
- [81] DENEV, S. A., T. T. A. LUMMEN, E. BARNES, A. KUMAR, and V. GOPALAN (2011) “Probing Ferroelectrics Using Optical Second Harmonic Generation,” *Journal of the American Ceramic Society*, **94**(9), pp. 2699–2727, publisher: John Wiley & Sons, Ltd.  
URL <https://www.doi.org/10.1111/j.1551-2916.2011.04740.x>
- [82] LEISGANG, N., J. G. ROCH, G. FROEHLICHER, M. HAMER, D. TERRY, R. GORBACHEV, and R. J. WARBURTON (2018) “Optical second harmonic generation in encapsulated single-layer InSe,” *AIP Advances*, **8**(10), p. 105120, publisher: American Institute of Physics.  
URL <https://www.doi.org/10.1063/1.5052417>
- [83] MURRAY, W., M. LUCKING, E. KAHN, T. ZHANG, K. FUJISAWA, N. PEREALOPEZ, A. L. ELIAS, H. TERRONES, M. TERRONES, and Z. LIU (2020) “Second

- harmonic generation in two-dimensional transition metal dichalcogenides with growth and post-synthesis defects,” *2D Materials*, **7**(4), p. 045020, publisher: IOP Publishing.  
URL <https://www.doi.org/10.1088/2053-1583/aba564>
- [84] GUAN, Z., H. HU, X. SHEN, P. XIANG, N. ZHONG, J. CHU, and C. DUAN (2020) “Recent Progress in Two-Dimensional Ferroelectric Materials,” *Advanced Electronic Materials*, **6**(1), p. 1900818, publisher: John Wiley & Sons, Ltd.  
URL <https://www.doi.org/10.1002aelm.201900818>
- [85] MENNEL, L., M. M. FURCHI, S. WACHTER, M. PAUR, D. K. POLYUSHKIN, and T. MUELLER (2018) “Optical imaging of strain in two-dimensional crystals,” *Nature Communications*, **9**(1), p. 516, number: 1 Publisher: Nature Publishing Group.  
URL <https://www.doi.org/10.1038/s41467-018-02830-y>
- [86] LI, Y., Y. RAO, K. F. MAK, Y. YOU, S. WANG, C. R. DEAN, and T. F. HEINZ (2013) “Probing Symmetry Properties of Few-Layer MoS<sub>2</sub> and h-BN by Optical Second-Harmonic Generation,” *Nano Letters*, **13**(7), pp. 3329–3333, publisher: American Chemical Society.  
URL <https://www.doi.org/10.1021/nl401561r>
- [87] MURRAY, W. (2020) “Nonlinear Optical Characterization with Instrumentation Development,” .
- [88] ZHANG, X., X.-F. QIAO, W. SHI, J.-B. WU, D.-S. JIANG, and P.-H. TAN (2015) “Phonon and Raman scattering of two-dimensional transition metal dichalcogenides from monolayer, multilayer to bulk material,” *Chemical Society Reviews*, **44**(9), pp. 2757–2785, publisher: The Royal Society of Chemistry.  
URL <https://www.doi.org/10.1039/C4CS00282B>
- [89] LIANG, F., H. XU, X. WU, C. WANG, C. LUO, and J. ZHANG (2018) “Raman spectroscopy characterization of two-dimensional materials,” *Chinese Physics B*, **27**(3), p. 037802, publisher: IOP Publishing.  
URL <https://www.doi.org/10.1088/1674-1056/27/3/037802>
- [90] WU, J. and L. XIE (2019) “Structural Quantification for Graphene and Related Two-Dimensional Materials by Raman Spectroscopy,” *Analytical Chemistry*, **91**(1), pp. 468–481, publisher: American Chemical Society.  
URL <https://www.doi.org/10.1021/acs.analchem.8b04991>
- [91] MCCREARY, K. M., A. T. HANBICKI, G. G. JERNIGAN, J. C. CULBERTSON, and B. T. JONKER (2016) “Synthesis of Large-Area WS<sub>2</sub> monolayers with Exceptional Photoluminescence,” *Scientific Reports*, **6**(1), p. 19159, number: 1 Publisher: Nature Publishing Group.  
URL <https://www.doi.org/10.1038/srep19159>

- [92] NGUYEN, T. A., J.-U. LEE, D. YOON, and H. CHEONG (2014) “Excitation Energy Dependent Raman Signatures of ABA- and ABC-stacked Few-layer Graphene,” *Scientific Reports*, **4**(1), p. 4630, number: 1 Publisher: Nature Publishing Group. URL <https://www.doi.org/10.1038/srep04630>
- [93] KIM, Y. A., K. FUJISAWA, H. MURAMATSU, T. HAYASHI, M. ENDO, T. FUJIMORI, K. KANEKO, M. TERRONES, J. BEHRENDTS, A. ECKMANN, C. CASIRAGHI, K. S. NOVOSELOV, R. SAITO, and M. S. DRESSELHAUS (2012) “Raman Spectroscopy of Boron-Doped Single-Layer Graphene,” *ACS Nano*, **6**(7), pp. 6293–6300, publisher: American Chemical Society. URL <https://www.doi.org/10.1021/nn301728j>
- [94] FUJISAWA, K., T. HAYASHI, M. ENDO, M. TERRONES, J. HEE KIM, and Y. AHM KIM (2018) “Effect of boron doping on the electrical conductivity of metallicity-separated single walled carbon nanotubes,” *Nanoscale*, **10**(26), pp. 12723–12733, publisher: Royal Society of Chemistry. URL <https://www.doi.org/10.1039/C8NR02323A>
- [95] TSUKADA, S. (2018) “Raman scattering study of the ferroelectric phase transition in BaTi<sub>2</sub>O<sub>5</sub>,” *Physical Review B*, **97**(2). URL <https://www.doi.org/10.1103/PhysRevB.97.024116>
- [96] SWAIN, D., V. S. BHADRAM, G. K. PRADHAN, and C. NARAYANA (2020) “Understanding the Mechanism of Ferroelectric Phase Transition in RbHSO<sub>4</sub>: A High-Pressure Raman Investigation,” *Inorganic Chemistry*, **59**(12), pp. 7960–7965, publisher: American Chemical Society. URL <https://www.doi.org/10.1021/acs.inorgchem.9b03340>
- [97] KIM, J., J.-U. LEE, and H. CHEONG (2020) “Polarized Raman spectroscopy for studying two-dimensional materials,” *Journal of Physics: Condensed Matter*, **32**(34), p. 343001, publisher: IOP Publishing. URL <https://www.doi.org/10.1088/1361-648X/ab8848>
- [98] GABEL, M. and Y. GU (2021) “Understanding Microscopic Operating Mechanisms of a van der Waals Planar Ferroelectric Memristor,” *Advanced Functional Materials*, **31**(9), p. 2009999, publisher: John Wiley & Sons, Ltd. URL <https://www.doi.org/10.1002/adfm.202009999>
- [99] TSUKADA, S. and Y. FUJII (2020) “Multivariate curve resolution for angle-resolved polarized Raman spectroscopy of ferroelectric crystals,” *Japanese Journal of Applied Physics*, **59**(SK), p. SKKA03, publisher: IOP Publishing. URL <https://www.doi.org/10.35848/1347-4065/ab78e8>
- [100] TSUKADA, S., Y. FUJII, Y. YONEDA, H. MORIWAKE, A. KONISHI, and Y. AKISHIGE (2018) “Raman scattering study of the ferroelectric phase transition in BaTi<sub>2</sub>O<sub>5</sub>,” *Physical Review B*, **97**(2), p. 024116, publisher: American Physical

Society.

URL <https://www.doi.org/10.1103/PhysRevB.97.024116>

- [101] DE, B. K., V. DWIJ, R. MISAWA, T. KIMURA, and V. G. SATHE (2021) “Femtometer atomic displacement, the root cause for multiferroic behavior of CuO unearthed through polarized Raman spectroscopy,” *Journal of Physics: Condensed Matter*, **33**(12), p. 12LT01, publisher: IOP Publishing.  
URL <https://www.doi.org/10.1088/1361-648X/abd738>
- [102] “LOR and PMGI Resists Data Sheet,” 00000.
- [103] “Megaposit SPR3000 Series Photoresist,” 00000.
- [104] CHOI, D.-Y., S. MADEN, A. RODE, R. WANG, and B. LUTHER-DAVIES (2008) “Plasma etching of As<sub>2</sub>S<sub>3</sub> films for optical waveguides,” *Journal of Non-Crystalline Solids*, **354**(27), pp. 3179–3183, 00036.  
URL <https://www.doi.org/10.frgxxg>
- [105] “PMMA Resist Datasheet,” 00000.
- [106] “Nano PMGI Resists Datasheet,” 00000.
- [107] FRISENDA, R., E. NAVARRO-MORATALLA, P. GANT, D. P. D. LARA, P. JARILLO-HERRERO, R. V. GORBACHEV, and A. CASTELLANOS-GOMEZ (2018) “Recent progress in the assembly of nanodevices and van der Waals heterostructures by deterministic placement of 2D materials,” *Chemical Society Reviews*, **47**(1), pp. 53–68, publisher: The Royal Society of Chemistry.  
URL <https://www.doi.org/10.1039/C7CS00556C>
- [108] (2007), “Physical Property Measurement System Hardware Manual,” .
- [109] DÜNKEL, S., M. TRENTZSCH, R. RICHTER, P. MOLL, C. FUCHS, O. GEHRING, M. MAJER, S. WITTEK, B. MÜLLER, T. MELDE, H. MULAOSMANOVIC, S. SLE-SAZECK, S. MÜLLER, J. OCKER, M. NOACK, D.-A. LÖHR, P. POLAKOWSKI, J. MÜLLER, T. MIKOLAJICK, J. HÖNTSCHEL, B. RICE, J. PELLERIN, and S. BEYER (2017) “A FeFET based super-low-power ultra-fast embedded NVM technology for 22nm FDSOI and beyond,” in *2017 IEEE International Electron Devices Meeting (IEDM)*, pp. 19.7.1–19.7.4, 00051 ISSN: 2156-017X.  
URL <https://www.doi.org/10.1109/iedm.2017.8268425>
- [110] SI, M., P.-Y. LIAO, G. QIU, Y. DUAN, and P. D. YE (2018) “Ferroelectric Field-Effect Transistors Based on MoS<sub>2</sub> and CuInP<sub>2</sub>S<sub>6</sub> Two-Dimensional van der Waals Heterostructure,” *ACS Nano*, **12**(7), pp. 6700–6705, 00000.  
URL <https://www.doi.org/10.1021/acsnano.8b01810>
- [111] KHAN, A. I., A. KESHAVARZI, and S. DATTA (2020) “The future of ferroelectric field-effect transistor technology,” *Nature Electronics*, **3**(10), pp. 588–597, zSCC:

0000002 Number: 10 Publisher: Nature Publishing Group.  
URL <https://www.doi.org/10.1038/s41928-020-00492-7>

- [112] MA, T. and J.-P. HAN (2002) “Why is nonvolatile ferroelectric memory field-effect transistor still elusive?” *IEEE Electron Device Letters*, **23**(7), pp. 386–388, 00000 ZSCC: 0000335 Conference Name: IEEE Electron Device Letters.  
URL <https://www.doi.org/10.djzs4x>
- [113] SI, M., A. K. SAHA, S. GAO, G. QIU, J. QIN, Y. DUAN, J. JIAN, C. NIU, H. WANG, W. WU, S. K. GUPTA, and P. D. YE (2019) “A ferroelectric semiconductor field-effect transistor,” *Nature Electronics*, pp. 1–7, zSCC: 0000002.  
URL <https://www.doi.org/10.1038/s41928-019-0338-7>
- [114] DING, W., J. ZHU, Z. WANG, Y. GAO, D. XIAO, Y. GU, Z. ZHANG, and W. ZHU (2017) “Prediction of intrinsic two-dimensional ferroelectrics in In<sub>2</sub>Se<sub>3</sub> and other III<sub>2</sub>-VI<sub>3</sub> van der Waals materials,” *Nature Communications*, **8**(1), pp. 1–8, 00000.  
URL <https://www.doi.org/10.1038/ncomms14956>
- [115] DAI, M., K. LI, F. WANG, Y. HU, J. ZHANG, T. ZHAI, B. YANG, Y. FU, W. CAO, D. JIA, Y. ZHOU, and P. Hu (2020) “Intrinsic Dipole Coupling in 2D van der Waals Ferroelectrics for Gate-Controlled Switchable Rectifier,” *Advanced Electronic Materials*, **6**(2), p. 1900975, 00000 Publisher: John Wiley & Sons, Ltd.  
URL <https://www.doi.org/10.1002aelm.201900975>
- [116] XIAO, J., H. ZHU, Y. WANG, W. FENG, Y. HU, A. DASGUPTA, Y. HAN, Y. WANG, D. A. MULLER, L. W. MARTIN, P. HU, and X. ZHANG (2018) “Intrinsic Two-Dimensional Ferroelectricity with Dipole Locking,” *Physical Review Letters*, **120**(22), p. 227601, 00046.  
URL <https://www.doi.org/10.1103/physrevlett.120.227601>
- [117] ZHOU, Y., D. WU, Y. ZHU, Y. CHO, Q. HE, X. YANG, K. HERRERA, Z. CHU, Y. HAN, M. C. DOWNER, H. PENG, and K. LAI (2017) “Out-of-Plane Piezoelectricity and Ferroelectricity in Layered α-In<sub>2</sub>Se<sub>3</sub> Nanoflakes,” *Nano Letters*, **17**(9), pp. 5508–5513, 00000.  
URL <https://www.doi.org/10.1021/acs.nanolett.7b02198>
- [118] WAN, S., Y. LI, W. LI, X. MAO, W. ZHU, and H. ZENG (2018) “Room-temperature ferroelectricity and a switchable diode effect in two-dimensional α-In<sub>2</sub>Se<sub>3</sub> thin layers,” *Nanoscale*, **10**(31), pp. 14885–14892, 00000.  
URL <https://www.doi.org/10.1039/C8NR04422H>
- [119] HOU, P., Y. LV, X. ZHONG, and J. WANG (2019) “α-In<sub>2</sub>Se<sub>3</sub> Nanoflakes Modulated by Ferroelectric Polarization and Pt Nanodots for Photodetection,” *ACS Applied Nano Materials*, **2**(7), pp. 4443–4450, 00002 Publisher: American Chemical Society.  
URL <https://www.doi.org/10.ggppwb>

- [120] HOU, P., S. XING, X. LIU, C. CHEN, X. ZHONG, J. WANG, and X. OUYANG (2019) “Resistive switching behavior in  $\alpha$ -In<sub>2</sub>Se<sub>3</sub> nanoflakes modulated by ferroelectric polarization and interface defects,” *RSC Advances*, **9**(52), pp. 30565–30569, 00000 ZSCC: 0000000 Publisher: Royal Society of Chemistry.  
URL <https://www.doi.org/10.1039/c9ra06566k>
- [121] WAN, S., Y. LI, W. LI, X. MAO, C. WANG, C. CHEN, J. DONG, A. NIE, J. XIANG, Z. LIU, W. ZHU, and H. ZENG (2019) “Nonvolatile Ferroelectric Memory Effect in Ultrathin  $\alpha$ -In<sub>2</sub>Se<sub>3</sub>,” *Advanced Functional Materials*, **29**(20), p. 1808606, 00010.  
URL <https://www.doi.org/10.1002/adfm.201808606>
- [122] YANG, H., M. XIAO, Y. CUI, L. PAN, K. ZHAO, and Z. WEI (2019) “Nonvolatile memristor based on heterostructure of 2D room-temperature ferroelectric  $\alpha$ -In<sub>2</sub>Se<sub>3</sub> and WSe<sub>2</sub>,” *Science China Information Sciences*, **62**(12), pp. 1–8, 00000 ZSCC: 0000000 Company: Springer Distributor: Springer Institution: Springer Label: Springer Number: 12 Publisher: Science China Press.  
URL <https://www.doi.org/10.1007/s11432-019-1474-3>
- [123] CHOI, D.-Y., S. MADDEN, D. BULLA, A. RODE, R. WANG, and B. LUTHER-DAVIES (2011) “SU-8 protective layer in photo-resist patterning on As<sub>2</sub>S<sub>3</sub> film,” *physica status solidi c*, **8**(11-12), pp. 3183–3186, zSCC: 0000011.  
URL <https://www.doi.org/10.1002/pssc.201000741>
- [124] CHOI, D.-Y., S. MADDEN, A. RODE, R. WANG, D. BULLA, and B. LUTHER-DAVIES (2008) “A protective layer on As<sub>2</sub>S<sub>3</sub> film for photo-resist patterning,” *Journal of Non-Crystalline Solids*, **354**(47-51), pp. 5253–5254, zSCC: 0000015.  
URL <https://www.doi.org/10.1016/j.jnoncrysol.2008.05.067>
- [125] BALAKRISHNAN, N., E. D. STEER, E. F. SMITH, Z. R. KUDRYNSKYI, Z. D. KOVALYUK, L. EAVES, A. PATANÈ, and P. H. BETON (2018) “Epitaxial growth of  $\gamma$ -InSe and  $\alpha$ ,  $\beta$ , and  $\gamma$ -In<sub>2</sub>Se<sub>3</sub> on  $\varepsilon$ -GaSe,” *2D Materials*, **5**(3), p. 035026, zSCC: 0000016.  
URL <https://www.doi.org/10.1088/2053-1583/aac479>
- [126] ISLAND, J. O., S. I. BLANTER, M. BUSCEMA, H. S. J. VAN DER ZANT, and A. CASTELLANOS-GOMEZ (2015) “Gate Controlled Photocurrent Generation Mechanisms in High-Gain In<sub>2</sub>Se<sub>3</sub> Phototransistors,” *Nano Letters*, **15**(12), pp. 7853–7858, zSCC: 0000151 Publisher: American Chemical Society.  
URL <https://www.doi.org/10.1021/acs.nanolett.5b02523>
- [127] (1986) “Electrical and optical properties of In<sub>2</sub>Se<sub>3</sub> thin films,” *Thin Solid Films*, **137**(1), pp. 27–37, publisher: Elsevier.  
URL [https://www.doi.org/10.1016/0040-6090\(86\)90191-4](https://www.doi.org/10.1016/0040-6090(86)90191-4)
- [128] HIKAMI, S., A. I. LARKIN, and Y. NAGAOKA (1980) “Spin-Orbit Interaction and Magnetoresistance in the Two Dimensional Random System,” *Progress of*

*Theoretical Physics*, **63**(2), pp. 707–710, zSCC: 0002742.  
URL <https://www.doi.org/10/csg659>

- [129] LEE, P. A. (1985) “Disordered electronic systems,” *Reviews of Modern Physics*, **57**(2), pp. 287–337, zSCC: 0006454.  
URL <https://www.doi.org/10/cqht5z>

**Vita**  
**Your Name**

The details of my childhood are inconsequential.